A Radar Signal Processing Study

on PMCW and FMCW radar systems

Adham Sakhnini

Abstract

Automotive radar systems have undergone a long and extensive evolution since the first prototypes appeared in automotive industry labs in the 1970s. Since then, practically all major manufacturers have started to offer radar systems in some car models, promising increased safety and comfort. The current use include tasks such as adaptive cruise control, collision avoidance and parking assistance, with the trend appearing to become an industry standard. Very recently, phase modulated systems have started to emerge, challenging the current fast chirping state-of-the-art in terms of cost, resolution and cooperability while simultaneously enabling efficient communication capabilities. This thesis is an attempt at making a comparison between these kind of systems from an idealistic signal processing perspective. Specifically, three contributions are attempted.

First, some of the current established literature is gathered and summarized, focusing on development and mutual interference aspects of phase modulated systems. Second, a system analysis is performed, presenting some automotive system requirements and finishing with a case study. It is shown that phase modulated systems provide better performance in terms resolution and contrasting capabilities, but suffers from dynamic range degradations in scenarios of uncompensated Doppler. The systems are further investigated in terms of multi-transmit multi-receive capabilities, where it is argued that phase modulated systems are advantageous in terms of up-scaling.

In the third contribution, computational approaches are investigated in an attempt at resolving some of the resolution and Doppler-degrading shortcomings. It is first confirmed that data adaptive algorithms may provide significant performance gains in some automotive scenarios where angular resolution is bottlenecking. Then, a mismatched filtering approach is taken to deal with Doppler degradations at pulse compression. It is shown that for some common binary sequences, the Doppler-degradation can be heavily attenuated by mismatching at receive with only small losses in processing gain. However, a major drawback is the large number of bits (16 to 24) needed in the filter representation.

Acknowledgements

Writing this thesis during the Spring of 2020 has been exciting and fulfilling in many ways and aspects. The topic has been on phase and frequency modulated radar systems, where the objective has been to investigate each kind of system. With this, I have been given the opportunity to explore fields which I have been fond of ever since introduced to, namely signal processing and radar systems. Even though the process has been a roller-coaster (as a thesis should be), I am happy with the outcome. To this end, I am grateful for the people who have supported me during the course of this work.

Specifically, I wish to thank my mentor and advisor Prof. Andreas Jakobsson for taking care of me during my MSc studies and for teaching me some real black belt signal processing. I have yet met anyone so dedicated and supportive towards his students.

Furthermore, a big thank you to Cacke and Sebastian for supervising me during this time, and for all the patience, friendship and warmth given. In hindsight, I am convinced that I could not have been given any better support.

Also, I wish to express my big thanks to N13, Pi14, Corridor Vanner, iGEM Lund 2017/2018, PCNI, CTR, Johan and Hanna for all the companionship and happiness shared during my years of study at LTH.

And finally, a big thank you to my family and most specifically to my Mum for all the unconditional love, support and kindness.

Lund in June 2020

Adham Sakhnini

Contents

List of Abbreviations

ACDC	All-cell-Doppler correction
ACMC	All-cell migration compensation
ADAS	Advanced driver-assistance system
ADC	Analog to digital converter
CMOS	Complementary metal oxide semiconductor
CPI	Coherent processing interval
FMCW	Frequency modulated continuous wave
FPGA	Field-programmable gate array
IF	Intermediate frequency
INR	Interference to noise ratio
LIDAR	Laser detection and ranging
LO	Local oscillator
LPF	Low pass filter
MIMO	Multiple input multiple output
MTI	Moving target indication
PMCW	Phase modulated continuous wave
PRF	Pulse repetition frequency
PRI	Pulse repetition interval

Radar	Radio detection and ranging
RF	Radio frequency
Rx	Receiver
SCR	Signal to clutter ratio
SIR	Signal to interference ratio
SNR	Signal to noise ratio
Tx	Transmitter

Chapter 1

Introduction

Radar, short for radio detection and ranging, is a type of apparatus used for detection, localization, tracking and characterization of objects in a confined region in space. The working principle is based on time of flight and energy measurements of transmitted sets of pulses scattered off from targets in a field of view. If a received echo has enough power to be significantly different from noise, clutter or interference, a target is deemed to be present. By measuring the time from transmission to reception, the distance to the target can be estimated. By measuring the change in distance from pulse to pulse, the radial velocity of the target can be estimated. By employing a scanning type of system, or multiple transmitters or receivers, the horizontal and vertical angles to the target can be estimated. If the system has enough resolution, target signatures (such as micro-motions) can be used to characterize (classify) the target. If the system has few ambiguities in the measurements, multiple targets can be detected, localized and characterized simultaneously. By employing multiple target tracking algorithms, each target can be monitored over a sequence of frames.

Thus, radar systems are very capable, providing all necessary information for obtaining comprehensive situational awareness of monitored environments. Compared to optical, infrared, laser and ultrasound systems, radar systems have long range capabilities and the ability to function even under harsh weather conditions and external interference due to the inherent environmental robustness and by the combination of smart system and signal processing design. This has made them extensively popular in military systems (from which they originate from), with the main application being air defence (from ground, sea or air) since the invention in the 1930s to defend against bomber aircrafts. Other applications include early warning systems, missile guidance, non-cooperative target recognition and confined area surveillance, among many others. To this end, the useage has largely been a success

story, and have played critical roles during wartimes [1–6].

Over the past decades, radar systems have emerged in numerous civilian applications, such as airport traffic control, marine navigation, speed cameras for law enforcement, remote sensing of the environment and much more [3, 4, 7]. An emerging application field is within healthcare, where applications such as contact-less vital sign monitoring [8–10], and human monitoring [11, 12] are being developed. For instance, in [10], a radar system was shown to be capable of tracking multiple persons while simultaneously monitoring each individuals vital signs, including breathing and heartbeat rates. Even more recently, radar systems has started entering consumer applications, ranging from advanced driver-assistance systems to wearables and other applications [13–17]. In [15], a pulsed coherent radar was used for gesture control of headphones, and in [14], the same radar was used for the gesture control of speakers, among other use cases. Perhaps more indicative, the new pixel 4 from Google was recently released, being the first known commercial cellphone to employ a small radar sensor for presence detection and gesture recognition [16–19].

There are many books and papers on radar systems and applications. For a further overview, see for instance the recent magazines [20, 21], as well as [4, 22, 23]. The topic of this thesis will be on phase and linear frequency modulated automotive radar systems as applied for advanced driver assistance.

1.1 Motivation

In 2016, approximately 1.35 million people died as a direct consequence of road traffic injuries, corresponding to one fatality every 25 seconds [24]. As a consequence of the high rates of traffic accidents, the automotive industry has for several decades invested a lot of resources on developing driver safety functions. These efforts have mainly consisted of passive systems which work by alleviating the accident once it has happened, with examples including air-bags, seat belts and crumple zones. However, as pointed out in [25], the passive systems have been "virtually exhausted" and what remains is exploring active safety systems, where the accident is mitigated before taking place. In order to accomplish this, a set of sensors providing enough information about the environment for the task at hand is required in order to either alarm the driver to take action or autonomously avoid or mitigate the hazard. Perhaps anticipated, it has been shown that after the seat belt, the most efficient safety system for the passengers is dynamic driving controls (see the references in [26]).

One active area of research and development is within advanced driver-assistance systems (ADAS), which are electronic systems aimed at assisting the driver to operate the vehicle (see [26, 27] and the introduction of [28]). These systems are deemed important since most accidents are due to human errors caused by loss of alertness, inattention, fatigue and alcohol [29]. Possible scenarios include direct measures such as collision avoidance and traffic alert, but also reducing the risk of accident by a driver's slip by increasing the drivers comfort through functionalities such as, for instance, adaptive cruise control, parking assistance and ultimately automated driving. In the light of these aspirations, radar systems have emerged as promising candidates due to the robust operational capabilities even under non-ideal environmental conditions, while simultaneously providing accurate localization performance of widely separated targets in the field of view. As an example, Figure 1.1 illustrates an adaptive cruise control scenario using a forward looking radar.

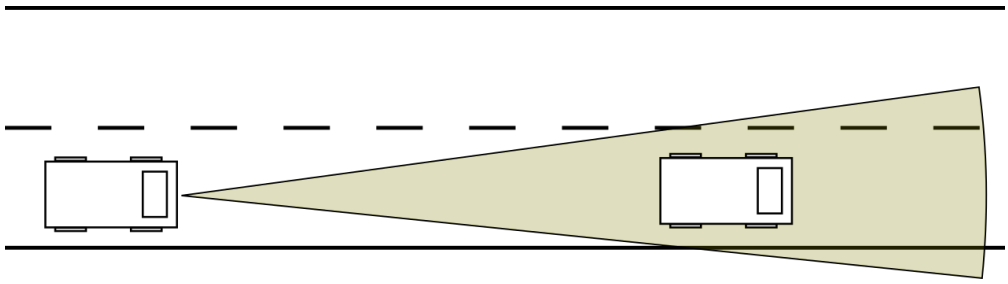

Figure 1.1: Illustration of an adaptive cruise control scenario.

To this end, automotive radar systems has undergone an extensive evolution since the first prototypes in the 1970s, with the first commercial systems appearing in Japanese cars during the 1980s developed by Toyota, Nissan and Honda [30] and in US and Europe during the late 1990s with the Daimler S-class systems, followed by Jaguar, Nissan and BMW [13, 25, 31]. Since then, practically all major automotive manufacturers have started to offer radar systems in some car models, being used in applications such as adaptive cruise control and brake assistance, with the trend appearing to become an industry standard [25, 31].

In the current state, the majority of the systems seem to employ some form of frequency modulation for range estimation, with linear sweeps appearing to become the most commonly used waveform as indicated in the literature (see, for instance [25, 30, 32, 33]) and by some of the current manufacturers [34–37]. While the frequency modulation can be realized in many different ways, each with its own set of advantages and disadvantage (see [32] for the automotive case), the main benefit is the ease of implementation and low cost, realized by the recent advances in hardware manufacturing [13] and the employement of the stretch processor which allows for the simultaneous use of high bandwidth waveforms and low analog receive

bandwidths, which significantly reduces the noise power and the required sampling rates to recover the signal [38–40]. In the case of linear frequency modulation, the stretch processing essentially de-ramps the chirp at receive which allows for a highly efficient implementation of the pulse compressor by a set of fast Fourier transforms.

Moving into the future, it has been concluded that the systems must be able to sustain high levels of interference caused by inter-operating sensors, as well as attaining even higher resolution in all dimensions (ideally approaching that of LIDAR) for accurate localization and mitigating the risk of corner case failures. One of the reasons for these requirements, as noted in [41], is that automotive radar systems are *clutter limited* as opposed of being noise limited like many conventional radar systems, and will therefore require high resolutions in order to resolve targets. For instance, resolving a car from a tunnel opening at decent distances requires high resolution in elevation, while separating a child walking close next to a car requires a high horizontal resolution, as well as high contrasting capablities. For an an overview on the topic of future system requirements, see [42] (and the reference therein), where the current state of the art technology is also discussed, covering aspects such as target tracking, clustering, waveform optimization and cognition. See also [43, 44], which explores some approaches of super resolution estimation.

As a part of the increasing demands and due to the technological advances, the tradtionally employed 24 GHz systems are getting phased out for the high bandwidth 77 GHz systems due to the smaller associated form factors as well as increased resolution in practically all dimensions [13]. However, while the range and Doppler resolution can be increased by simply increasing the bandwidth, and dwell time and operating frequency, the angular resolution remains a limiting factor since it requires additional receive channels which is burdened by the additional scaling in hardware and data processing units, to name two issues. For instance, the early automotive radar systems had limited angular capabilities and relied mostly on narrow and scanning beams, or limited beamforming [13], while the more recent systems have adopted digital beamforming by employing multiple-input multiple-output (MIMO) configurations, which has the advantage of providing a large aperture at reduced hardware and improved form factor by exploiting the concepts of diversity and virtual arrays [39,45]. The benefit is improved angular resolution at a relatively low cost and it appears that most current systems use three transmitters and four receivers with combined azimuth and elevation capabilities. Three examples include the systems developed by Texas Instruments [46], NXP [47] and ST [48], each using three transmitters and four receivers. Following the trend, imaging systems employing extensively larger MIMO configurations are emerging, with four examples being the next generation Texas Instruments imaging

radar [49], as well as the systems developed by Vayyar [50], Uhnder [51] and Arbe [52], each capable of employing 192 or more virtual receivers.

One may thus consider MIMO to be enabling technology in process of achieving high resolution. However, the technology has been a topic of controversty outside the automotive community [53–55] and while it appears that the industry is catching the trend and heading towards increasingly bigger MIMO systems, the advantages are not without compromise. For instance, in [56], it was shown that the amount of clear area in the MIMO ambiguity function is reduced by a factor corresponding to the number of transmitters employed. Another issue is the degraded interference rejection capabilities in the spatial domain since the entire virtual array no longer can be used to place mitigating nulls (the transmit steering vector is no longer known, see e.g. [57]). Thus, while larger MIMO systems consisting of several transmitters and receivers provide improved spatial capabilities, it is at the cost of various other system parameters which may impose additional design constraint on top of already challenging requirements.

1.2 Background

As previously noted, the main objective of automotive radar is to reduce the number of road accidents by taking pro-active measures and increasing the drivers comfort. To this end, some of the current limitations (or weaknesses) of FMCW systems are the lack of resolution and robustness to interference. In an attempt to circumvent these issues, larger bandwidths have been allocated [13], increasingly bigger MIMO systems developed [49–52], and novel interference mitigation and co-existance schemes considered [58, 59].

In [60, 61], a 79 GHz fully integrated phase modulated continuous wave (PMCW) radar system with MIMO capabilities, targeting consumer products, was for the first time demonstrated, suggesting several possible improvements over the mainstream FMCW systems. Among them, the use of phase codes allows for the design of waveforms with certain desireable properties. For instance, the codes can be constructed to give flat, unambiguous and thumbtack-like range responses after pulse compression [38], and by embedding additional information, vehicle-to-vechile communication becomes possible [62]. The employed waveforms may furthermore be designed with respect to the entire MIMO system in mind, allowing for a simultaneous transmit from all channels by fast time code division multiplexing [63]. Similar to communication systems, the use of spread spectrum techniques also implies a certain degree of robustness against interference, noise and jamming.

Some of the development appear to have started in [64], where the first transmitter in 28 nm CMOS capable of PMCW sensing was demonstrated, satisfying spectral mask regulations and capable of operating at the entire 77-81 GHz range at a chip rate of 2 Gbps. The design also showed a transmit effiency of 10.4 % at 27°C at an output power of 11.5 dBm, with a degradation of 4.3 dBm at 125°C. However, a major drawback was the large instantaneous bandwidth required to recover the transmitted signal, which implied the need for fast and expensive analog to digital converters and high throughput data processors. In [65], it was shown that for short range applications, only 4 bits are required to achieve a dynamic range of more than 70 dB, as a direct consequence of thermal noise dithering and large processing gains. Even 3 bits were deemed sufficient if certain performance losses were to be tolerated. The results indicated the feasibility of efficient CMOS implementation [66], and in [67], a parallized correlator bank was demostrated in an FPGA for compressing and accumulating the received echos (at half the bandwidth), also demonstrating computatioanl feasibility. Shortly after, the first fully integrated MIMO systems where presented [60, 61], capable of both transmission, reception and compression, leaving the rest of the processing to be handled off-chip (Doppler and direction of arrival estimation, detection, tracking etc.). In the design, two transmitters and two receivers were used, with the capability of cascading two chips into a 4-by-4 MIMO system, yielding a 5 degree angular resolution in both azimuth and elevation when employing a line parametric estimator. In [63,68–70], several waveforms were investigated for automotive radar use, each with their set of advantages and disadvantages, showing the possibility of satisfying the large dynamic range requirements by employing binary phase codes with zero correlation zones. Finally, in [51], a 12 transmitter and 8 receiver PMCW MIMO system was presented, capable of processing 192 virtual receivers by time multiplexing the transmitters in azimuth and elevation, allowing for both vertical and horizontal localization with very high resolution. To this end, this appears to the most capable PMCW system published to date, remaining highly competetive in performance when compared with the current state-of-the-art among FMCW systems.

Regarding interference aspects, it has been claimed that PMCW systems offers a certain degree of improved rejection due to the spread spectrum approach and (almost) arbitrary waveform design capabilities. While a lot of work on the nature of FMCW interference has been accomplished (e.g. [57, 58, 71–78], to name a few), there is still at the time of writing little work done on PMCW systems. The following is an attempt at summarizing the current state.

The first study on PMCW interference appear to be [79], where the performance was evaluated experimentally under simulated environments and compared with that of an equivalent

FMCW system. In the analysis, it was concluded that both PMCW and FMCW systems show similar susceptibility to either kind of interference, as long as no synchronization between the victim and interferer occurs. While happening rarely, these kind of interferences have the effect being amplified by the signal processor and thus dramatically increasing the interference to noise ratio (INR). In order to avoid these catastrophic scenarios of synchronization and spread out the interference in the range-Doppler domain, it was suggested that co-operating systems should differ at least 5 % in bandwidth and 40 ppm in carrier frequency as well as using different waveform modulations, such as differnet chirp rates in the case of FMCW and phase codes in the case of PMCW. It was also noted that in order to obtain a good spread in Doppler, the greatest common divisor of the number of pulses during a coherent processing interval (CPI) should be as small as possible.

A similar interference study was carried out in [80] where it was shown that both FMCW and PMCW systems suffers from ridges in the range-Doppler map which are dependent on the relative waveforms and velocities motion of the radar systems, even after moderate asynchronization. In the case PMCW, the spread was mostly limited to a single Doppler bin whereas in FMCW the ridges spread throughout the range-Doppler map. It was concluded that randomization is necessary for obtaining a good range-Doppler spread.

A Monte-Carlo interference study was carried out in [81], which showed that no substantial differences could be found in the noise floor between FMCW and PMCW systems when randomizing the carrier frequencies, bandwidths, pulse durations and code sequences of the interfers. However, it was shown that ridges appear in the range-Doppler domain for FMCW systems, which in practices makes the noise floor significantly more heavy-tailed and consequently degrading target detectability (in case of CFAR, raising the detection threshold), whereas in PMCW systems the spread was observed to be flat. The study was further supported by analytical investigations and it was concluded that the interference suppression is equal given uncorrelated systems and equal time-bandwidth products (but *not* equally distributed in range-Doppler). For future work, it was noted that the probability of interference and probability of uncorrelated and correlated (synchronization) for either kind of system needs to be investigated.

In [59, 82], an analytical approach was used to show that as a direct consequence of the stretch processing used, the INR is generally higher in FMCW systems than in PMCW systems, as related linearly by an introduced interference susceptibility factor. For PMCW systems, the factor was argued to always be close to one, regardless if the interferer is of FMCW or PMCW type. In the case of FMCW systems, the same conclusion was made

when interfered by a PMCW system. However, when interfered by another FMCW system, the factor is *generally* higher than one and directly related to the relative chirp rates of the victim and interferer. For instance, for two crossing chirps with opposite signs on the chirp rates, the factor is one and equal to the PMCW case, whereas the more similar the slopes are, the higher the susceptiblity factor. As an example on the order of magnitude, an amplification of more than 10 dB was illustrated for two systems sweeping at 15.36 and 13.5 MHz/us respectively [59]. The conclusion of this work is that the FMCW systems are more susceptible to INR degradations than PMCW systems as a direct consequence of the stretch processing employed. However, it also concludes that the more randomized (asynchronized, or dithered) the waveforms are, the smaller are the differences in susceptibility.

In [83], the effects of phase noise was considered in order to also consider hardware non-idealities in the interference analysis. Assuming the same type of victim and interferer, it was shown analytically that phase noise causes additional spreading in range and Doppler by mismatching with the receive filter. Based on the simulations, it was concluded that PMCW systems are less affected by phase noise in the interferer, in terms of range-Doppler spread and target masking. Furthermore, it was also concluded that these kind of non-idealities significantly affects interference susceptibility.

In [84], the impact of FMCW interference on PMCW systems was investigated using simulated data and a time domain excision approach to mitigate the effect proposed. It was noted that in order to mitigate the FMCW interference, a time domain approach must be used since otherwise the correlation properties of the phase codes are compromised. As such, the chirps were detected in baseband by thresholding and blanked out, yielding significant improvements in SNR. However, due to the periodic transmission of the interferer, the blanking was observed to result in artifacts in the range-Doppler domain. For aspects and strategies on PMCW-PMCW mitigation, see [85] and the discussions in [59].

Thus, to conclude, PMCW systems are *in general* better than FMCW systems at rejecting interference, specifically when hardware imperfections (e.g. phase noise) and real world scenarios (e.g. synchronization) are taken into account. Furthermore, the noise floor does not appear to be as heavy tailed as in FMCW, indicating better detection statistics. However, this is not due to the occurence of "orthogonal waveforms" in PMCW systems (although it definitely alleviates), but rather due to the risk of having similar chirps entering the passband in the stretch processor. Nevertheless, the advantages do not appear to be dramatic, and taking into account of currently established mitigation techniques, it is not clear which system is the most robust. For instance, there is a large number of interference mitigation

techniques specifically developed for FMCW systems, as compared to PMCW systems, as noted in [81]. Therefore, although many of the methods are waveform independent and thus easily extendable to PMCW systems (e.g. beamforming, frequency agility), there is still a large hole in the PMCW literature which may hinder practictioners and engineers from implementeing efficient systems. However, as noted [59], PMCW systems share many similarities with CDM communication systems which has been subjected to an extensive amount of research on the topic. As concluded, this is still a topic of research and is therefore yet not established for the radar use case.

Finally, cost is yet an aspect with no definitive answer — in [64] it was claimed that PMCW is cheaper due to tight integration and efficient 28 nm CMOS fabrication when compared with current state of the art silicon-germanium technology. However, there are yet no sensors available in the market, and at the time of writing, the only company developing commercial automotive PMCW systems is Uhnder, under the partnership with Magna, with the first product planned to be released in 2019-2020 [86, 87].

The purpose of this thesis is to make a futher exploration on these topics from a signal processing perspective, pin-pointing system and interference aspects, as well as attempting a comparison with current state-of-the-art FMCW systems. Specifically, a case study is carried out to investigate the performance differences between PMCW and FMCW systems under typical short range automotive requirements. Aspects on MIMO scaling is then considered with regards to the current emergence of large multi-transmit systems. Some topics of high performance processing is then considered, investigating the possible use of data adaption in the spatial domain to estimate the direction of arrivals of targets under difficult scenarios. A specific investigation of pulse compression filter design for the PMCW case is then considered since it is shown that the compression suffers significant sidelobe degradations in the presence of uncompensated Doppler shifts. In the final chapter, a method for mitigating mutual interference is proposed for both PMCW and FMCW systems.

1.3 Scope

It is well known that sometimes, hardware imperfections is the main factor limititing the achievable performance. This topic is considerable and very complicated, and includes everything from and between the waveform generators, antenna subsystems to the receive achitecture and analog to digital conversion, as well as the environment surrounding the radar components (e.g packaging) and the actual environment illuminated. Some typical factors

are, for instance, phase noise, oscillator leakage, antenna couplings, receiver nonlinearities and saturation. Sometimes even issues in the complex number representation, originating from in-phase and quadrature components not being orthogonal, can bottleneck the system by image band folding. These aspects, while being critical from a practical point of view, will not be considered in detail in this thesis. As will be shown, even in the absence of such non-idealities, there are still major bottlenecks limiting the performance of the systems considered.

1.4 Outline

Chapter 2: The objective of this chapter is to provide a set of signal models for both FMCW and PMCW systems. Admittedly long, there is, to the writer's (although limited) knowledge, no single textbook which covers both FMCW and PMCW models in one place at the same time. A part of the objective is therefore to have it all gathered in one place as a reference for future readers.

Chapter 3: In this chapter, the necessary background of radar waveforms is introduced in order to understand the main body of text. The intention is not to provide a complete treatment — for that, see the included references. Also, a short section on the Welch lower bound is included, illustrating that there is no such things as orthogonal waveforms (although one can construct sets to be orthogonal at certain regions).

Chapter 4: This chapter is about the typical procedures employed when practicing signal processing. First, a set of assumptions are imposed on the models introduced in Chapter 2, simplifying the treatment and allowing for efficient processing — typically at the cost of a certain model mismatch. The basics of pulse compression, Doppler processing and direction of arrival estimation is then covered as a background for the future analysis. A section on radar performance metrics derived from the idealized models is then presented in order to evaluate the system designs and performances in later chapters.

Chapter 5: In this chapter, a system analysis of the automotive radar requirements is carried out. First, an introduction to short, medium and long range specifications are introduced. A short range radar system design for both FMCW and PMCW radars is then considered as a case study and both system compared. Then, some aspects of MIMO are

discussed, showing the improved performance and concluding that PMCW is better in terms of up-scaling.

Chapter 6: This chapter is on high performance processing. First, data adaptive direction of arrival estimators are investigated for both small and larger MIMO systems under some corner-case scenarios. Then, pulse compression filters are designed in order to mitigate the effects of uncompensated Doppler.

Chapter 2

Signal models

A radar system does not differ much from a clockwatch. The principal task is to measure the round-trip time of a transmitted pulse scattered from an object in the receptive field. By relating the time to the speed of propagation, the range to the object can be deduced. For the systems considered in this thesis, the way of doing this turns out to be sole difference.

2.1 Overview

In the following, two types of radar systems will be considered. In the first type, which is known as frequency modulated continuous wave (FMCW) radar system, a linear frequency modulated (LFM) waveform, is transmitted, a so scalled *chirp*. The modulation implies that the instantaneous frequency changes linearly over time. Assuming the pulse duration is much longer than the round-trip time, the range can be deduced at any time instance by comparing the frequency of the currently received echo with the currently transmitted one. Since the frequency changes at a specific rate, the difference in frequency is used to calculate the round-trip time, which in turn gives the range.

Figure 2.1 illustrates how this may be implemented in practice by using a stretch processor. In the upper part of the figure, the chirp waveform that is transmitted is illustrated, consisting of a repetetive sequence of LFM pulses generated by the chirp generator. After generation, the LFM waveforms are assumed to be at radio frequency (RF), and are therefore subsequently transmitted. Simultaneously, the transmitted signal is sent to the mixer, which down-converts any received waveform, directly followed by low pass filtering (ADC), analog to digital conversion (ADC) and then typically stored in an on-board memory where

parameter estimation and data processing takes place. The stretch processing part is the mixing between the transmitted chirp and the received chirp, which in practice corresponds to a multiplication and results in a signal which consist of the instantaneous frequency difference, called the intermediate frequency (IF) and the instantaneous frequency sum. This down-conversion is sometimes also denoted as demodulation, or deramping. The role of the the low-pass filter (LPF) is to discard the frequency sum and only retain the intermediate frequency, which in turn can be related to the round-trip time since the chirp rate is known. This procedure significantly reduces the analog bandwidth and the required sampling rate by (depending on the system) a factor of 20 or even more while also reducing the complexity of the subsequent pulse compression to a set of fast Fourier transforms. For more details on the stretch processor, see for instance [38, 39].

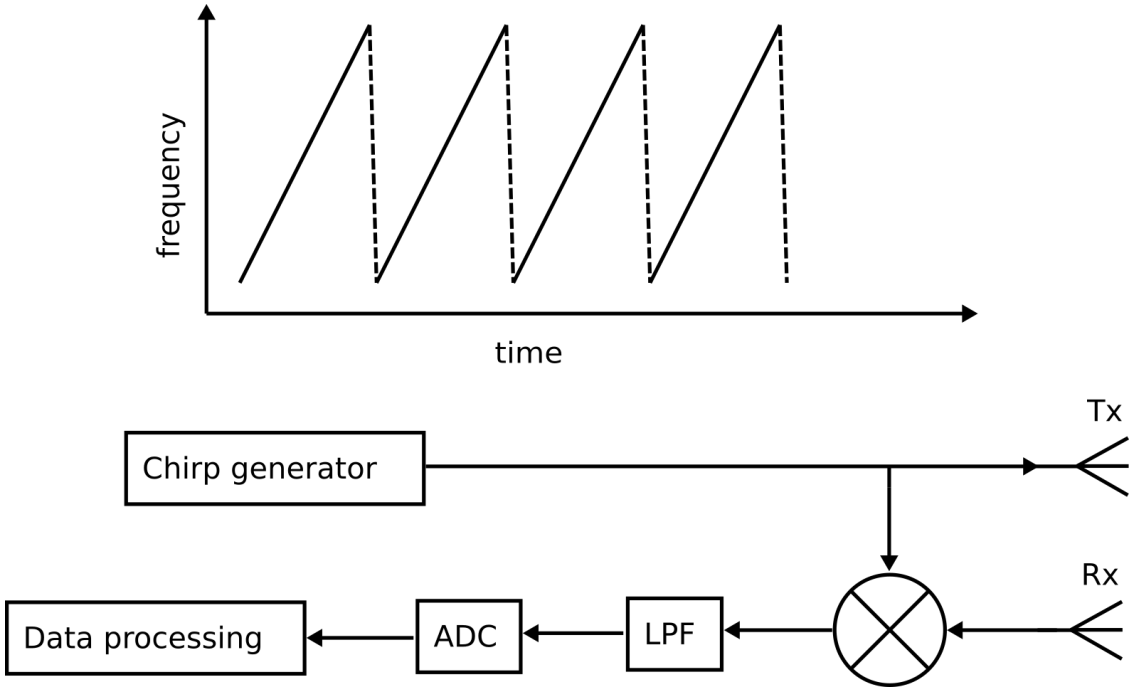

Figure 2.1: A high level view of a FMCW system using a stretch processor.

In the second type of system considered, the so called phase modulated continuous wave (PMCW) systems, a constant frequency waveform subjected to phase modulations is transmitted and the round-trip time measured directly, by comparing anything received with what was transmitted. While the phase modulation is not strictly needed for estimating the round-trip time, it turns out to make several targets resolvable.

Figure 2.2 illustrates how a PMCW system can be realized in practice, using a direct conversion architecture. In the upper part of the figure, the phase modulated waveform is

illustrated. We will only consider binary phase modulated waveforms, which in practice is a sequence of ones and zeros, where each step, or subpulse, is called chip and the entire waveform called sequence or phase code. The waveform is generated at baseband and upconverted to RF by the local oscillator (LO) prior to transmission. At reception, the waveform is down-converted to baseband, low pass filtered, digitized and then subjected to various stages of data processing in order to estimate the time delays. The range estimation is typically accomplished by a combination of correlations and accumulations.

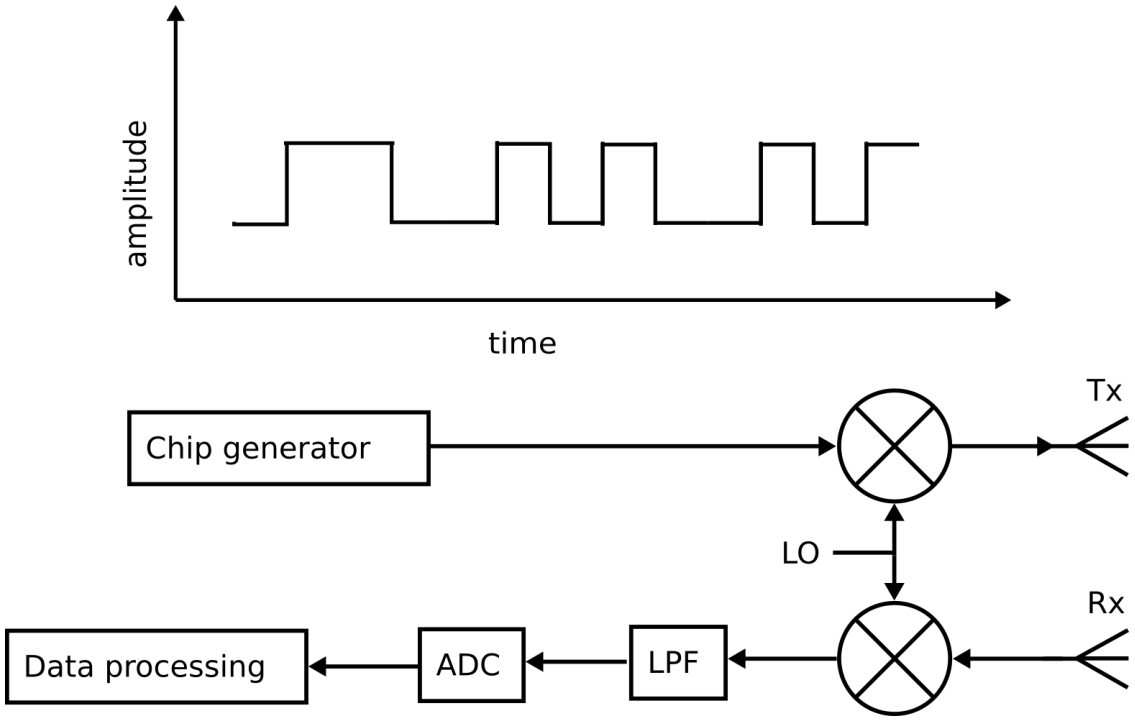

Figure 2.2: A high level view of a direct conversion PMCW system.

Since most systems transmit a sequence of multiple pulses over a CPI, two time scales (in addition to the total time elapsed) are commonly used to keep track of the times within each pulse as well as the times when each pulse was transmitted. These are known as fast time and slow time, and are illustrated in Figure 2.3a) and b). As shown in a), the fast time dimension corresponds to the time instances within a single pulse, while the slow time dimension to the time instances at the start of each transmitted pulse. In the following, these variables will be denoted as t_f and t_s.

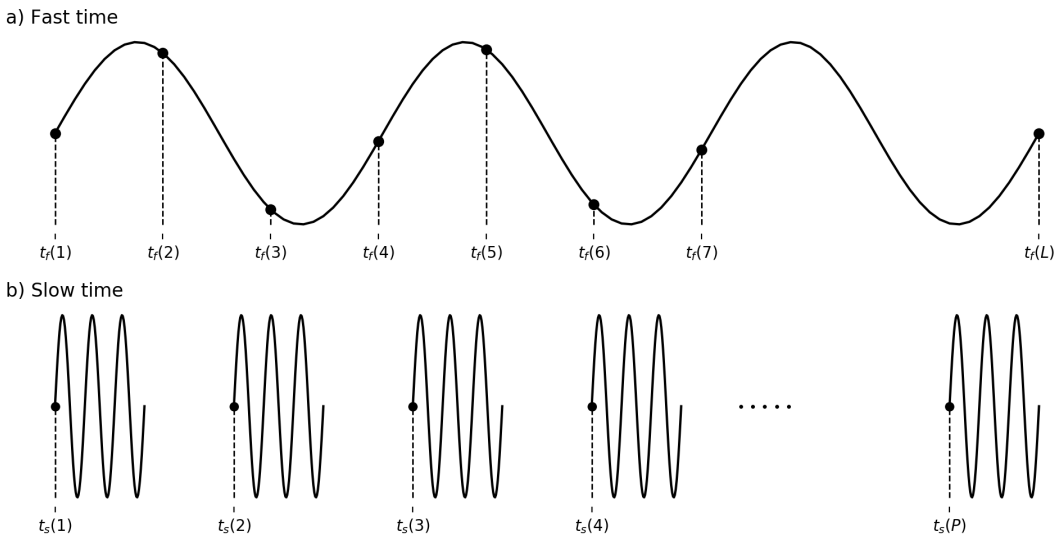

Figure 2.3: Illustration of the radar time scales. a) Fast time referes to the time instances between the start and the end of a pulse. b) Slow time refers to the time instances at which each pulse is transmitted.

2.2 Range-Doppler models

2.2.1 Phase modulated systems

Let $\phi(t)$ denote the baseband signal of a single transmitter at time $t = t_f + t_s$. After modulation with a carrier at frequency f_c, the transmitted signal is

$$y_{tx}(t_f, t_s) = \phi(t - t_s)\cos(2\pi f_c(t - t_s) + \psi) = \phi(t_f)\cos(2\pi f_c t_f + \psi) \tag{2.2.1}$$

where it is assumed that the waveform is transmitted every t_s and ψ represents an arbitrary phase term. Assuming a single point scatterer in the field of view, a single echo is returned with an (unspecified, possibly time varying and non-stationary) time delay $\tau = \tau(t) = \tau(t_f, t_s)$. The received signal is therefore

$$y_{rx}(t_f, t_s) = \phi(t_f - \tau)\cos(2\pi f_c(t_f - \tau) + \psi) \tag{2.2.2}$$

The signal $y_r(t_f, t_s)$ is then down-converted to baseband by mixing with the baseband carrier signal and low-pass filtered, yielding the in phase component

$$\mathrm{LPF}\big(y_{rx}(t_f, t_s)\cos(2\pi f_c t_f + \psi)\big) \approx \frac{1}{2}\phi(t_f - \tau)\cos(2\pi f_c \tau). \tag{2.2.3}$$

By performing the same procedure, but with the carrier instead phase-shifted $\pi/2$ radians, a phase unambiguity is be obtained and the analytic signal recovered, i.e., the in phase (I) and quadrature (Q) components are recovered. Therefore, the demodulated signal may be expressed by using the complex baseband representation

$$y(t_f, t_s) = \phi(t_f - \tau)e^{j2\pi f_c \tau} \tag{2.2.4}$$

which is the PMCW baseband range-Doppler model. It can be seen that there are two factors in the received signal, a time delayed replica of $\phi(t)$[1] and a phase modulation which depends on the time delays (motion) of the target. As will be shown in Section 4, the first factor can be used to estimate the range to the target, and the second to estimate the radial velocity, as well as the azimuth and elevation angles.

2.2.2 Linear frequency modulated systems

In the following, we will consider a chirp being transmitted, which in the "up" case is expressed in RF as $\cos(2\pi f_c t + \pi \frac{B}{T_c} t^2 + \psi)$ where f_c is the carried frequency, B is the bandwidth, T_c the chirp duration and ψ an abitrary phase offset. It should be noted that the instantaneous frequency is increasing linearly as $f_c + \frac{B}{T_c} t$, but that sometimes a linearly decreasing instaneous frequency might be used. As previously, the signal is transmitted at time instances t_s, yielding

$$y_{tx}(t_f, t_s) = \cos(2\pi f_c t_f + \pi \frac{B}{T_c} t_f^2 + \psi) \tag{2.2.5}$$

A scattered replica $y_{rx}(t_f, t_s)$ with time delay $\tau = \tau(t_f, t_s)$ is then obtained, given by

$$y_{rx}(t_f, t_s) = \cos(2\pi f_c (t_f - \tau) + \pi \frac{B}{T_c} (t_f - \tau)^2 + \psi) \tag{2.2.6}$$

The received signal is then demodulated with a copy of the transmitted signal and lowpass filtered, yielding the in-phase component

$$\mathrm{LPF}\big(y_{rx}(t_f, t_s) \cos(2\pi f_c t_f + \pi \frac{B}{T_c} t_f^2 + \psi)\big) \approx \cos(2\pi f_c \tau + 2\pi \frac{B}{T_c} t_f \tau - \pi \frac{B}{T_c} \tau^2) \tag{2.2.7}$$

[1] In Chapter 4, it will be shown that if the target is moving at a constant velocity, the waveform will also be subjected to compression and dilation effects. For the scenarios considered, these are however considered to be negligible.

and with the quadrature component one obtains the complex representation

$$y(t_f, t_s) = e^{j2\pi \frac{B}{T_c} t_f \tau - j\pi \frac{B}{T_c} \tau^2} e^{j2\pi f_c \tau} \tag{2.2.8}$$

which is the stretch LFM baseband range-Doppler model. Comparing with the model in eq. (2.2.4), one may notice a close resemblence. To see this, let $\phi(t_f, t_s; \tau) = e^{j2\pi \frac{B}{T_c} t_f \tau - j\pi \frac{B}{T_c} \tau^2}$, which allows eq. (2.2.8) to be expressed as

$$y(t_f, t_s) = \phi(t_f, t_s; \tau) e^{j2\pi f_c \tau} \tag{2.2.9}$$

which is the same form as (2.2.4).

Example: Range estimation of a stationary target

To illustrate how the range can be estimated, consider a stationary target with time delay $\tau = \tau_0 = \frac{2R_0}{c}$. The baseband signal is then

$$y(t_f, t_s) = e^{2\pi \frac{2BR_0}{cT_c} t_f} e^{-j\pi \frac{B}{T_c} \tau_0^2} e^{j2\pi f_c \tau_0} \tag{2.2.10}$$

Since all factors except the first are constant, estimating the range R_0 is simply a frequency estimation problem. The range may thus be estimated using, for instance, a Fourier transform in fast time. It turns out that this model holds approximately even when targets are moving moderately fast.

2.3 Interference models

The models derived in the previous sections do only consider the cases when the received waveform is synchronized with the receiver and no interferers are present. Since the receivers of each type of systems are different, the respective waveforms will also differ after down-conversion and filtering. In this section, the range-Doppler models are therefore extended to also include non-cooperative interferers from both type of systems. Four models will be considered, describing the PMCW-PMCW, FMCW-PMCW, PMCW-FMCW and FMCW-FMCW interference cases, where the system before the hyphen is the interferer and the system after the victim (that is, FMCW-PMCW means a FMCW interfering on a PMCW). It will be shown that in all cases, except for PMCW-PMCW interference, the received baseband signal will in general be chirp-like.

2.3.1 Phase modulated systems

We will in the following use the same notation as previously defined, but with an interferer denoted by an additional superscript $(.)^{(l)}$, denoting the l:th interferer. Let $\phi^{(l)}(t)$ be the phase modulated baseband signal of the l:th interferer, at time $t = t_f^{(l)} + t_s^{(l)}$ where $t_f^{(l)}$ and $t_s^{(l)}$ is the fast and slow time variables for the interferer, respectively. The time interpretations are as previously, fast time corresponds to the time as measured from the start of each pulse and slow time the time instances each pulse is transmitted. Let $y_{tx}^{(l)}(t)$ be the upconverted transmitted signal from the l:th interferer, given as

$$y_{tx}^{(l)}(t) = \phi^{(l)}(t - t_s^{(l)}) \cos(2\pi f_c^{(l)}(t - t_s^{(l)}) + \psi^{(l)}) \tag{2.3.1}$$

where $f_c^{(l)}$ denotes the carrier frequency and $\psi^{(l)}$ an arbitrary phase offset. The signal will reach the operating radar system of interest, with a time delay $\tau = \tau(t) = \tau(t_f, t_s) = \tau(t_f^{(l)}, t_s^{(l)})$, and then demodulated and down-converted, yielding the received signal $y(t_f, t_s)$ as viewed from the perspective of the operating radar. Following the same steps as previously, one obtains

$$y^{(l)}(t_f, t_s) = \text{LPF}\left(\phi^{(l)}(t_f + t_s - t_s^{(l)} - \tau^{(l)}) e^{j2\pi f_c^{(l)}\tau^{(l)}} e^{j2\pi f_\Delta^{(l)}(t)} e^{j(\psi - \psi^{(l)})}\right) \tag{2.3.2}$$

where $\tau^{(l)}$ is the direct path propagation time between the radar systems and $f_\Delta^{(l)}(t) = f_c(t - t_s) - f_c^{(l)}(t - t_s^{(l)})$ is a frequency modulation which depends on the relative PRFs and carrier frequencies. We note some immediate differences when compared with eq. (2.2.4). First, there are two modulation factors. The first, which depends on $\tau^{(l)}$ depends on the carrier frequency of the interferering radar system instead of the operating radar systems carrier frequency. The second factor consisting of $f_\Delta^{(l)}(t)$ is a modulation factor which captures carrier frequency and PRI differences and will introduce additional distortions to the baseband signal $\phi(t)$. Finally, as can be seen, if $t_s = t_s^{(l)}$, $f_c = f_c^{(l)}$ and $\psi = \psi^{(l)}$, the same model as in eq. (2.2.4) is obtained.

Example: Two stationary PMCW systems

As an example, we will consider two identical stationary radar systems but with different carrier frequencies. This scenario would for instance be prevalent when two-self driving cars of the same model are waiting in a traffic intersection. The situation implies that $\tau^{(l)} = \tau_0$ is constant and that the PRI parameters are equal, which yields constant slow time difference

$t_s - t_s^{(l)} = t_{s,0}$ (since the initial timings might differ). Thus, eq. (2.3.2) becomes

$$y^{(l)}(t_f, t_s) = \phi^{(l)}(t_f + t_{s,0} - \tau_0) e^{j2\pi(f_c - f_c^{(l)})t_f} e^{j2\pi f_c^{(l)}\tau_0} e^{-j2\pi f_c^{(l)} t_{s,0}} e^{j\Delta\psi} \tag{2.3.3}$$

Two points can be made. First, there is a time delay $\tau_0 - t_{s,0}$ which depends on the relative PRI timings of the systems. Since the PRI is on the order of several microseconds, which corresponds to several hundreds of meters, and since the systems are non-cooperative, this time delay will be completely random. Second, there is a fast time modulation term with frequency $f_c - f_c^{(l)}$, which will cause an additional pulse compression mismatch between the waveforms and possibly range smearing depending on the waveform used. Based on these two observations, an interferer may end up anywhere in range and may in addition mask weak targets in range, depending on the waveform range-response. However, since there are no slow-time modulations, the interferer will end up at zero Doppler (and may therefore be mitigated by e.g. MTI). However, it should be noted that it will only be non-zero Doppler if the timing parameters are exactly equal. If it is also assumed that the PRIs are only slightly different, this would end up a slow-time drift between the systems, resulting in a Doppler shift (and possibly even chirp-like modulation in slow time). The implications would be that the interferer would be entirely unpredictable in range-Doppler as well as additional smearings over the entire range-Doppler map, which may significantly deteriorate the system.

□

We will now proceed to derive the equations describing how a FMCW system interfers with a PMCW system. The transmitted LFM signal from the interferer is

$$y_{tx}^{(l)}(t_f, t_s) = \cos(2\pi f_c^{(l)}(t - t_s^{(l)}) + \pi\alpha^{(l)}(t - t_s^{(l)})^2 + \psi^{(l)}) \tag{2.3.4}$$

where as previously, the superscript $(.)^{(l)}$ denotes the l:th interferer and $\alpha^{(l)} = \frac{B^{(l)}}{T_c^{(l)}}$ is the corresponding chirp rate. The delayed signal, received in the PMCW system is

$$y_{rx}^{(l)}(t_f, t_s) = \cos(2\pi f_c^{(l)}(t - t_s^{(l)} - \tau^{(l)}) + \pi\alpha^{(l)}(t - t_s^{(l)} - \tau^{(l)})^2 + \psi^{(l)}) \tag{2.3.5}$$

The received signal is then in-phase and quadrature demodulated at constant frequency and low-pass filtered, yielding the complex baseband signal

$$y^{(l)}(t_f, t_s) = \mathrm{LPF}\big(e^{j2\pi f_\Delta^{(l)}(t)} e^{j2\pi f_c^{(l)}\tau^{(l)}} e^{-j\pi\alpha^{(l)}(t - t_s^{(l)} - \tau^{(l)})} e^{j(\psi - \psi^{(l)})}\big) \tag{2.3.6}$$

As can be seen by the third modulation, the received FMCW interference resembles itself as a

chirp at baseband. The starting frequency of the chirp will depend on the frequency difference between the radar systems as well as the relative time delays, as can be seen by the first and second modulations. The low-pass filter is still kept in this expression since the receiver will filter away any frequency components outside the analog receiver bandwidth.

Example: A coherent FMCW interferer

In this example, we will illustrate the case when a coherent interference is present. Under such circumstances, $f_c^{(l)} = f_c$, $t_s^{(l)} = t_s$, which yields the baseband signal

$$y^{(l)}(t) = e^{j2\pi f_c^{(l)}\tau^{(l)}} e^{-j\pi\alpha^{(l)}(t-t_s^{(l)}-\tau^{(l)})^2} e^{j(\psi-\psi^{(l)})} \tag{2.3.7}$$

which is simply a chirp with slope $\alpha^{(l)}$, modulated by the relative time delays between the systems.

2.3.2 Linear frequency modulated systems

We will now derive two range-Doppler models for the FMCW case. As will be seen, the models are slightly different when compared with phase modulated systems due to the stretch processor employed.

Denote as as previously the l:th interferer by the superscript $(.)^{(l)}$ and consider a phase modulated interferer. Then, the upconverted transmitted signal $y_{tx}^{(l)}(t)$ is

$$y_{tx}^{(l)}(t) = \phi^{(l)}(t - t_s^{(l)}) \cos(2\pi f_c^{(l)}(t - t_s^{(l)}) + \psi^{(l)}) \tag{2.3.8}$$

which is received by the victim after a time delay $\tau^{(l)}$. Since the victim is assumed to use a stretch processor, the signal is demodulated with $\cos(2\pi f_c t_f + \pi\alpha t_f^2\psi)$ and its quadrature component, and lowpass filtered, yielding the in-phase and quadrature signal

$$y(t_f, t_s) = \text{LPF}\left(\phi(t_f + t_s - t_s^{(l)} - \tau^{(l)}) e^{j2\pi f_c^{(l)}\tau^{(l)}} e^{j\pi\alpha t_f^2} e^{j2\pi f_\Delta^{(l)}(t)} e^{j(\psi-\psi^{(l)})}\right) \tag{2.3.9}$$

where $f_\Delta^{(l)}(t) = f_c(t - t_s) - f_c^{(l)}(t - t_s^{(l)})$. As can be seen, the interferer resembles a chirp due to the stretch processor. However, since $\phi^{(l)}(t)$ is pseudo-random, the signal will average out to zero and appear noise-like. In the case of an FMCW interferer, the transmitted signal

is

$$y_{tx}^{(l)}(t) = \cos(2\pi f_c^{(l)}(t - t_s^{(l)}) + \pi\alpha^{(l)}(t - t_s^{(l)})^2 + \psi^{(l)}) \tag{2.3.10}$$

and at reception, after complex demodulation and lowpass filtering, the received signal is

$$y^{(l)}(t_f, t_s) = \text{LPF}\left(e^{j2\pi f_c^{(l)}\tau^{(l)}} e^{j\pi\alpha(t-t_s)^2} e^{-j\pi\alpha^{(l)}(t-t_s^{(l)})^2} e^{j2\pi f_\Delta^{(l)}(t)} e^{j(\psi-\psi^{(l)})}\right) \tag{2.3.11}$$

and as can be seen, the interferer is essentially a lowpass filtered chirp at baseband.

Example: A scenario of FMCW-FMCW interference

To provide a concerete example, consider a scenario when two frequency modulated systems are interfering and assume that $t_s = t_s^{(l)} = 0$ and $\psi - \psi^{(l)} = 0$. Then, the interferer in eq. (2.3.11) can be simplified as

$$y^{(l)}(t_f, t_s) = \text{LPF}\left(e^{j2\pi f_c^{(l)}\tau^{(l)}} e^{j2\pi(f_c - f_c^{(l)})t_f} e^{j\pi(\alpha-\alpha^{(l)})t_f^2}\right) \tag{2.3.12}$$

which is a lowpass filtered chirp with start frequency $f_c - f_c^{(l)}$ and chirp rate $\alpha - \alpha^{(l)}$, which is the difference between the carrier frequencies and the chirp rates of the respective systems. Note also that there is a modulation factor with phase $f_c^{(l)}\tau^{(l)}$ which also affects the shape of the interferer, which is dependent on the motion of the interferer. This effect can sometimes be significant.

2.4 MIMO model

The single channel range-Doppler models presented in the previous sections will now be extended to the case when multiple transmitters and multiple receivers are operating simultaneously. We will illustrate for the case of a PMCW system, the other models follow analogously.

Consider the situation illustrated in Figure 2.4 and assume that there are M receivers and N transmitters, and that transmitter number n is radiating the waveform $\phi_n(t)$. Then, the received signal at receiver m will be the sum of all transmitted waveforms, scattered from the target. If it is also assumed that the radar system is designed so that each of the transmitters

and each of the receivers are separated in space, then, each of the transmitted waveforms will have a slightly different range to the target. Similarly, the range from the target to each each of the receivers will be different, and thus also having slightly different time delays. Therefore, the propagation time from the n:th transmitter to the m:th receiver will be $\tau + \tau_n^{tx} + \tau_m^{rx}$ where τ is the time delay as measured from some reference, and τ_n^{tx}, and τ_m^{rx} the additional time delays caused by the position of the n:th transmitter and m:th receiver relative to the frame of reference, respectively. The PMCW signal $y_m(t)$ in eq. (2.2.4), measured at the m:th receiver can therefore be written as

$$y_m(t) = \sum_{n=1}^{N} \phi_n(t_f - \tau - \tau_n^{tx} - \tau_m^{rx}) e^{j2\pi f_c(\tau + \tau_n^{tx} + \tau_m^{rx})} \tag{2.4.1}$$

It can be seen the single channel model is modified in two ways. First, each receiver will obtain the same sum of waveforms, but delayed by a time which depends on the overall location of the sensors. Second, the sum of waveforms will also experience a modulation, which in addition to the target also depends on location of the sensors. It will later in the signal processing section be shown that this spatial diversity can be used to estimate the direction of arrival of targets illuminated by the radar system, and that the additional transmitters will enhance this capability.

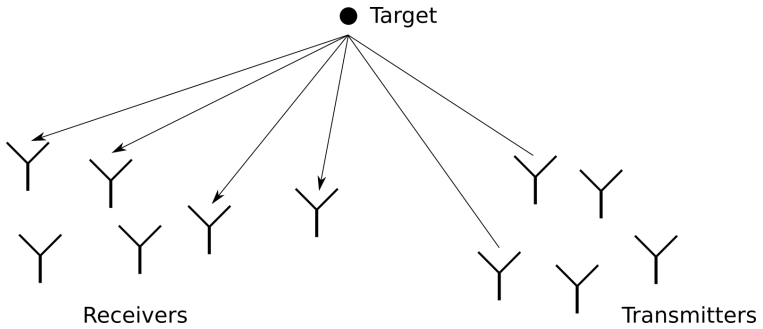

Figure 2.4: A MIMO array illuminating a target, illustrating the concept of spatial diversity.

2.5 Amplitude and noise models

In this section, some amplitude and noise models based on the radar range equation are presented. These results can be found in practically any radar textbook, in one form or another. The ones presented here were obtained from chapter 2 in [3]. We will first present the two-path model for the case of a single staring radar system, and then a single-path model for the case when jammers and other mutual interferers are present.

We note that while explicit dependencies on time, environmental, system and target characteristics are omitted from the models, many of the parameters are actually dependent on these quantities and may in certain situations have significant effects. Furthermore, while the received signal power is in theory deterministic, it is in practice highly dependent on the aspect angles which may significantly affect the radar cross section. The received power may therefore be treated as a stochastic random variable with an expected value around the range, Doppler and angle of interest, which is typically assumed constant during CPI, but with a radar cross section which follows a certain probability distribution. The Swerling models as introduced in [88] are famous approximations and allow for intra-pulse of inter-pulse variations by using relatively simple models. For the sake of simplicity, we will consider the amplitude as an unknown but constant variable which does not change over a CPI.

2.5.1 Two-path model

The received signal power P_r scattered from a target at range R and radar cross section σ is given by

$$P_r = \frac{P_t \lambda^2}{(4\pi)^3} \cdot \frac{G_t G_r}{R^4} \sigma \tag{2.5.1}$$

where P_t is the transmitted power, G_t and G_r the transmit and receive antenna gain, and λ the wavelength of the baseband carrier.

2.5.2 Single-path model

The received signal power $P_r^{(l)}$ from a single-path propagation from another system at range R is given by

$$P_r^{(l)} = \frac{G_r \lambda^2}{(4\pi)^2} \cdot \frac{P_t^{(l)} G_t^{(l)}}{R^2} \tag{2.5.2}$$

where $P_t^{(l)}$ is the transmit power and $G_t^{(l)}$ the transmit gain.

2.5.3 Thermal noise

The thermal noise power can be expressed as

$$P_n = k_B T B F \tag{2.5.3}$$

where B is the analog bandwidth of the receiver, F the noise factor, T the temperature, and k_B Boltzmanns constant.

2.5.4 Examples

To give the reader an impression of the order of magnitudes, we will now proceed with three examples.

Example 1: The signal strength of a target

Assume that a radar is operating with $G_t = G_r = 6$ dB and $P_t = 10$ dBm at 79 GHz. For a target at 30 meters, the receiver power is then -126.3 dBm for a target with $\sigma = -8$ dBsm, resembling a pedestrian [89].

Example 2: The signal strength of an interferer

Assume that a radar is operating with $G_r = 6$ dB dBm at 79 GHz and that there is an interferer present with $P_t^{(1)} = 10$ dBm and $G_t^{(1)} = 6$ dB. The received interference power is then -77.9 dBm at 30 meters.

Comparing with the received power from the previous example, a signal to interference ratio (SIR) of -48.4 dB is obtained. If the interferer would be at 5 or 100 meters instead, the received powers would be -62.3 and -88.4 dBm, yielding a SIR of -63.9 and -30.0 dB instead. These observations indicate that an interferer can be several orders of magnitudes higher in energy than the targets that one may want to detect.

Example 3: Thermal noise power, SNR and INR

Consider a PMCW system with a receive bandwidth of 1500 MHz and noise figure 15 dB, operating at 300° K. The thermal noise power is then -67.1 dBm. Comparing with the previ-

ous two examples, one then obtains a signal to noise ratio (SNR) of -59.2 dB and interference to noise ratio of INRs of 4.8, -10.8 and -21.3 dB at 5, 30 and 100 m, respectively.

Aa can be seen, the SNR is extremely low, and well below any form of detectability. This can be challenge in some radar systems. Fortunately however, the processing gains can be of several orders of magnitude due to the extremely large amount of data "flooding" through the ADCs. For instance, in the current example, at least 74.2 dB of processing gain is needed to get an SNR of 15 dB. Assuming for simplicity an entirely coherent processing, this would require the integration of a total of 26.3 megasamples, which may, for instance, be realized by processing of 4 receive channels at 1500 MHz in tandem over a CPI of 5 ms (assuming a 100% duty cycle).

Chapter 3

Radar waveforms

The purpose of a radar system is to actively (and sometimes passively) sense an environment for any backscattered echos from objects in the receptive field. The waveforms employed play a central role in the process, since they determine many key performance metrics. For instance, if multiple echos from multiple targets are received, each single waveform needs to be easily distinguishable from time shifted versions of itself. If multiple waveforms are used in a MIMO setting, each of those waveforms must also be distinguishable from each other. If in addition other, possibly non-cooperative systems are transmitting, the waveforms used must be chosen carefully as to minimize mutual interference. This problem of waveform design turns out to be rather difficult, specifically when taking the hardware and budget constraints into account, and has therefore extensively been considered in the literature.

The purpose of this chapter is to provide a very brief overview on radar waveforms specifically for binary PMCW systems. The concept of phase modulated waveforms is first introduced, along with some associated operations and metrics. Of concern will be waveforms with good auto- and cross correlation properties. A good autocorrelation indicates little ambiguities and a good pulse compression response, whereas if multiple waveforms are used simultaneously, the cross correlation properties will decide the amount of channel isolation achieveable. For this purpose, four binary waveforms used in this thesis are summarized, the maximum lengths sequences, Gold codes, almost perfect autocorrelation sequences and zero correlation zone sequences. What follows is a short overview of some MIMO multiplexing techniques. The chapter finishes with a discussion on the Welch lower bound. For a more complete treatment, see for instance [38, 90–92].

3.1 Phase modulation

When employing phase modulation, the baseband signal $\phi(t)$ has the following particular form:

$$\phi(t) = \sum_{k=1}^{L} s_k p_k(t) \tag{3.1.1}$$

where L is the number of symbols in the sequence, s_k the symbols of the phase code and $p_k(t)$ a shaping pulse with duration T_c. A unit-modulus constraint will be assumed, yielding $s_k = e^{j\varphi(k)}$ for some phase sequence $\varphi(k)$. It will also be assumed that the codes are binary, which yields $\varphi(k) \in \{0, \pi\}$ and therefore $s_k \in \{-1, 1\}$. In the case of a rectangular shaping function, one obtains

$$p_k(t) = \text{rect}\left(\frac{t - (k-1)T_c}{T_c}\right) \tag{3.1.2}$$

but for spectral efficiency reasons, other shapes might be used, such as gaussian windows or half cosines. In the following we will assume that the waveforms are sampled at time instances T_s, yielding

$$\phi(n) = \phi(nT_s) = \sum_{k=1}^{L} s_k p_k(nT_s), \quad n = 1 \dots L \tag{3.1.3}$$

In the representation, it has been implicitly assumed that $T_s = T_c$ since L samples were sampled over the waveforms, but note that sometimes one may want to oversample the waveform. The waveforms may further be classified as periodic or aperiodic. In this thesis, we will only consider periodic waveforms, which have the property of being L periodic, such that $\phi(n) = \phi(n+L)$. These waveforms are realized by transmitting the same code repeatedly at full duty cycle. At receive, the waveforms are typically subjected to pulse compression by matched filtering. The pulse compression response may be defined by periodic correlation function,

$$r_{\phi_1,\phi_2}(k) = \sum_{n=1}^{L} \phi_1(n)\phi_2^c((n-k) \bmod L), \quad k = -L+1 \dots L-1 \tag{3.1.4}$$

where $(.)^c$ denotes the complex conjugate. If a normalized response is considered, it means $r_{\phi_1,\phi_2}(k)/r_{\phi_1,\phi_2}(0)$ is evaluated. For a matched compression, $\phi_1(n) = \phi_2(n)$, where we denote $r_\phi(k) = r_{\phi_1,\phi_2}(k)$. If the target experiences Doppler modulations, one may consider the

periodic ambiguity function, meaning $\phi_1(n) = \phi(n)e^{j2\pi f_d n}$ and $\phi_2(n) = \phi(n)$, where f_d is the normalized Doppler. If the compression is mismatched, then $\phi_1(n) = \phi(n)$ and $\phi_2(n)$ is the mismatched filter. The (mismatched) periodic cross correlation and periodic cross ambiguity functions may similarly be defined, but for two different waveforms $\phi_1(n)$ and $\phi_2(n)$. The value of the periodic autocorrelation function between two samples can be obtained by linear interpolation if a rectangular shaping function is used [38].

Two metrics will be of particular interest: the integrated sidelobe level (ISL) and the maximum peak-to-sidelobe ratio (PSLR). Consider a set of m sequences $\{\phi_1(n), \ldots, \phi_m(n)\}$, then the metrics may be defined as

$$\text{PSLR} = \max_{k\neq 0, i\neq j} |r_{\phi_i,\phi_j}(k)|^2 \tag{3.1.5}$$

$$\text{ISR} = 2\sum_{i=1}^{m}\sum_{k=1}^{L-1} |r_{\phi_i}(k)|^2 + \sum_{i\neq j}\sum_{k=-L+1}^{L-1} |r_{\phi_i,\phi_j}(k)|^2 \tag{3.1.6}$$

When mismatched filters are used, some loss in processing gain (LPG) is typically expected, and is assessed by

$$\text{LPG} = 10\log_{10}\left(\frac{\left(\sum_{n=1}^{L}\hat{\phi}_n^c\phi_n\right)^2}{\sum_{n=1}^{L}|\hat{\phi}_n|^2\sum_{n=1}^{L}|\phi_n|^2}\right) \tag{3.1.7}$$

where $\hat{\phi}$ is the mismatched filter.

In the following, we will restrict ourselves to the four following binary sequences (although it should be noted that many other variants exist):

Maximum length sequences

Maximum length sequences, also known as pseudorandom noise sequences, have been used in multiple applications such as spread spectrum communications. Recently, they have also been considered for the use in automotive radar systems [93]. The short overview below follows the exposition in [94].

Let $h(x) = h_0x^q + h_1x^{q-1} + \ldots + h_q$ be a binary polynomial of order q, with $h_0 = h_q = 1$. If $h(x)$ is also a primitive polynomial, then the binary sequence u generated by $h(x)$ as

$$u_{i+q} = \sum_{k=0}^{q-1} h_{q-k} \oplus u_{i+k} \tag{3.1.8}$$

Table 3.1: A list of preferred pair primitive polynomials in binary representation. The polynomials should be read from left to right. For instance 100101 represents the polynomial $x^5 + x^2 + 1$.

Order	**Polynomial 1**	**Polynomial 2**
5	100101	111101
6	1000011	1100111
7	10001001	10001111
9	1000010001	1001011001
10	10000001001	10100001101
11	100100100101	100000000101

is said to be a maximum length sequence (m-sequence, or MLS) of degree q, where $\oplus$ defines the modulo-2 addition (exclusive OR). The vector consisting of the q initializing symbols, $u_0, u_1, \ldots, u_{q-1}$, is called the seed, and must be different from the zero vector. The sequences may be generated by linear feedback shift registers (LFSR), and have, among many other, the three following properties, where $L = 2^q - 1$,

1. For a given seed, the m-sequence repeats itself every L symbols (it is L-periodic).
2. Exactly L sequences can be generated, given by the L different periodic shifts.
3. After the mapping $\{0, 1\} \to \{-1, 1\}$, the normalized periodic autocorrelation function is two valued, having the value of $-1/L$ for all out of phase components.

Table 3.1 lists some primitive polynomials of order $q = 5, 6, 9, 10$. Figure 3.1 shows a maximum length sequence with $q = 5$ which has been subjected to the mapping $\{0, 1\} \to \{-1, 1\}$, corresponding to 0 and 180 degree phase shifts in eq. (3.1.1). As can be seen, the sequence is noise-like and has a flat autocorrelation function.

Gold codes

It turns out that when considering a larger set of m-sequences, the cross correlation properties are rather bad. A related kind of sequences is the family of Gold codes, which possess good cross correlation properties. To this end, Gold codes have been used in multiple applications, such as spread spectrum communications and satellite navigation. Similar to the overview on m-sequences, the following is based on [94].

Consider two different primitive polynomials, $h_1(x)$ and $h_2(x)$ each of order q. If the pair of m-sequences, u_1 and u_2, generated by the polynomials have a three valued (periodic) cross-correlation function, then the polynomials are said to be preferred. A set G of new sequences can then be generated from this pair of m-sequences by the pairwise modulo-2 additions of

the periodically shifted versions of each other,

$$G = \{u_1, u_2, u_1 \oplus u_2, u_1 \oplus T^1 u_2, \ldots, u_1 \oplus T^{L-1} u_2\} \tag{3.1.9}$$

where $L = 2^q - 1$ and T^k is a k-element periodic shift operator. The generated sequences in the set are called Gold codes and have also a three valued periodic cross (and auto) correlation function, with the highest value given by $2^{(q+2)/2} + 1$ if q is even and $2^{(q+1)/2} + 1$ if q is odd. As can be seen, the set consist of $L + 2$ sequences, corresponding to the L shifted pairs of modulo-2 additions along with the two original preferred m-sequences. The pair of polynomials illustrated in table 3.1 are also preferred (note that no preferred pairs exist for $q = 4, 8, 12, \ldots$). Figure 3.2 illustrates a Gold sequence with $q = 5$, along with the periodic auto- and the cross correlation functions obtained when correlating with another Gold sequence in the set.

Almost perfect autocorrelation sequences

Ideally, one wants perfect codes with all out of phase correlations being zero. However, this is not always possible, and a reasonable compromise is therefore sequences which are perfect almost everywhere. The use of almost perfect autocorrelation sequences (APAS) for automotive radar was first proposed in [69] as an approach to satisfy the high dynamic range scenarios that may be encountered. The following three properties were proven in [95]:

1. The number of symbols in APAS sequence must be a multiple of 4.
2. A sequence is an APAS if and only if the non-zero out-of-phase correlation coefficient is at lag $\frac{L}{2} - 1$.
3. The amplitude of the out-of-phase coefficient is $4 - L$.

Admittedly, the theory (and the construction) of these type of sequences appear rather complicated. For further details, see [69] and the references therein (specifically [96, 97]). The implementation used in this thesis is based on [98]. Figure 3.3 illustrates an APAS of length 60 along with its autocorrelation function. As can be seen, the autocorrelation is zero everywhere except in the middle.

Zero correlation zone sequences

Similarly to the case of APAS, one may further relax the requirements to only consider sequences which are orthogonal over certain regions. Such sequences are known as zero correlation zone (ZCZ) sequences and have been considered for the automotive case in, for instance [70, 99], where in the latter a single APAS was used by circularly shifting the

sequence equidistantly in time. Note that by definition, APAS are also a ZCZ sequences, defined by the regions at either side of the non-zero out-of-phase coefficient — specifically, the length of the ZCZ is $L/2-1$ since the non-zero peak is at the center. The zero correlation zones can in turn be split up into additional smaller zones by shifts, leading to range domain code multiplexing, as explained later.

In this thesis, we will use the construction scheme presented in [100], which allows for the design of multiple different sequences with a joint ZCZ (as compared with using a single shifted APAS) Figure 3.4 illustrates a constructed ZCZ sequence of length 32, along with the periodic autocorrelation function and the periodic cross correlation function obtained from the complementary ZCZ sequence. As can be seen, there are approximately 8 lags on either side of the in-phase component, indicating a zero correlation zone of 16 lags.

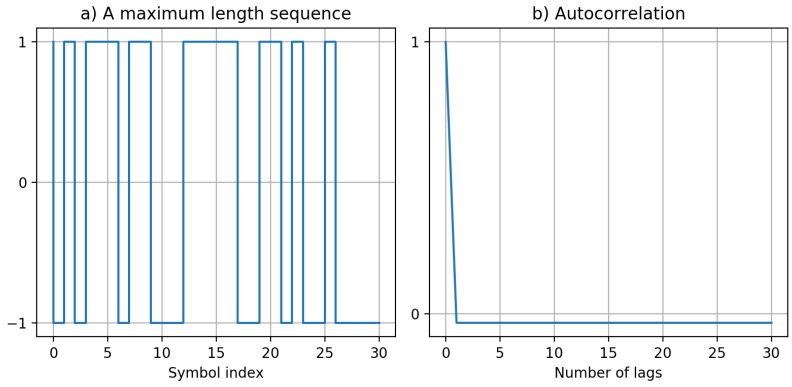

Figure 3.1: a) a maximum length sequence and b) its (periodic) autocorrelation function.

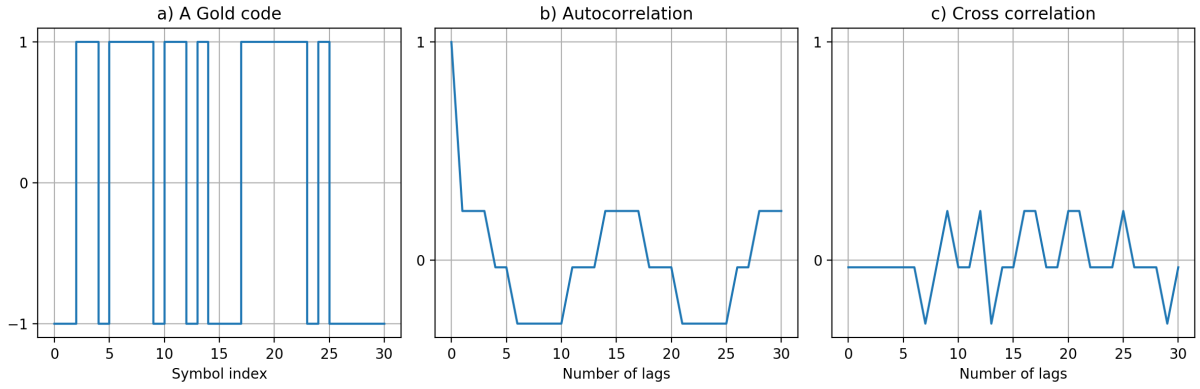

Figure 3.2: a) a Gold code and b) its (periodic) autocorrelation function. c) shows the (periodic) cross correlation function with another code.

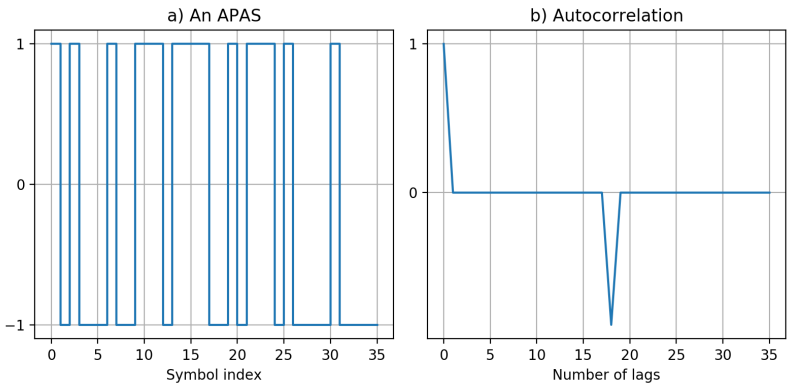

Figure 3.3: a) an almost perfect autocorrelation sequence and b) its (periodic) autocorrelation function.

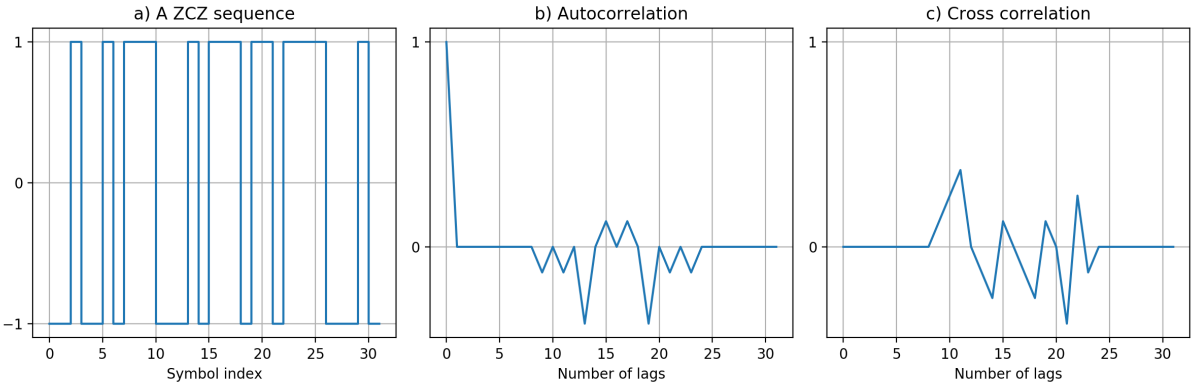

Figure 3.4: a) a ZCZ sequence and b) its (periodic) autocorrelation function. c) shows the (periodic) cross correlation function with a complementary ZCZ sequence.

3.2 MIMO multiplexing

Since MIMO multiplexing is a big topic in automotive radar (see e.g [93, 101–103]), a brief overview will be provided. Three types of schemes will be considered, time division multiplexing (TDM), frequency division multiplexing (FDM) and code division multiplexing (CDM). Within the CDM framework, three techniques are common - fast time, range domain and outer code multiplexing. Note that this section depends on the theory presented in Section 4.

Let $\boldsymbol{A}$ be a matrix (e.g a MIMO matrix) and $\boldsymbol{\Phi} = \boldsymbol{\Phi}(t) = [\boldsymbol{\phi}_1(t), \quad \boldsymbol{\phi}_2(t), \quad \dots \quad , \boldsymbol{\phi}_M(t)]^T$ a set of M waveforms sampled at L points. The problem of multiplexing is essentially a pulse compression problem where the objective is to recover each of the individual transmit-receive channels, loosely stated as follows: Given a hypothesized target $\boldsymbol{A\Phi}$, design a receive filter $\hat{\boldsymbol{\Phi}}$ such that $\boldsymbol{A\Phi\Phi}^* \approx \boldsymbol{A}$. It should be noted that this problem is rather hard, since all of

the requirements in normal pulse compression also needs to be satisfied, indicating that in addition to good out-of-phase properties, each of the waveforms need to also be orthogonal. As stated by the Welch lower bound, uniformly orthogonal waveforms do not exist, and the effect of Doppler mismatch may impact the compression negatively, see e.g [104].

In order to keep the discussion short and distinguish the multiplexing techniques, we will in the following assume that each $\boldsymbol{\phi}_i$ are sufficiently orthogonal when matched out of phase individually (i.e low sidelobes).

Code division multiplexing

The most intuitive solution to the problem is by employing fast time CDM. Under such circumstances, $\boldsymbol{\Phi}$ contains a set of "orthogonal" waveforms, and $\boldsymbol{A}$ is simply recovered by the procedure

$$\boldsymbol{A}\boldsymbol{\Phi}\boldsymbol{\Phi}^* \approx \boldsymbol{A} \tag{3.2.1}$$

If using range domain CDM, the same set of waveforms in $\boldsymbol{\Phi}$ are used, but cyclically time shifted with respect to each other, such that they are cross-orthogonal in the autocorrelation domain. However, for a fixed pulse length, this has the downside of reducing the maximum unambiguous range by the number of transmitters.

In outer code divison multiplexing, the issue is solved by transmitting multiple identical waveforms, but each modulated according to some scheme which allows for separation at reception. One scheme proposed for the automotive case is Hadamard codes [102]. To illustrate, assume 2 transmitters and let $\boldsymbol{H}_2$ be a Hadamard matrix of size two,

$$\boldsymbol{H}_2 = \begin{bmatrix} 1 & 1 \\ 1 & -1 \end{bmatrix} \tag{3.2.2}$$

then, if only $\boldsymbol{\phi}^T$ is transmitted, we can write $\boldsymbol{\Phi}$ as

$$\boldsymbol{\Phi} = \boldsymbol{H}_2 \otimes \boldsymbol{\phi}^T = \begin{bmatrix} 1 \cdot \boldsymbol{\phi}^T & 1 \cdot \boldsymbol{\phi}^T \\ 1 \cdot \boldsymbol{\phi}^T & -1 \cdot \boldsymbol{\phi}^T \end{bmatrix} \tag{3.2.3}$$

where $\otimes$ denotes the Kronecker product. The received signal is then compressed with the same transmitted waveform, yielding

$$\boldsymbol{A}\boldsymbol{\Phi}\boldsymbol{\Phi}^* = \boldsymbol{A} \begin{bmatrix} \boldsymbol{\phi}^T & \boldsymbol{\phi}^T \\ \boldsymbol{\phi}^T & -\boldsymbol{\phi}^T \end{bmatrix} \begin{bmatrix} \boldsymbol{\phi}^c & \boldsymbol{\phi}^c \\ \boldsymbol{\phi}^c & -\boldsymbol{\phi}^c \end{bmatrix} = \boldsymbol{A} \begin{bmatrix} 2\boldsymbol{\phi}^T\boldsymbol{\phi}^c & 0 \\ 0 & 2\boldsymbol{\phi}^T\boldsymbol{\phi}^c \end{bmatrix} = 2\boldsymbol{A} \tag{3.2.4}$$

Similarly, for M transmitters the procedure corresponds to transmitting $\boldsymbol{H}_M \otimes \boldsymbol{\phi}^T$ and then

compressing with $\boldsymbol{H}_M \otimes \boldsymbol{\phi}^T$. However, note that since periodic waveforms are commonly used, some kind of additional buffers are needed for reorganization of the data, depending on how the processing is set out. Note also that an M times longer PRI is needed, indicating a loss in maximum Doppler.

Time division multiplexing
In order to achieve orthogonality in TDM, each of the waveforms are interleaved in time at transmit. Conceptually, there is no difference between TDM and outer CDM (when using Hadamard codes). To see this, let $\boldsymbol{H}_M = \boldsymbol{I}_M$ be an identity matrix of size M. Then, as previously

$$\boldsymbol{A}\boldsymbol{\Phi}\boldsymbol{\Phi}^* = \boldsymbol{A}\begin{bmatrix}\boldsymbol{\phi}^T & \boldsymbol{0}^T \\ \boldsymbol{0}^T & \boldsymbol{\phi}^T\end{bmatrix}\begin{bmatrix}\boldsymbol{\phi}^c & \boldsymbol{0} \\ \boldsymbol{0} & \boldsymbol{\phi}^c\end{bmatrix} = \boldsymbol{A}\begin{bmatrix}1 & 0 \\ 0 & 1\end{bmatrix} = \boldsymbol{A} \tag{3.2.5}$$

Thus, for M transmitters the procedure corresponds to transmitting $\boldsymbol{I}_M \otimes \boldsymbol{\phi}^T$ and then matching with $\boldsymbol{I}_M \otimes \boldsymbol{\phi}^T$. Note that similar to outer CDM, an M times longer PRI is needed.

Frequency division multiplexing
In FDM, orthogonality is achieved by transmitting each of the waveforms at different frequency bands. The individual transmit-receive channels are then recovered by sampling the total bandwidth simultaneously and then isolating each component by bandpass filtering. After a data reorganization, pulse compression and standard data processing may then be continued as usual.

3.3 The Welch lower bound

It has been claimed that by employing orthogonal waveforms, one can completely eliminate all interference and co-existance problems. This is obviously not true and in this section we will show that no such waveforms exist as a direct consequence of the Welch lower bound (WLB).

Theorem 1. *The Welch lower bound*
Let $\boldsymbol{\phi} = \{\boldsymbol{\phi}_1 \;\; \boldsymbol{\phi}_2 \;\; \dots \;\; \boldsymbol{\phi}_m\}$ *be a set of* m *unit vectors in* $\mathbb{C}^n$. *Then, the maximum cross*

correlation c_{max} is bounded by

$$c_{max}^2 \geq \frac{m-n}{n(m-1)} \tag{3.3.1}$$

The proof is rather simple, and follows by connecting the Frobenius norm with the eigenvalues of the covariance matrix of $\boldsymbol{\phi}$, followed by Cauchy-Schwarz inequality and a simple sum inequality, see [105]. Loosely speaking, the theorem then tells us "how orthogonal" a set of m vectors can be in $\mathbb{C}^n$. Obviously, this is only meaningful if $m > n$ since otherwise c_{max} is bounded from below by a negative number, and it is well known from linear algebra that up to m vectors can easily be made orthogonal in an m-dimensional space.

Regarding the applications to radar, the bound is mostly interesting from a pulse compression perspective. Under such circumstances, using a periodic phase code, each of the cyclically shifted replicas need to be distinguished from each other after correlation processing (see Section 4.2). Thus, if a total of n symbols are used, there will be $m = n$ different waveforms, which yields $c_{max} = 0$, indicating the possibility of forming perfect codes. On the other hand, if instead p periodic phase codes are transmitted, then the total number of time-shifted waveforms becomes pn, and the WLB takes the form

$$c_{max}^2 \geq \frac{p-1}{pn-1} \tag{3.3.2}$$

Figure 3.5 illustrates the WLB with respect to the number of symbols in the sequences for various set sizes. It can be seen that in the case of $p = 2$ sequences, the lowest possible peak correlation level ranges from approximately -13 to -53 dB for sequence lengths ranging from 10 to 100000 symbols. It can further be seen that the bound decreases approximately 10 dB for every order of magnitude increase in the number of symbols. For sets consisting $m = 4$ or more sequences, the bound follows the same shape but is approximately 3 dB higher, ranging from -10 to -50 dB.

Put into perspective with the first application, modern automotive radar systems need to operate in dynamic ranges ranging in the order of 100 dB. For instance, in the 77 GHz band, pedestrians and cars may have a cross sections in the order of -5 dBsm and 35 dBsm, indicating a span of 40 dB if assuming equal range. Furthermore, assuming conventional correlation processing and that a detector with a 10 dB threshold is used, the dynamic range needs to be at least 50 dB. This corresponds to sequences containing the order 100000 symbols. Comparing with recently proposed systems [60,61], this appears difficult to implement, keeping in mind that even if such sequences were possible, they would be highly susceptible

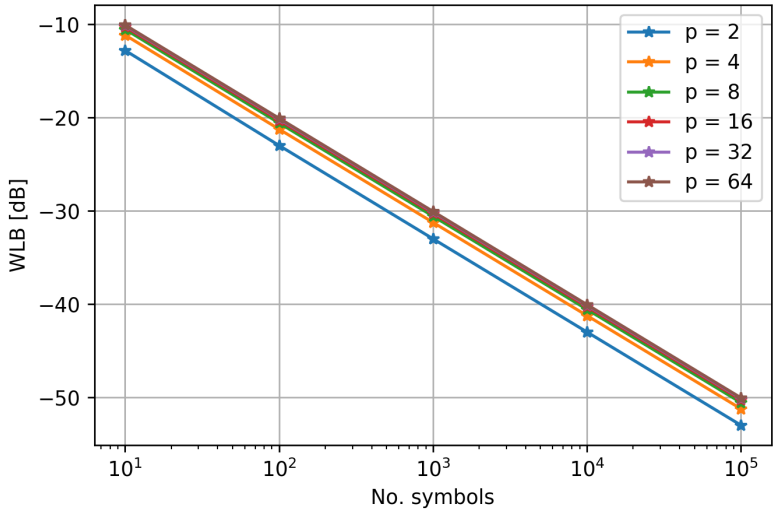

Figure 3.5: The WLB with respect to the number of symbols.

to Doppler degradation. Also if including the R^{-4} factor in the radar range equation, even longer sequences would be needed.

However, it is worth noting that sequences which are orthogonal at certain regions, so called zero correlation zones are possible. For instance, if $p = 4$ waveforms are used, but only the first $n/4$ range bins needs to be considered (this could for instance correspond to the range at which a signal is detectable), then the number of shifted waveforms becomes n and the cross correlation is bounded by zero, indicating a possible feasibility of orthogonality.

Chapter 4

Signal processing

Once the sensor data $\boldsymbol{Y}$ has been collected, the task of the signal processor is to determine whether targets are present, and if so establish an estimate of their parameters, such as position and identity. Put under the statistical framework of hypothesis testing, the formulation is then, given a certain set of target parameters such as range, Doppler and angles of arrival, to determine whether a hypothesized target $\boldsymbol{Y}_k$ can be deemed sufficiently different from noise, interference and clutter $\boldsymbol{N}$. That is, under the null hypothesis H_0, the target is considered absent, whereas under the alternative hypothesis H_1, the target is present

$$H_0 : \quad \boldsymbol{Y} = \boldsymbol{N} \tag{4.0.1}$$

$$H_1 : \quad \boldsymbol{Y} = \boldsymbol{Y}_k + \boldsymbol{N} \tag{4.0.2}$$

The optimal detection criteria is given by the Neyman-Pearson criteria, and multiple rules can be made to perform the hypothesis testing, such as the generalized likelihood ratio test. Typically, most common tests culminate in some form of whitening followed by thresholding, set by the noise, clutter and interference environment, where the target is deemed present if the energy of the hypothesis exceeds the threshold, see [3, 106]. Viewed from a more pragmatic setting, the purpose of all data processing before detection is to maximize the SNR (or SCR, SIR... or all of them, depending on the circumstances), in order to maximize the probability of detection and while simultaneously suppressing noise, clutter and interferecne to reduce the probability of false alarm. Once a target has been detected, the process of parameter estimation proceeds, which may include additional signal processing, conditioning, tracking and classification.

The actual data processing path can be rather complicated and done in many different ways.

We will consider the very simple scheme illustrated in Figure 4.1, which appears to be the most common one in automotive radar systems, as frequently indicated by the literature (see for instance [42]). First, the (conditioned) sensor data is subjected to pulse compression and Doppler processing. This is repeated for each channel, and if the transmitted signal is multiplexed at transmit, it also needs to be demultiplexed at receive. A non-coherent averaging is then typically performed, followed by some form of threshold detection. Typically, 10 dB above the noise floor is sufficient, as pointed out in [13]. The directions of arrival are then estimated, and the detections are then subjected to post processing, which may include clustering, tracking and classification. The final product is a set of target lists, which sole purpose is to provide a good understanding of the monitored environment.

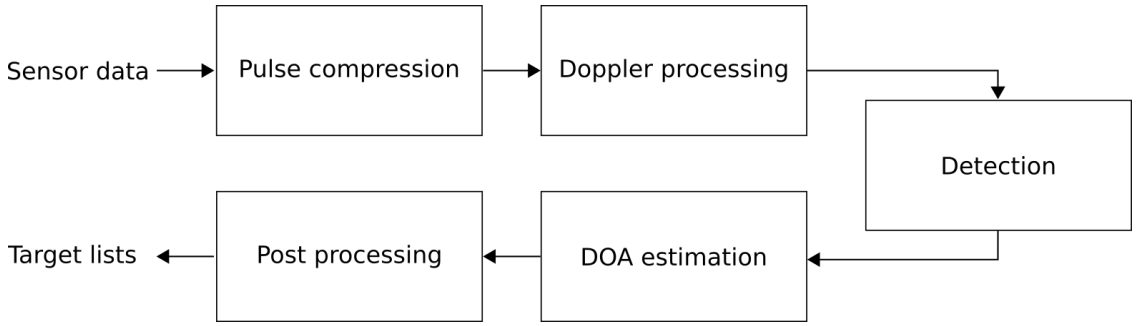

Figure 4.1: Illustration of the considered signal processing path.

In the following, we will present the basics of each block, excluding detection and post processing. However, as is typical in the engineering sciences, a set of assumptions are first imposed on the models developed in Section 2, followed by a series of approximations to make the following signal processing and interpretation tractable. Based on these results, some associated performance metrics are also presented, as a reference for future sections.

4.1 Model assumptions

4.1.1 MIMO assumptions

We will start by simplifying the MIMO model in eq. (2.4.1). As will be shown, the results are rather neat. Assume that the waveforms $\phi_n(t)$ are narrowband, which is a fair assumption since a 4 GHz bandwidth corresponds to a fractional bandwidth of approximately 5% at 79 GHz. Although, it should be noted some significant (although not dramatic) degradations

should be expected if employing an adaptive beamformer [107]. The assumption means that $\phi_n(t)$ varies slowly enough so that the MIMO time delays can be neglected

$$\phi_n(t_f - \tau - \tau_n^{tx} - \tau_m^{rx})e^{j2\pi f_c(\tau+\tau_n^{tx}+\tau_m^{rx})} \approx \phi_n(t_f - \tau)e^{j2\pi f_c(\tau+\tau_n^{tx}+\tau_m^{rx})} \tag{4.1.1}$$

What remains is then to find an expression on the time delays τ_n^{tx} and τ_m^{rx}. This may be achieved by the far field assumption, which implies that a plane wave approaches the array, and holds approximately whenever targets are further away than $2D^2/\lambda$, where D is the size of the MIMO aperture [3]. At 79 GHz and a 32 element ULA, this corresponds to approximately 2 meters, whereas if using 96 element ULA is used, as in [51], the far field is 17.5 meters away, indicating that this assumption is no longer valid over a significant range swath. Under such circumstances, one has to deal with the curvature of the wavefront. Nevertheless, under the assumption, the time delays can be written as [108, 109]

$$\tau_m^{rx} = \boldsymbol{g}_m^T \boldsymbol{p}(\theta, \varphi) \tag{4.1.2}$$

$$\tau_m^{tx} = \boldsymbol{g}_n^T \boldsymbol{p}(\theta, \varphi) \tag{4.1.3}$$

where $\boldsymbol{g}_m$ and $\boldsymbol{g}_n$ is the position of the m:th receiver and n:th transmitter, and $\boldsymbol{p}$ the target direction of propagation, given as

$$\boldsymbol{p} = [\cos(\theta)\sin(\varphi), \quad \sin(\theta)\sin(\varphi), \quad \cos(\varphi)]^T \tag{4.1.4}$$

where θ and φ are the azimuth and elevation angles. The model in eq. (2.4.1) then becomes

$$y_m(t) = b_m \sum_{n=1}^{N} a_n \phi_n(t_f - \tau)e^{j2\pi f_c \tau} \tag{4.1.5}$$

where $b_m = e^{j2\pi \boldsymbol{g}_m^T \boldsymbol{p}(\theta,\varphi)}$ and $a_n = e^{j2\pi \boldsymbol{g}_n^T \boldsymbol{p}(\theta,\varphi)}$. It can be seen that as a consequence of the narrowband and far-field assumptions, the range-Doppler and direction of arrival components have been separated out into two factors, simplifying the processing significantly. This is a celebrated result in array processing, and the exact same procedure can be done for the FMCW model in eq. (2.2.8), yielding the same model as above but with $\phi_n(t)$ being a multiplexed replica of the first modulation.

4.1.2 Target motion assumptions

We will now make the assumption that the targets are moving at a constant velocity v, which yields the time delay

$$\tau = \frac{2R_0 + 2vt}{c} = \tau_0 + \frac{2v}{c}(t_f + t_s) \tag{4.1.6}$$

The range-Doppler model in eq. (2.2.4) then becomes

$$y(t_f, t_s) = \phi \left(\underbrace{(1 - \frac{2v}{c})}_{a)\,dilation} t_f - \underbrace{\frac{2R_0}{c}}_{b)\,range} - \underbrace{\frac{2v}{c} t_s}_{c)\,migration} \right) \underbrace{e^{j2\pi f_d t_f}}_{d)\,mismatch} \underbrace{e^{j2\pi f_d t_s}}_{e)\,Doppler} e^{j\frac{4\pi R_0}{\lambda}} \tag{4.1.7}$$

where $f_d = \frac{2v}{\lambda}$ is the Doppler frequency. For clarity, the respective factors have been emphasized. The first factor in a) incurs a compression/dilation in fast time, caused by the target motion during pulse transmission. This effect can be safely neglected in automotive scenarios since relativistic velocities are unheard of. The second term in b), is the target range, which is to be estimated. However, the parameter is biased by the third term in c), which corresponds to a range migration in slow time. The effect may be substantial, specifically in high resolution radars when targets are moving fast. The fourth factor in d) corresponds to a Doppler modulation in fast time, which may cause a Doppler induced mismatch at pulse compression — the actual effect is typically studied using the ambiguity function. The fifth factor in e) is a Doppler modulation in slow time, which is typically used to estimate the target Doppler shift.

Simplifying the range-Doppler model in eq. (4.1.7), one may obtain a set of equations which are applicable under different regimes. We will consider the three below (were we have discarded the time constant phase and dilation/compression factors):

$$y_{a)}(t_f, t_s) = \phi \left(t_f - \frac{2R_0}{c} - \frac{2v}{c} t_s \right) e^{j2\pi f_d t_f} e^{j2\pi f_d t_s} \tag{4.1.8}$$

$$y_{b)}(t_f, t_s) = \phi \left(t_f - \frac{2R_0}{c} \right) e^{j2\pi f_d t_f} e^{j2\pi f_d t_s} \tag{4.1.9}$$

$$y_{c)}(t_f, t_s) = \phi \left(t_f - \frac{2R_0}{c} \right) e^{j2\pi f_d t_s} \tag{4.1.10}$$

which correspond to the modes a) high range resolution and high Doppler, b) high Doppler and c) low Doppler.

One may form the same set of equations for the FMCW model. Consider the range response $\phi(t_f, t_s; \tau)$ in eq. (2.2.9), and neglect the second quadratic modulation. Then, under the constant velocity assumption (and neglecting range migration in fast time) one obtains

$$\phi(t_f, t_s; \tau) \approx e^{j2\pi \frac{2B}{cT_c}(R_0 + vt_s)t_f} \tag{4.1.11}$$

and consequently the model approximation (ignoring the phase constants)

$$y(t_f, t_s) = \underbrace{e^{j2\pi\left(\frac{2B}{cT_c}(R_0+vt_s)+f_d\right)t_f}}_{a)\,range} \underbrace{e^{j2\pi f_d t_s}}_{b)\,Doppler} \tag{4.1.12}$$

As illustrated, the model consists of two main components. The range information can be found in a), where also the corresponding range-migration and fast time Doppler modulation is present, biasing the range estimate. In b), there is a Doppler modulation in slow time. Since the Doppler modulation in fast time only biases the result, only two models are considered, yielding

$$y_{d)}(t_f, t_s) = e^{j2\pi\left(\frac{2B}{cT_c}(R_0+vt_s)+f_d\right)t_f} e^{j2\pi f_d t_s} \tag{4.1.13}$$

$$y_{e)}(t_f, t_s) = e^{j2\pi\left(\frac{2B}{cT_c}R_0+f_d\right)t_f} e^{j2\pi f_d t_s} \tag{4.1.14}$$

As can be seen, both baseband models are entirely complex sinusoidal, with d) also showing a range migration phase cross term, attributing the well known range-Doppler coupling present in chirp radar systems, see e.g. [3,39,40]. The model approximation in e) is entirely sinusoidal. We conclude this section by noting that the FMCW model is rather complicated, since we have neglected many factors which may in fact be significant under certain scenarios.

4.1.3 Signal processing model

We are now ready to summarize the model development and realize the final signal models which the signal processing will be build upon. Using vector notation, we will express $\boldsymbol{a}(\theta, \varphi) \in \mathbb{C}^{N\times 1}$, $\boldsymbol{b}(\theta, \varphi) \in \mathbb{C}^{M\times 1}$ and $\boldsymbol{A}(\theta, \varphi) \in \mathbb{C}^{M\times N}$ as

$$\boldsymbol{a}(\theta, \varphi) = \begin{bmatrix} a_1(\theta, \varphi) & a_2(\theta, \varphi), \ldots, a_N(\theta, \varphi) \end{bmatrix}^T \tag{4.1.15}$$

$$\boldsymbol{b}(\theta, \varphi) = \begin{bmatrix} b_1(\theta, \varphi) & b_2(\theta, \varphi), \ldots, b_M(\theta, \varphi) \end{bmatrix}^T \tag{4.1.16}$$

$$\boldsymbol{A}(\theta, \varphi) = \boldsymbol{b}(\theta, \varphi)\boldsymbol{a}(\theta, \varphi)^T \tag{4.1.17}$$

where $\boldsymbol{a}(\theta,\varphi)$ and $\boldsymbol{b}(\theta,\varphi)$ are the transmit and receive steering vectors, and $\boldsymbol{A}(\theta,\varphi)$ the MIMO matrix. Furthermore, let $t_f = n_f T_s$ and $t_s = n_s T_p$, where $n_f = 1 \dots L$ and $n_s = 1 \dots P$. Then, each of the returned waveforms in eq. (4.1.8)-(4.1.10) and eq. (4.1.13)-(4.1.14) can be represented with respect to the fast-slow-time snapshots as $\phi(n_f, n_s; R, v)$. The N received waveforms $\boldsymbol{\Phi}(n_s; R, v) \in \mathbb{C}^{N \times L}$ at snapshot n_s can be expressed as

$$\boldsymbol{\Phi}(n_s; R, v) = [\boldsymbol{\phi}_1(n_s; R, v), \quad \boldsymbol{\phi}_2(n_s; R, v), \quad \dots \quad , \boldsymbol{\phi}_N(n_s, R, v)]^T \tag{4.1.18}$$

where each pulse $\boldsymbol{\phi}_n(n_s; R, v) \in \mathbb{C}^{L \times 1}$ for $n = 1, \dots, N$ is

$$\boldsymbol{\phi}_n(n_s; R, v) = [\phi_n(1, n_s; R, v), \quad \phi_n(2, n_s; R, v), \quad \dots \quad , \phi_n(L, n_s; R, v)]^T \tag{4.1.19}$$

Under this notation, the returned echo from a target under any of the models in eq. (4.1.8)-(4.1.10) and eq. (4.1.13)-(4.1.14) can be expressed as

$$\boldsymbol{X}(n_s; R, v, \theta, \varphi) = \alpha e^{jwn_s} \boldsymbol{A}(\theta, \varphi) \boldsymbol{\Phi}(n_s; R, v) \tag{4.1.20}$$

where $w = \frac{4\pi v}{\lambda}$ is the normalized angular Doppler frequency and α the complex amplitude. In order to make the notation more readable, we will consider a target k with parameters α_k, R_k v_k, θ_k and φ_k and denote the received echo as

$$\boldsymbol{Y}_k(n_s) = \alpha_k e^{jw_k n_s} \boldsymbol{A}_k \boldsymbol{\Phi}_k = \alpha_k \boldsymbol{X}_k \tag{4.1.21}$$

where it is understood from the context whether $\boldsymbol{X}_k$ or $\boldsymbol{\Phi}_k$ depends on n_s or not, and where all of the target parameters are implicit in the matrice $\boldsymbol{A}_k = \boldsymbol{b}_k \boldsymbol{a}_k^T$ and $\boldsymbol{\Phi}_k$. For a set of K targets, the received signal is

$$\boldsymbol{Y}(n_s) = \sum_{k=1}^{K} \alpha_k e^{jw_k n_s} \boldsymbol{A}_k \boldsymbol{\Phi}_k + \boldsymbol{N} \tag{4.1.22}$$

where $\boldsymbol{N}$ represents the contribution from interference, clutter and noise. If not otherwise specified, it will be assumed to circularly symmetric complex normally distributed white noise with a conforming dimension. The reason for this is that it is the most tractable and easiest to approximate. In reality, however, the noise can be very complicated, see for instance [40].

4.2 Pulse compression

The pulse compression is typically the first stage in the data processing after the baseband data has been conditioned, with the purpose of matching the waveforms of the received echos as to increase the SNR and range resolution. Since the waveforms employed are typically in the order of microseconds, corresponding to a couple of hundred meters, while the actual resolution is in the order of centimeters, the waveform is said to be "compressed" into that particular range cell (or "bin"), which justifies the name pulse compression.

As was discussed previously, the received signal $\boldsymbol{Y}$ was said to consist of K targets. However, since the task at hand is to estimate the number of targets and their parameters, the number cannot be known beforehand. One may therefore instead consider a set of hypothetic targets $\boldsymbol{Y}_k$ with amplitude α_k over a discretized grid of ranges indexed by k, where the task is to determine whether the amplitude α_k is significantly different from zero or not. The way this is done is by correlating the expected waveform $\boldsymbol{\Phi}_k$ of $\boldsymbol{Y}_k$ with a matching filter $\hat{\boldsymbol{\Phi}}_k$. Under such circumstances, and neglecting Doppler, the compression is

$$\boldsymbol{Y}\hat{\boldsymbol{\Phi}}_k^* = \alpha_k \boldsymbol{A}_k \boldsymbol{\Phi}_k \hat{\boldsymbol{\Phi}}_k^* + \sum_{l \neq k} \alpha_l \boldsymbol{A}_l \boldsymbol{\Phi}_l \hat{\boldsymbol{\Phi}}_k^* + \boldsymbol{n}\hat{\boldsymbol{\Phi}}_k^* \tag{4.2.1}$$

As can be seen, one would ideally want that $\boldsymbol{\Phi}_k \hat{\boldsymbol{\Phi}}_k^* = \boldsymbol{I}$ while simultaneously suppressing the clutter terms such that $\boldsymbol{\Phi}_l \hat{\boldsymbol{\Phi}}_k^* = 0$. The responses from the surrounding bins is known as sidelobe clutter, originating from adjacent targets. If the waveforms employed have good auto- and cross correlation properties (or is multiplexed well), then this contribution will be small. Note that if the waveform would only have good autocorrelation properties, but not good cross correlation properties then that contribution would be large, possibly higher than α_k and thus masking the true amplitude.

To elaborate further, the way the pulse compression is implemented depends on what kind of system is considered. In the case of FMCW, the compression may efficiently be implemented using fast fourier transforms, as indicated by the sinusoidal model in eq. (4.1.14). In the case of PMCW, a bank of parallell correlators and accumulators may be used [61].

The filter which maximizes the SNR is the matched filter [3], given as $\hat{\boldsymbol{\Phi}}_k = \boldsymbol{\Phi}_k$. Given an evaluated range bin, the filter will provide the best possible detection under the white noise assumption. However, it does not take into account of side effects such sidelobe clutter from neighbouring cells which may significantly bias the detection criteria and mask possible targets if rejected in a later detection stage. The matched filter is therefore suboptimal from

a SCR perspective and considering that automotive radars are often clutter limited [41], this is a big drawback and is the reason why practically all FMCW systems employ some form of windowing prior to compression in order to reduce the sidelobes — an operation which is nothing but mismatched filtering. See for instance [110, 111].

4.3 Doppler processing

Doppler processing is usually the second stage in the data processing. In the following, we will assume that the echos have been successfully compressed at each of the desired range bins, neglecting any residual Doppler. It will later be briefly discussed what to do when this assumption no longer holds. Under the said circumstances, the signal model after pulse compression, evaluated at a certain range bin, is

$$\boldsymbol{Y}(n_s) = \sum_{k=1}^{K} \alpha_k e^{jw_k n_s} \boldsymbol{A}_k + \boldsymbol{N} \tag{4.3.1}$$

where K is the number of targets present along the considered Doppler profile. The task is identically to the case of compression: to do sequence of hypothesis tests over a grid of Doppler shifts to determine whether targets at certain velocities are present in the evaluated range bin. Since the the signal along each transmit-receive channel $\boldsymbol{A}_k$ is a complex exponential, the corresponding matched filter is equivalent to a discrete fourier transform. Similarly to the case of pulse compression in FMCW systems, some form of tapering is usually required.

It turns out that different kind of targets reside at different regions in the Doppler subspace. Specifically, clutter is known to be localized along the low Doppler profiles whereas (moving) targets (of interest) usually reside in the high Doppler profiles. This is the motivation behind many of the Doppler processing techniques conventioanlly used, such as MTI [2, 3], which filters out unwanted echos around zero Doppler. As can be seen by the model in eq. (4.3.1), each Doppler return appears as a pure sinusoid, hinting that the processing is in fact "just" spectral analysis [112].

Another interesting topic which has attracted notable attention is that of microdoppler [113]. Since most targets are extended (when sufficiently close) the return will not consist of a single echo, but rather a sum of echos originating from different portions of the target. Each of these individual echos will experience (possibly time varying) Doppler shifts, which may

be identical or not. Thus, consider a single range bin and channel, and assume a single target which returns K echos, with the k:th echo having a Doppler shift $\Omega_k(n_s)$, then the microdoppler signature is

$$y(n_s) = \sum_{k=1}^{K} \alpha_k e^{j\Omega_k(n_s)} \tag{4.3.2}$$

To make a concrete example, pedestrians which are sufficiently close to the radar will scatter from, for instance, the torso, arms and legs. Since the body parts are different in size, they will have different α_k. Furthermore, if the pedestrian is walking, the arms and legs will be swaying back and forth, indicating certain phase-variations in $\Omega_k(n_s)$ for those particular body parts, usually oscillating around the Doppler of the torso which typically has a more low-pass character. In general the phase variations can be complicated, but idealized, one may consider the return as a synchronized sum of sinusoids. This kind of information can be used to distinguish various objects monitored by the radar, such as humans from animals, vehicles and clutter. To do so, one may for instance use time-frequency representations combined with some sort of feature extraction prior to classification, as discussed in [11]. In the cases of multiple targets, separation in Doppler can be problematic and a different approach was proposed in [114] were the microdoppler was extracted at the tracking level for target identification. Similarly, in [115], an implementation of a 24 GHz FMCW system was presented, including a system level description, which uses a support vector machine to discriminate humans post processing at the tracking level. The topic is still rather new and has been considered in, for instance [11, 116, 117], where deep learning approaches appears to give state of the art performance.

We will now briefly touch on two issues which are related to the Doppler and pulse compression. As can be seen by the signal models in eq. (4.1.8) and eq. (4.1.13), the range and Doppler parameters are coupled in the waveform by the fast and slow time modulations. This can cause certain performance losses when using the processing methods presented since there can be residual Doppler shifts present, which may degrade the pulse compression. In the case of chirping systems, the doppler shift typically results in a small range bias by the range-Doppler coupling, which is more often than not acceptable. However, uncompensated Doppler shifts may significantly degrade the pulse compression in PMCW systems, see for instance [80, 104]. Furthermore, if the radar has a sufficiently high range resolution and a target moving sufficiently fast, a migration over several range bins may occur during a dwell, so called range migration, which in turn may causes performance losses and target spread in the range-Doppler domain. These topics has therefore been studied in the lit-

erature, where several compensation approaches have been investigated. For instance, by employing a Doppler-first processing approach, the fast time modulations may be compensated for, as shown in [118], significantly reducing the associated range clutter. Similarly, it was demonstrated in [119] that by in addition performiing a fourier transform in fast time, the range migration can be compensated by taking chirp z-transforms along the Doppler profiles. The corresponding pulse compression is then performed on the Doppler and migration compensated data by taking an inverse fourier transform in fast time, following by conventional pulse compression. As also noted in the paper, these processing schemes are known as all-cell-doppler correction (ACDC) and all-cell migration compensation (ACMC), or simply keystone processing in synthetic aperture radar.

4.4 Direction of arrival estimation

By measuring the relative time of flight differences of the returned echos between a set of receivers, the direction of arrival (DOA) to the target can be estimated. It turns out that the process is specifically simple under the narrowband assumption, as previously introduced in Section 4.1, since then a time delay can be estimated with a phase shift.

Assume that the received signal has been compressed in range and processed in Doppler. Then, the signal model is

$$\boldsymbol{Y} = \sum_{k=1}^{K} \alpha_k \boldsymbol{A}_k \boldsymbol{R}_k + \boldsymbol{N} \tag{4.4.1}$$

where the $\boldsymbol{R}_k = \boldsymbol{\Phi}_k \hat{\boldsymbol{\Phi}}_k^*$ is the waveform covariance matrix, which ideally should be the identify matrix. However, due to non-orthogonality, it will color the channels (note that the noise will also be colored, but we will neglect this aspect). The task is to estimate the parameters $\{\theta_k, \varphi_k\}$. Let $\boldsymbol{y} = \text{vec}\{\boldsymbol{Y}\}$ be a vectorization of the data matrix, then

$$\boldsymbol{y} = \sum_{k=1}^{K} \alpha_k (\boldsymbol{R}_k^T \otimes \boldsymbol{I}_M) \text{vec}\{\boldsymbol{A}_k\} + \text{vec}\{\boldsymbol{N}\} \tag{4.4.2}$$

$$= \sum_{k=1}^{K} \alpha_k (\boldsymbol{R}_k^T \otimes \boldsymbol{I}_M) \boldsymbol{v}_k + \boldsymbol{n} \tag{4.4.3}$$

where ideally $\boldsymbol{R}_k^T \otimes \boldsymbol{I}_M \approx \boldsymbol{I}_{MN}$ and $\boldsymbol{v}_k$ is the MIMO steering vector. Here, the relation $\text{vec}\{\boldsymbol{AB}\} = (\boldsymbol{B}^T \otimes \boldsymbol{I})\text{vec}\{\boldsymbol{A}\}$ has been used [120]. As can be seen, non-orthogonality

in the transmitted waveforms affects the virtual array by a coupling, similar to the way conventional calibration errors affect normal arrays. However, this effect appear to be small for most reasonable radar waveforms. In the following, we will neglect this factor, and only consider the model

$$\boldsymbol{y} = \sum_{k=1}^{K} \alpha_k \boldsymbol{v}_k + \boldsymbol{n} \tag{4.4.4}$$

when doing DOA estimation. As previously, the direction of arrivals can be estimated by doing a hypothesis test over all possible $\boldsymbol{v}_k$ which are of interest.

4.5 Performance metrics

We will now present some performance metrics based on the simplified models in Section 4.1 and conventional processing in Section 4.2-4.4, as a reference for the coming sections. Three metrics will be considered in each of the measurables, the accuracy, resolution and ambiguity. While some of the derivations are rather simple, they are good for the intuition, and will therefore also be presented.

4.5.1 Range

We will start with the range resolution in the FMCW case. Consider the range component in the sinusoidal model in eq. (4.1.14), assume zero Doppler and that the waveform is sampled every T_s seconds over the pulse. Then, $t_f = T_s n$, where T_p/T_s is the number of samples. Since the range estimation problem is equivalent to a frequency estimation problem, the normalized resolution is then given by the inverse of the number of samples T_s/T_p [112]. The corresponding range resolution is given by

$$\Delta R = \frac{T_s}{T_c} \frac{cT_p}{2BT_s} = \frac{c}{2B} \tag{4.5.1}$$

As can be seen, the resolution depends only on the bandwidth B of the chirp. It turns out that the same relation also holds for general waveforms, and thus also in the PMCW case, see [3, 121]. For a waveform with pulse length T_p seconds, the maximum unambigous range

R_{max} is given by

$$R_{max} = \frac{cT_p}{2} \tag{4.5.2}$$

However, in the FMCW case, R_{max} is sometimes limited by the sampling rate $F_s = 1/T_s$. To see this, note that the maximum frequency is constrained by $1 = \frac{1}{\Delta R F_s T_p} R_{max}$, which yields $R_{max} = \Delta R F_s T_p$. Thus, the minimum sampling rate $F_{s,min}$ needed to achieve a given coverage is

$$F_{s,min} = \frac{R_{max}}{\Delta R T_p} \tag{4.5.3}$$

Note that the image band has been used to extend the range. Otherwise, one would need twice the sampling rate to satisfy a given R_{max}. The range accuracy δR can be assessed in multiple ways, for instance by using the Cramér-Rao lower bound [122, 123]. We will consider the approximate expression given in [13],

$$\Delta R = \delta R \sqrt{2SNR} \tag{4.5.4}$$

which relates the metric with the resolution and SNR.

4.5.2 Doppler

The Doppler can sometimes be seen as a sinusoid in slow time, as shown in Section 4.1. Thus, assuming a dwell time T_D, and scaling for the velocity, the resolution Δv is given by

$$\Delta v = \frac{\lambda}{2T_D} \tag{4.5.5}$$

which indicates that longer dwells increase the resolution. The maximum unambiguious velocity is determined by the PRF (which is the sampling rate), yielding

$$v_{max} = \pm \frac{\lambda}{4PRI} \tag{4.5.6}$$

where the maximum normalized Doppler was assumed ± 0.5 since both positive and negative velocities are of interest, as compared with the maximum unambiguous range in the FMCW case where only positive ranges are of interest. The velocity accuracy δv is assessed based

on [13], giving

$$\Delta v = \delta v \sqrt{2SNR} \tag{4.5.7}$$

4.5.3 Direction of arrival

Assessing the performance of DOA estimation can be tricky, since there is a long standing history of using data adaptive methods and nonuniform arrays, which might make some conventional assessments rather pessimistic. Under such circumstances, a simple, although expensive way of estimating the performance is by performing statistical analysis using Monte-Carlo simulations under realistic target environments. However, more recently analytical results on the performance bounds have emerged, see e.g. [124].

Under the data independent matched filtering framework, the performance is bounded similarly as for the range and Doppler counterparts. Assume a uniform linear array (ULA) with half wavelength element spacing $d = \lambda/2$, then the spatial frequency resolution is given by

$$\Delta f = \frac{d}{\lambda} \left(\sin(\theta + \Delta\theta) - \sin(\theta) \right) = \frac{1}{N_{vx}} \tag{4.5.8}$$

where N_{vx} is the number of elements. An estimate of the resolution $\Delta\theta$ can be obtained from the following approximation

$$\sin(\theta + \Delta\theta) - \sin(\theta) \approx \cos(\theta)\Delta\theta \tag{4.5.9}$$

which yields

$$\Delta\theta \approx \frac{2}{N_{vx}} \text{ radians} \approx \frac{120}{N_{vx}} \text{ degrees} \tag{4.5.10}$$

Note that if tapering is used, then the resolution will be worse, see for instance [112]. For the section on system analysis, we will also need the following approximate expression [13],

$$\Delta\theta = \delta\theta \sqrt{2SNR} \tag{4.5.11}$$

which relates the angular resultion with the accuracy $\delta\theta$.

Chapter 5

Radar system analysis

The purpose of this section is to make a comparison between FMCW and PMCW radar systems from a signal procesing and system perspective. To accomplish this, the current requirements of automotive radar systems are first presented, where bottlenecks are pinpointed and the requirements for future systems examined. A short range radar use case for parking assistance is then considered, where the previous requirements are adjustment for the particular scenario. A FMCW and a PMCW radar system are then designed for the particular use case, which are then jointly compared.

It is first shown that PMCW radar systems have better range resolution and high contrasting capabilities than FMCW systems under conventional processing frameworks, while FMCW systems are less prone to Doppler induced performance degradations, which may otherwise mask certain targets under certain scenarios. When evaluating the systems in the angular domain, no significant difference is found for the considered scenarios. The topic of MIMO scalibility is then considered, where it is shown that as a result of the direct sampling approach used in PMCW systems, the maximum amount of range-Doppler area is exploited by design, whereas for FMCW systems the area is bottlenecked by the required sampling rates imposed by the stretch processor. This property makes PMCW systems naturally more scalable from the point of currently employed systems, whereas realizing big MIMO FMCW systems will require a convergence towards direct IF sampling and digital pulse compression in order to scale properly. It is then finally illustrated that both systems experience slight Doppler degradations in the virtual array as a result of transmit multiplexing, but that the PMCW system is less sensitive due to the relatively fast MIMO switching.

5.1 General system requirements

Due to the almost infinite number of automotive radar use cases and scenarios, three representative type of systems were defined in [13] in order to simplify the design process. The designs are denoted as SRR, MRR and LRR for short-, medium-, and long range radar, respectively. The types of intended applications covered by sensors are numerous and include, for instance, adaptive cruise control, lane change assistance, forward collision avoidance, evasion assistance, cross traffic alert, obstacle detection, parking assistance, blind spot detection and rear collision warning.

The list of requirements for the SRR, MRR and LRR systems is presented in table 5.1 which shows the available frequency bands along with the allowed power transmissions as well as various resolution and accuracy requirements on range, Doppler, azimuth and elevation. It should be noted that the presented values are only representative and depend on the specific system, intended application and assumptions made, while the frequency and power regulations are absolute. These requirements, along with some others will be discussed in the next sections in order to provide a picture of the design problem.

Table 5.1: A list of automotive radar requirements for the LRR, MRR and SRR systems at the 76–81 GHz band as presented in [13].

Type	**LRR**	**MRR**	**SRR**
Maximum EIRP	55 dBm	-9 dBm/MHz	-9 dBm/MHz
Frequency band	76–77 GHz	77–81 GHz	77–81 GHz
Range swath	10–250 m	1–100 m	0.15-30 m
Range resolution	0.5 m	0.5 m	0.1 m
Range accuracy	0.1 m	0.1 m	0.02 m
Velocity resolution	2.2 km/h	2.2 km/h	2.2 km/h
Velocity accuracy	0.36 km/h	0.36 km/h	0.36 km/h
Angular accuracy	0.1°	0.5°	1.0°
3 dB beamwidth azimuth	± 15°	± 40°	± 80°
3 dB beamwidth elevation	± 5°	± 5°	± 10°

5.1.1 Dynamic range

The dynamic range of a radar system is the ratio between the strongest and weakest return that the system can handle to the extent that the signal processor can output accurate and unambiguous target detections, without an excessive number of false detections and spurious returns. The metric can be defined in mulitple ways depending on which part of the system that is considered. For instance, analog to digital converters have a dynamic

range which depends on the number of bits used, whereas the linear amplifiers used in the analog front end have a dynamic range which is determined by the 1 dB compression point and the level of the spurioses [3]. In the following, we will consider the dynamic range from a pulse compression and matched filtering perspective, which we define by the PSR after a filtering operation. The metric is important since it sets a limit on how detectable targets with small cross sections are when high cross section targets are closely situated. In [82], a similar notion using the term high contrast resolution was used to determine how detectable two close targets with high cross sectional differences are.

The dynamic range that needs to be handled in a radar system can be very large due to the R^{-4} scaling in the received power [3] and the variations in the radar cross section [13, 89, 125, 126]. Satisfying these requirements is a challenge, as pointed out in [13]. To get an impression of the levels that may be encountered, the worst case dynamic range can estimated by using the radar range equation, which is assessed as

$$\text{worst case dynamic range} = 40\log_{10}\left(\frac{R_{max}}{R_{min}}\right) + (\sigma_{max} - \sigma_{min}) + \gamma_{det} \tag{5.1.1}$$

where γ_{det} is a detection threshold. The value is typically set around 10–17 dB above the noise floor [3,13,121]. For the SRR system as specified in table 5.1, and a scenario consisting of a car and a pedestrian with 30 and -8 dBsm cross section [13,89], the worst case dynamic range becomes 140 dB when using a detection threshold of 10 dB. For the MRR and LRR systems, the corresponding values are 128 and 96 dB. This high dynamic range scenario may for instance occur when a car approaches the radar at close distances, while a pedestrian is walking further away. If both targets end up occupying the same Doppler bin, the range sidelobe level needs to be well below 100 dB, which puts high demands on the signal processor. It should be noted that 100 dB corresponds to a 5 decimal difference in a linear amplitude scale. The observation indicates that SRR systems need to handle higher power variations than MRR and LRR systems due to the short close raneg requirements, yielding dynamic ranges of well above 100 dB in the worst cases.

5.1.2 Angular accuracy and resolution

As shown in table 5.1, the angular accuracy requirements are set at 1.0, 0.5 and 0.1 degrees for SRR, MRR and LRR systems, respectively. At the maximum required ranges, the corresponding cross ranges are approximately 0.50, 0.85 and 0.44 meters. Based on these observations, it may be noted that LRR systems need higher accuracies to achieve the same

cross range performance at the maximum range when compared to MRR and LRR systems due to the amplification in cross-range. In general, the longer the operational range, the higher is the demand on good angular accuracy.

Continuing with the angular resolution, it appears that an actual value is difficult to assess since it depends on the intended application and the assumptions imposed on the possible scenarios. However, it is safe to say that if the systems are to be used in safety critical applications, then they must be able to properly handle almost all possible corner cases that may be encountered during an intended operation. This in turn will require an angular resolution in the order of degrees or less for scenarios when high range-Doppler resolution is insufficient. For instance, in [43], it was noted that in some adaptive cruise control and forward collision avoidance scenarios, specular multipath propagation might cause conventional signal processing approaches to be unreliable and that high resolution angular processing might instead be needed. Other possible corner cases, requiring high angular resolution in both azimuth and elevation include detecting small objects such as tires on the road, bridges and cars standing in tunnel openings. Furthermore, high angular resolution might be needed for certain applications such as lane change assistance. In [13], it was pointed out that an angular resolution of a couple of degrees or less might be needed for high performance, and in [127], it was concluded that high angular resolution is critical for future systems.

For the SRR, MRR and LRR accuracy requirements, the corresponding required resolutions at 15 dB SNR becomes approximately 8.0, 4.0 and 0.8 degrees when evaluated using eq. (4.5.11). Assuming conventional processing and a ULA with half wavelength spacing, the number of channels needed to satisfy these requirements, using eq. (4.5.10), is 15, 30 and 150, respectively, indicating that a rather large MIMO system is needed. However, it should be noted that the actual number of elements might be lower or higher in practice. For instance, array calibration errors may degrade the performance significantly [128–130], and some form of tapering might be needed to suppress sidelobes, at the cost of degraded resolution in order to obtain a sufficent dynamic range [112]. Similarly, numerous data adaptive methods may be used to surpass the resolution criteria [108, 112], with some simultaneously also being robust to calibration errors [112]. In [44], a method using MUSIC in the range-angle beamspace was used in an attempt to reduce the computational complexity while simultaneously achieving superresolution. In the Texas Instruments people tracking and counting reference design, Capon was used after range processing to obtain high resolution range-angle heat maps prior to Doppler processing [131]. To this end, there is a rich literature on direction of arrival estimators which can be used for both the single and multiple snapshot case depending on the signal processing pipeline employed (see for instance [108, 112, 132]). Although considered

somewhat risky, these methods may be used to compensate for the hardware required, at the cost of a significantly increased computational burden.

5.1.3 Range ambiguity, resolution and accuracy

The effects on the system design caused by the operating range requirements in table 5.1 will be slightly different depending if the system is linear frequency modulated and employs a strech processor or whether it is phase modulated with a correlator filter bank. In the latter case, the assessment is rather easy since the only requirement is that the pulse duration is long enough. For the specified cases of 250, 100 and 30 meters max range, the corresponding minimum pulse durations are given by the relation in eq. (4.5.2), which correspond to 1.7, 0.7 and 0.2 us respectively. However, typically one wants to match the maximum unambiguous range with the range at which the strongest possible target is well below the noise floor in order to avoid a target foldover to close ranges. In the FMCW case, the same limitation applies. However, since the pulses transmitted are typically in the order of 50 us, and since stretch processors predominantly used, the actual maximum unambiguous range usually is limited by the sampling rate, as shown in eq. (4.5.3), since targets further away will correspond to higher frequencies. Thus, the higher the sampling rate, the longer the maximum unambiguous range. Similarly, short pulses and high bandwidths correspond to shorter maximum ranges at a fixed sampling rate. As an example, a system with maximum range of 250 meters, bandwidth 300 MHz and sweep time 100 us will require a sampling rate of 5 MHz.

Regarding the minimum range requirements, at close ranges, a good transmit-receive isolation is necessary in order to avoid eclipsing. In the PMCW case, this requires minimizing transmit-receive spillover [61, 64] and in the FMCW case this also includes, among other things, minimizing the cross talk at the analog strech processing stage [40].

The range resolution requirements of 0.5, 0.5 and 0.1 meters for the LRR, MRR and SRR systems as illustrated in table 5.1, corresponds to a bandwidths of 300, 300 and 1500 MHz respectively. Using eq. (4.5.4), the required SNR to also satisfy the range accuracies is 11 dB for all three systems, which is harmonious with most threshold detectors.

5.1.4 Doppler ambiguity, resolution and accuracy

Doppler is important since it constitutes an independent dimension which can be used to enhance target discrimination. More importantly, for non-imaging systems with insufficient spatial resolution, clutter can be efficiently rejected via pulse Doppler processing or moving target indication [1, 3, 121]. The required resolution sets a limit on how short a dwell can be in a pulsed system, assuming conventional processing. For the systems presented in table 5.1, a resolution of 2.2 km/h is specified. In a 78 GHz system this corresponds to a shift of approximately 320 Hz, which yields a required dwell time of at least 3.1 ms. Given the specified accuracies in table 5.1, the required SNR is approximately 13 dB when using eq. (4.5.7), which is, similarly to the range requirements, consistent with the commonly used detection thresholds. However, it is worth noting that even longer dwell times will improve clutter suppression and detection of slowly moving targets. Another benefit which is the possible enhancement of achieving high resolution microdoppler signatures for target characterization, a feature which is becoming ever more prevalent in the radar literature (for an overview, see for instance [113–117].

Another important application specific consideration is the requirements on the maximum measureable unambiguous velocity. If assuming a non-staggered PRF, aliasing will occur if the Doppler shift exceeds half of the PRF. The effect is a possible foldover onto the low Doppler bins, potentially masking slow moving targets of interest. The problem can be alleviated by various disambiguation and foldover detection techniques, using for instance multiple frames with different PRFs together with the chinese remainder theorem [133] or by exploiting the transmit multiplexing in the MIMO system, see for instance [134] for the TDM case and [135] for the Hadamard CDM case. However, since the corrections are made post detection, the folding issues still remain. Furthermore, employing multiple PRFs may compromise the system requirements and exploiting the MIMO multiplexing becomes daunting when multiple transmitters are employed. Thus, while long pulses are desirable from a maximum range perspective, they will also lower the maximum Doppler. To get an impression on the orders of magnitude, an unambiguous measurement of targets moving with a relative radial velocity of 100, 200 and 300 km/h will require a PRI of maximum 34, 17 and 11 us respectively at 78 GHz. While these pulse lengths pose no restriction to phase modulated systems, frequency modulated systems with a stretch processor may get severely limited when also employing emplying multiple transmitters using time divsion or outer code multiplexing for increased spatial capabilities.

5.1.5 Multitarget detection capabilities

An important consideration of modern radar systems is the ability to detect and track multiple targets simultaneously. In the previous generation of automotive radars which used continuous wave, slow linear frequency modulation, frequency shift keying and various other methods, target disambiguation in the range-Doppler space was a limiting factor (see for instance [32] and the references therein). This eventually led to the mainstream fast chirping systems employed today, where each chirp duration is in the order of 90 us. Thus, this issue appears to no longer be a problem with the recently developed high PRF frequency and phase modulated systems.

5.1.6 A reference design from industry

To get an impression of how some real systems can be designed, we will now provide an example of an industrial system design developed by Texas Instruments. Specifically, the considered system, TIDEP-0092, is a SRR reference design based on the AWR1642 evaluation module which is a single chip FMCW radar sensor operating at the 76 to 81 GHz band [136]. The system is intended to be used in applications such as lane change assistance, autonomous parking, cross traffic alert and blind spot detection, and has an entire signal processing pipeline implemented on an integrated processing unit, including baseband processing and detection as well as data processing such as clustering and tracking.

The reference design employs a multi-mode system, combining both short range and ultra short range capabilities by switching between two modes, each employing different chirp waveforms. The short range mode uses a PRF switching scheme which allows for an extended unambiguous maximum velocity by a chinese remainder disambiguation, whereas the ultra short range mode runs at high bandwidth for accurate close range measurements. This design allows for tracking of strong scatterers such as cars at up to 80 meters while simultaneously generating point clouds for weaker targets at close ranges up to 20 meters at a higher resolution, with everything running on relatively cheap hardware.

As a reference to contrast the numbers in table 5.1, an overview of some of the system parameters is illustrated in table 5.2. As can be seen, the range and Doppler requirements are satisfied with large margins, whereas the angular resolution is not, when evaluated at an SNR of 15 dB. However, it should be noted that at least for the USRR mode, all of the requirements are satisfied at 20 dB SNR, indicating that whenever a target is well above the noise floor the system should function properly. Note also that the system does not have

any capabilities of resolving targets in elevation. The design choice is probably a trade-off between cost and hardware, since realizing many receivers is expensive.

Table 5.2: An overview of some system parameters in TIDEP-0092. [1]Evaluated at 15 dB SNR. [2]Increased from native with high level algorithms.

	SRR	**USRR**	**Unit**
Number of transmitters	1	2	
Number of receivers	4	4	
Effective chirp time	51	82	us
Time between chirps	5	5	us
Number of ADC samples	256	512	
ADC sampling frequency	5000	6250	ksps
Number of chirps	128	64	
Frame time	7.3	6.03	ms
Bandwidth	409	3456	MHz
Range resolution	36	4.3	cm
Range accuracy[1]	4.5	0.5	cm
Velocity resolution	0.94	1.13	km/h
Velocity accuracy[1]	0.12	0.14	km/h
Maximum velocity[2]	90	36	km/h
Azimuth resolution	30	15	degrees
Azimuth accuracy [1]	3.8	1.9	degrees

5.2 A short range radar case study

We will consider a SRR system designed for parking assistance. A fictive scenarios is illustrated in Figure 5.1 and consists of a rather crowded environment around a parking lot, where the drivers intention is to comfortably leave without having to fear the risk of collision. The role of the radar system is to provide a coherent view of the environment as to provide a complete situational awareness.

The considered system is based on the SRR requirements from table 5.1. However, small modifications will be made to fit the intended scenario slighty better. We will consider the range and Doppler resolution, field of view, and maximum unambiguous range and Doppler. The range and Doppler accuracies will be evaluated based on the corresponding resolutions. The angular estimation will be assessed based on the considered radar systems (i.e the available hardware), since there is typically little freedom in choosing the number of transmitters and receivers (although it should be noted that sparse configurations are possible, at the cost of certain trade-offs).

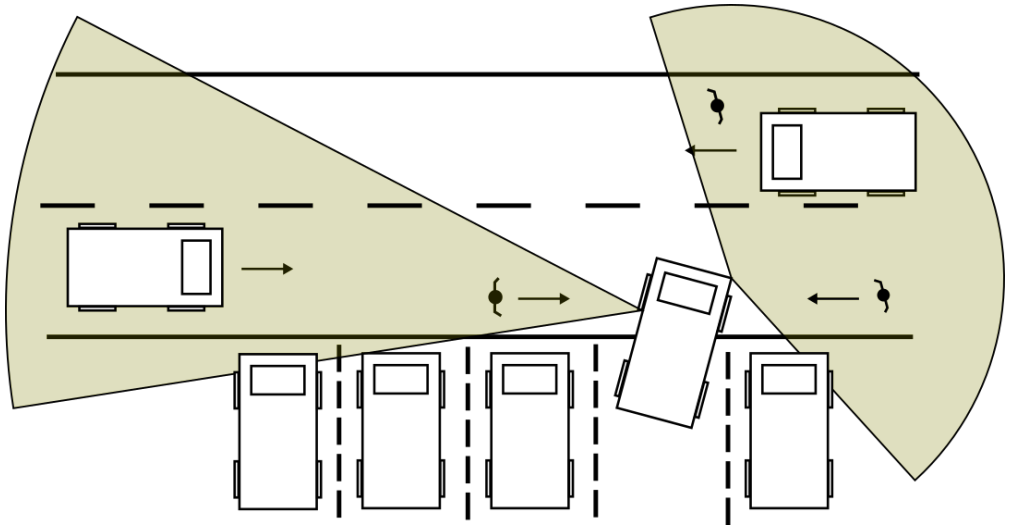

Figure 5.1: Illustration of a possible scenario in the use case considered.

5.2.1 System specifications

Doppler resolution: As compared to the value in table 5.1, we will increase the Doppler resolution from 2.2 to 0.5 km/h. This is to improve the detection of slowly moving targets such as pedestrians, which otherwise might be masked by strong clutter such as, for instance, bushes, trees or other swaying objects. Another considerable benefit is improved target recognition due to the enhanced microDoppler signatures, which may allow discriminating pedestrians from bicyclist, automotives and other clutter [113–117]. These advantages come at the price of a four times longer dwell which may impair the co-existance properties with other systems, as well as increasing the computational burden in the signal processor due to the increased amount of data which needs to be compressed at each frame.

Range resolution: The same range resolution as in table 5.1 will be used. However, it may be down prioritized for two reasons. First by decreasing the operating bandwidth more systems will be able to coexist in the frequency band. This might be an important trade off since many systems must be able to function simultaneously, even in the presence of tens of cars. Second, discriminating two objects sufficiently close at the same Doppler might not be a priority since they will most likely follow the same trajectory (assuming they are moving), or at least in a later time instance split up into two tracks when sufficiently spaced. Since the main objective is to increase the situational awareness as to avoid collisions, the knowledge of only one target present when it in fact was two closely spaced targets might not be that important for the application. However, it should be noted that poor resolution may lead to failure in certain corner cases and for a truly high performing system, high resolution is

of uttermost importance. This is obviously a design problem which needs to be addressed from a systems point of view.

Maximum Doppler: Since a possible scenario is the occurrence of cars driving in a main road, a maximum Doppler of at least 70 km/h will be required to guarantee that no aliasing occurs. It is here assumed that the car carrying the radar sensor is moving relatively slowly when leaving the parking lot. Nevertheless, it should be noted that the value can be increased or decreased depending on the post processing chain employed. For instance, the maximum velocity can be increased by disambiguation as previously noted, and since fast moving targets typically move non-radially, the target will move throughout the range-Doppler image, possibly masking different targets at each time instance. Certainly, a good target tracker should be able handle a few missing detections and thus alleviate the situation. Furthermore, assuming a stationary radar; in order to fold into zero Doppler and mask slowly moving targets, the target will have to move at twice the maximum unambiguous velocity, which in this case is 140 km/h.

In a trade-off between range resolution, maximum Doppler and hardware limitations (in this case a maximum possible IF bandwidth of 20 MHz in the later considered FMCW system), we will keep the range resolution as specified, and require a 70 km/h maximum unambiguous velocity. Obviously, this is a compromise and in a real implementation one would test many different configurations, some with higher maximum velocity and lower range resolution and vice versa, in order to ensure a satisfactory system.

Spatial resolution and accuracy: In current automotive systems, the spatial resolution is ultimately limited by the number of virtual receivers that can be used in the system. Furthermore, since it is rather hard to assess whether the range and Doppler resolution is sufficient, we will not consider this aspect any further – but only note that the situation might be alleviated algorithmically by using data adaptive methods.

Furthermore, imaging clutter (stationary targets) might be important in order to avoid colliding with targets such as, for instance, standing pedestrians, cones, pillars or railings; hence we will later also consider a small and large MIMO system.

Field of view: As mentioned in [137], a large field of view is required in order to obtain a good situational awareness – in this case we will follow the recommendations in table 5.1. However, it should be noted that this comes at the price of a reduced transmit and receive gain which may limit the operational range. This issue can obviously be (and is) solved by mounting multiple systems around the car - at the additional hardware cost, increased RF

Table 5.3: The requirements on the considered SRR system.

Parameter	**Value**	**Unit**
Maximum EIRP	-9	dBm/MHz
Frequency band	77-81	GHz
Range swath	0.15-30	m
Range resolution	0.1	m
Velocity resolution	0.5	km/h
Maximum velocity	70	km/h
3 dB beamwidth azimuth	± 80	degrees
3 dB beamwidth elevation	± 10	degrees

occupancy, and increased data processing (sensor fusion) and calibration complexity.

The system requirements are illustrated in table 5.3. We will now proceed to derive some additional parameters which are independent of the type of waveform employed. These are summarized in table 5.4.

Waveform bandwidth: The required range resolution is 0.1 meters, which corresponds to a bandwidth of 1500 MHz and an accuracy of 0.02 meters at 11 dB SNR, as shown previously.

Transmit and receive gain: The transmit and receive gain can be estimated as $G = 3.098\pi/(\theta_3\varphi_3) - L$ where φ_3 and θ_3 are the 3 dB beamwidths in azimuth and elevation respectively and L the associated losses [3]. By using the azimuth and elevation field of view as the 3 dB beamwidths, and setting a loss of 4 dB in transmit and receive, an estimate of the transmit and receive gain is 6 dB at the field of views of $\pm 80°$ and $\pm 10°$ in azimuth and elevation.

Transmit power: At the 1500 MHz bandwidth, the maximum EIRP becomes 22 dBm. This yields a maximum transmit power $P_{t,max} = 22 - G_t = 16$ dBm.

Pulse repetition interval: A maximum velocity of 70 km/h corresponds to a Doppler shift of approximately 10.2 kHz at 79 GHz. A PRF of 20.4 kHz will accordingly be needed to unambiguously sample the Doppler shift, which in turn corresponds to a PRI of approximately 49 us.

Dwell time: Similarly, a velocity resolution of 0.5 km/h corresponds to Doppler resolution of approximately 73 Hz, which in turn requires a dwell time of approximately 14 ms. This in implies that at least 286 pulses need to be transmitted during a CPI.

Table 5.4: The table shows some derived system parameters for the SRR case.

Parameter	Value	Unit
Receive gain	6	dB
Transmit gain	6	dB
Maximum transmit power	16	dBm
Pulse bandwidth	1500	MHz
Minimum PRI	49	us
Minimum dwell time	14	ms
Minimum number of pulses	286	
3 dB beamwidth elevation	± 10	degrees

5.2.2 Configuring a FMCW system

In the following, we will consider the AWR2243 developed at Texas Instruments as the hardware platform for the design [46]. An overview of some system parameters are illustrated in table 5.5.

Chirp parameters: In the system, three transmitters are available for improving the spatial diversity. In order to simplify the system analysis, we will consider time division multiplexing, although it should be noted that outer Hadamard coding is also possible in the AWR2243. Thus, all three transmitters must sequentially transmit a chirp during a PRI of 49 us, as specified in table 5.4. This yields a maximum chirp duration of 16.33 us, and a corresponding minimum ramp rate of 92 MHz/us, which is also satisfied by hardware, as given in table 5.5.

Sampling rates: Given the chirp rate and sweep time, the corresponding beat frequency at the maximum range of 30 m is 18.4 MHz, which satisfies the IF bandwidth requirement. Strong reflections from distances further away than 30 meters will not pose any problem and fold into close ranges since these are removed by the analog filters after the de-chirping in the analog front end.

It is worth nothing that if the maximum velocity requirement would have been 120 km/h, the chirp maximum chirp duration and minimum ramp rate would have corresponded to 9.33 us and 161 MHz/us respecteviely. This would yield a beat frequency of 32.2 MHz at 30 m, which is 60% above the 20 MHz IF bandwidth. The hardware would thus not support this configuration.

SNR analysis: We will proceed to evaluate the SNR obtained at 30 meter for a pedestrian with a radar cross section of -8 dBsm. The performance will be considered at 13 dBm transmit power and an additional 3 dB loss will be added on to noise figure, taking into

Table 5.5: An overview of some system parameters in AWR2243.

Parameter	Value	Unit
Sampling rate	45	Msps
Noise figure	12	dB
No. transmitters	3	
No. receivers	4	
Max transmit Power	13	dBm
Maximum IF bandwidth	20	MHz
Maximum ramp rate	266	MHz/us
3 dB beamwidth elevation	± 10	degrees

account of other possible losses. Thus, given the radar range equation and thermal noise power in eq. (2.5.1) and eq. (2.5.3), as well as the the parameters in the tables 5.4 and 5.5, the corresponding SNR at 30 m is -37 dB at 300 K.

A standard signal processing flow consisting of pulse compression, Doppler processing and non-coherent channel integration before detection is considered. At the specified range resolution of 0.1 meters, a minimum of 300 samples are needed for a 30 meter coverage. Since the ADCs are capable of each outputting 734 samples over the 16.33 us chirp duration at a sampling rate of 45 Msps, we will assume that 512 samples are available at compression. Since processing gain for the range-Doppler processing is coherent, the gain will be approximately 45.7 dB, assuming a pessimistic 6 dB window and straddle loss. The channel integration is non-coherent and will result in an approximately 7.6 dB gain [3].

Thus, the SNR at 30 meter is 8.4 dB before integration and after 16 dB, before detection, which above the typical 10 dB threshold used in many detectors. If assuming Rayleigh distributed noise and a Swerling 0 target, then the probability of detection is evaluated as 99.9 % when using an optimal linear law detector with a probability of false alarm of 10^{-6} when using Albersheims equation [3]. Thus, the implementation is clearly feasible (and possible even over-designed for the use case).

5.2.3 Configuring a PMCW system

As a reference system, we will consider the 79 GHz system developed in [60,61]. A list of some system parameters is illustrated in table 5.6. The system employs two transmitters and two receivers, where it was demonstrated that two chips can be combined to form a four-by-four transmit-receive MIMO system. At transmit, the waveform generator is capable of generating any arbitrary binary sequence with up to 2047 chips at 1.975 Gb/s, with the additional possibility of employing outer code multiplexing by using Hadamard codes. At receive, the

Table 5.6: An overview of the system parameters of the PMCW in [60, 61]. [1]When using 1 or 2 chips.

Parameter	Value	Unit
Carrier frequency	79	GHz
Noise figure	10	dB
Maximum chip rate	1.975	Gbps
Maximum sequence length	2047	chips
Number of receivers	2 / 4[1]	
Number of transmitters	2 / 4[1]	
Maximum transmit power	10	dBm
3 dB beamwidth elevation	± 10	degrees

signal is downconverted to complex baseband and digitized using a synchronized 7 bit 1.975 GHz analog to digital converter. At each channel, a set of parallel correlation banks and accumulators are used for pulse compression and coherent integration. The compressed data is then sent off-chip for further Doppler processing, direction arrival estimation, detection and data processing.

In the following, the same signal processing chain as in [61] will be used to configure the system and assess the performance. For an overview, we refer to the paper and Sections 2 and 4 on the signal modeling and processing. In order to make a fair comparison, the system will be assessed based on TDM transmission, although it should be noted that this is not ideal for PMCW systems and that one would prefer outer CDM using Hadamard codes (which is supported in the considered system). Furthermore, to make this configuration comparable to the previous FMCW system, we will consider a two-chip cascade, employing all receivers but only employing three of the four transmitters.

Waveform: As previously, the minimum pulse repetition interval is 49 us, which yields an effective duration of maximum 16.33 us for each transmitter. Since the required bandwidth is 1500 MHz, the corresponding chip duration is 0.67 ns, which yields a pulse duration of approximately 1.36 us for 2047 chips. Accordingly, each transmitter can accumulate approximately 12 pulses to yield a duration of approximately 16.33 us. We note that the risk of range folding is small since the 1.36 us pulse length corresponds to an unambiguous range of 200 meters.

Sampling rates: It will be assumed that the analog to digital converters are perfectly synchronized with the waveform generation, as in [61], but at a lower sampling rate of 1500 MHz. This will allow the transmitted waveform to be perfectly recovered despite critically sampled.

SNR analysis: As previously, we will evaluate the SNR obtained at 30 meter for a pedestrian with a radar cross section of -8 dBsm. The performance will be considered at 10 dBm transmit power and an additional 3 dB loss will be added on to noise figure, taking into account of other possible losses. A 2 GHz analog bandwidth is assumed, yielding an SNR of approximately -58 dB before compression at 30 meter distance and a temperature of 300 K.

The pulse compression, accumulation and Doppler processing is assumed coherent and channel integration non-coherent, yielding a signal processing gain of 62.5 dB before channel integration and 70 dB after. We have removed 3 dB for window and straddle losses during the Doppler processing, and an additional possible 3 dB loss if using, for instance, GMSK modulation at transmit to satisfy regulations. The corresponding SNR at 30 meter is then approximately 12 dB after integration, which is also above the approximately 10 dB threshold used in many detectors. By using Albersheims equation with a probability of false alarm of 10^{-6}, the probability of detection is approximately 91%, which is reasonable considering the pessimistic assumptions.

5.2.4 System comparison

We will now proceed to compare the described systems. Since the biggest differences lies in the way pulse compression is carried out, the range and Doppler responses are specifically investigated in terms of sidelobe structure, resolution and dynamic range. We will consider some of the binary sequences proposed in [63, 69, 70] for automotive radar and only use conventional matched filter processing without any Doppler correction (except for MIMO motion compensation as descrbibed later on) or other processing techniques. ZCZ, APAS, MLS are considererd at 2048, 2000, 2047 symbols with the previous specifications. The ZCZ and APAS has sidelobe-free zones up to approximately 50 and 100 meters, respectively, which is sufficient for the considered scenarios. For the FMCW system, the Hann and Blackman windows are applied to the downconverted LFM signal. These windows are considered necessary in order to acheive adequate performance and are well representative for most conventional systems.

Effects of uncompensated Doppler shifts

Fig. 5.2 illustrates the differences in the range responses obtained after compressing some PMCW sequences and a Hann windowed LFM waveform at various target velocities. Note that the responses have been centered in range and normalized in power to make the differ-

ences more visible. In practice, small biases may occur in the FMCW due to, for instance, range-Doppler coupling along with certain processing losses caused by the windowing and dppler mismatch [3, 40]. The waveforms are generated at a 1500 MHz bandwidth except for one ZCZ sequence which is generated at 750 MHz as reference. It can be seen that all phase codes yield a sharp thumbtack response which is narrower than the Hann windowed waveform, indicating a slightly better contrast resolution of closely spaced and wide dynamic range targets. At zero Doppler, APAS and ZCZ yield zero sidelobes whereas MLS yields a flat sidelobe structure at just below -60 dB. The Hann window has a sidelobe structure with a peak at -32 dB and a fall off to -100 dB and well below at larger distances. With the utilized bandwidth of 1500 MHz, the expected range resolution is approximately 0.1 m. It can be seen that the phase coded waveforms acheive this, but that since windowing is used in the FMCW system (which is necessary), the resolution is in fact 0.2 m when measured from the mainlobe peak to the first null. For comparison, the same resolution is obtained at 750 MHz when using a ZCZ sequence. At increased Doppler shifts however, substantial sidelobe degradations occur for the phase modulated sequences which reduces the dynamic range. The LFM waveform on the other hand remain robust and experiences practically no performance loss over the increasing amount of Doppler shifts.

In order to further quantify the effects of the Doppler induced filter mistmatches, PSR, ISR and LPG is shown in Fig. 5.3 when evaluated at increasing shifts. Since the LFM waveform is well known to be Doppler resistant with a ridge-like ambiguity function, and is well documented in the literature, it is excluded from the figure. For this particular case, the Doppler mismatch SNR losses are assumed to be negligible. However, it should be noted that there are other losses present, corresponding to approximately 1.9 dB in the window and maximum 1.33 dB in the straddle when using a Hann taper [3]. From the figure, it can be seen that the LPG is neglible for all evaluated velocities, indicating that the SNR after compression remains relatively unaffected. On the other hand, the PSR and ISR increases at increasing Doppler shifts which in essence instead reduces the SCR at adjacent target cells, which reduces detectability. The effect is rather substantial in the considered case since it breaks the worst case dynamic range requirements of approximately 100 dB after only minor Doppler shifts. For instance, at a target velocity of 30 km/h, the PSR is only -70 dB for an APAS or ZCZ sequence while the Hann windowed LFM waveform has a PSR of well below -100 dB at longer ranges, indicating better sidelobe rejection It may be further noted from Fig. 5.3 that the PSR and ISR performance is best for ZCZ and APAS as compared to MLS, with ZCZ having an edge with respect to the ISR. Furthermore, the 750 MHz ZCZ performes worse than the 1500 MHz ZCZ which is due to the longer pulse length (each chip is twice as

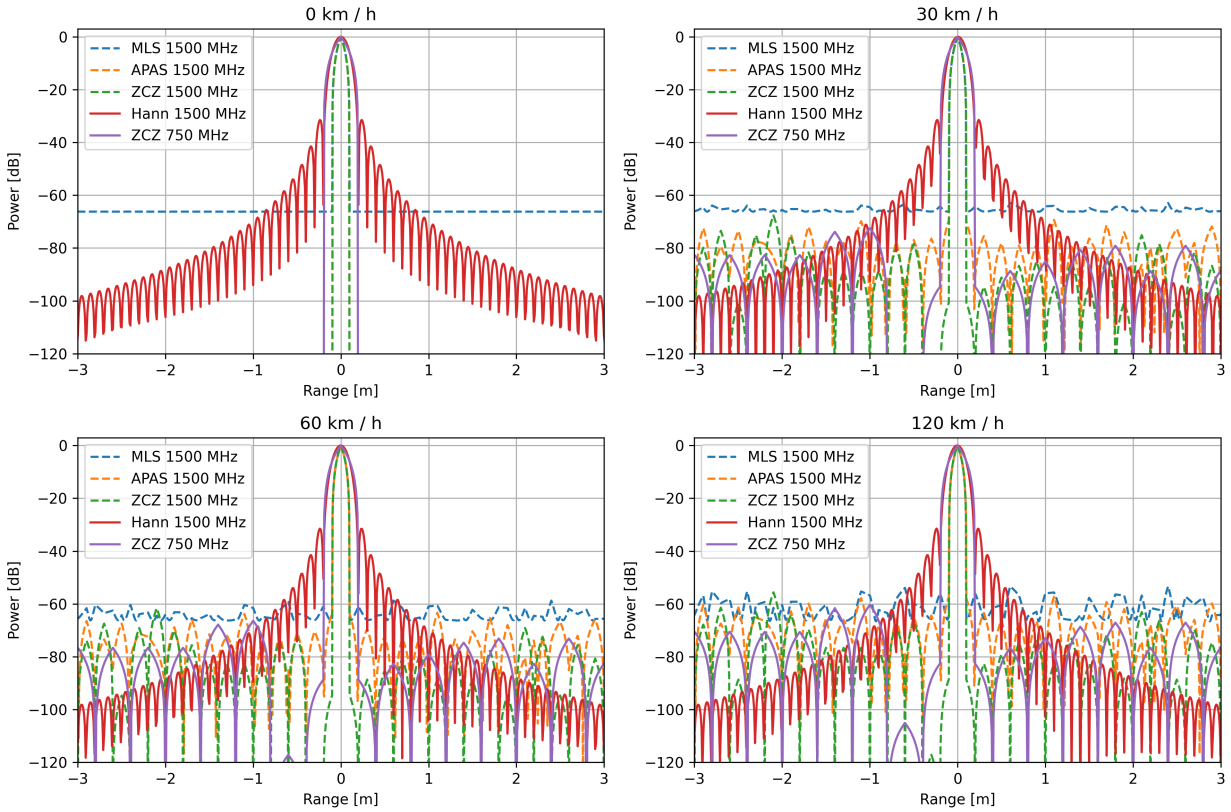

Figure 5.2: The normalized range response obtained after compressing various waveforms using matched filtering. It can be seen that the phase modulated waveforms (MLS, APAS, ZCZ) provide better resolution and dynamic range at small Doppler shifts and close distances when compared to the windowed periodogram (Hann). However, for large Doppler shifts and distances, the periodogram remains robust and outperforms the phase modulated analogs. Note that ZCZ acheives the same (Rayleigh) resolution as Hann at half the bandwidth.

long), which creates a larger Doppler distortion in the received signal. This appears to be a common phenomenon for most kind of sequences. As will be shown in the next example, the implications are that high RCS targets at close ranges may mask low RCS targets further away. However, for closely spaced targets, this is not an issue since the RCS differences typically do not exceed 50 dBsm in most scenarios.

Some performance illustrations

To give a further idea on how the systems differs, and illustrate the advantages of either kind of system, a test scenario consisting of two point sources with 40 and 10 dBsm cross sections will be considered. Although idealistic, these targets may represent a car and a bicyclist respectively and will illustrate the effects advantages and disadvantages of either system. Convential matched filtering will be used and it is assumed that the antennas form a uniform linear virtual array. In the setup, the previously presented APAS sequence will

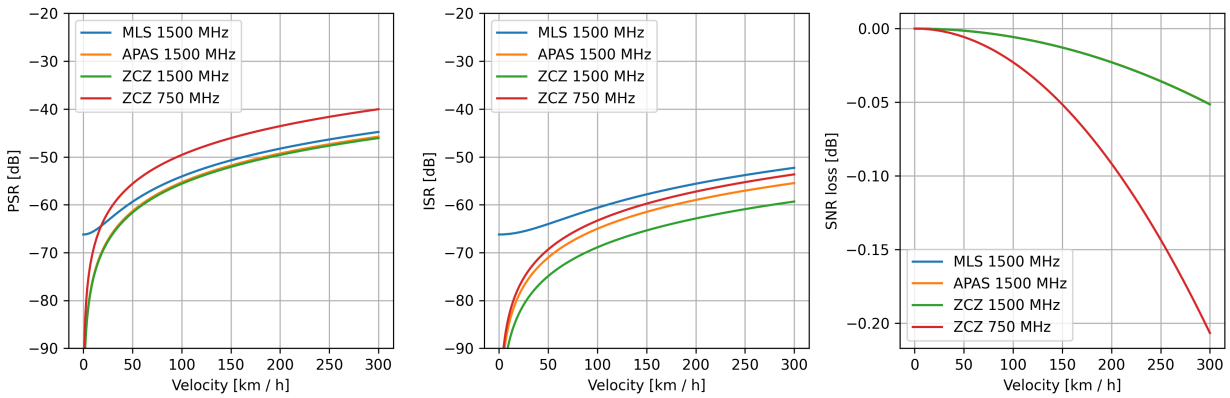

Figure 5.3: The figure illustrates the peak sidelobe ratio (PSR), integrated sidelobe ratio (ISR) and loss in processing gain (LPG) obtained after matched filtering compression for various Doppler shifts. It can be seen that small losses in processing

be used and compared with a hanning windowed LFM waveform after deramping. In the Doppler processing, a hanning window is used to taper the slow time samples.

Fig. 5.4 illustrates the range-Doppler maps obtained for the four different scenarios considered. The upper row corresponds to the response obtained from the PMCW system, and the bottom row the corresponding response from the FMCW system. In fig. 5.4a), the 40 and 10 dBsm target are placed at 2 and 7 meter range, respectively, with zero Doppler. It can be seen that the PMCW system manages to compress the target to a much smaller point source with no sidelobes in range when compared to the windowed FMCW, indicating a much better resolution and contrast imaging. However, as shown in fig. 5.4b), increasing the target velocities to 15 km/h increases the sidelobe levels dramatically in the PMCW system, making the weaker 10 dBsm target at 7 meter range hardly discernible from the surrounding clutter. The FMCW system on the other hand remains largely unaffected, illustrating the robustness in dynamic range even when the targets are subjected to Doppler shifts. Continuing, fig. 5.4c) illustrates the case when the targets are standing still at 2 and 2.5 meters respectively. It can be seen that, as previously, the PMCW system manages to compress the echos into two well separable point sources in the range-Doppler domain. On the other hand, despite having an expected resolution of 0.1 m, the targets are hard to discern due to the large main peak and high sidelobe levels. The same results can be seen in fig. 5.4d) when the targets are moving at a velocity of 15 km/h. It is noted that the targets are still discernible in the PMCW case despite the large sidelobe levels since the R^{-4} factor is not as prevalent when the targets are closely spaced. Similarly, the targets are still hardly resolvable in the FMCW case.

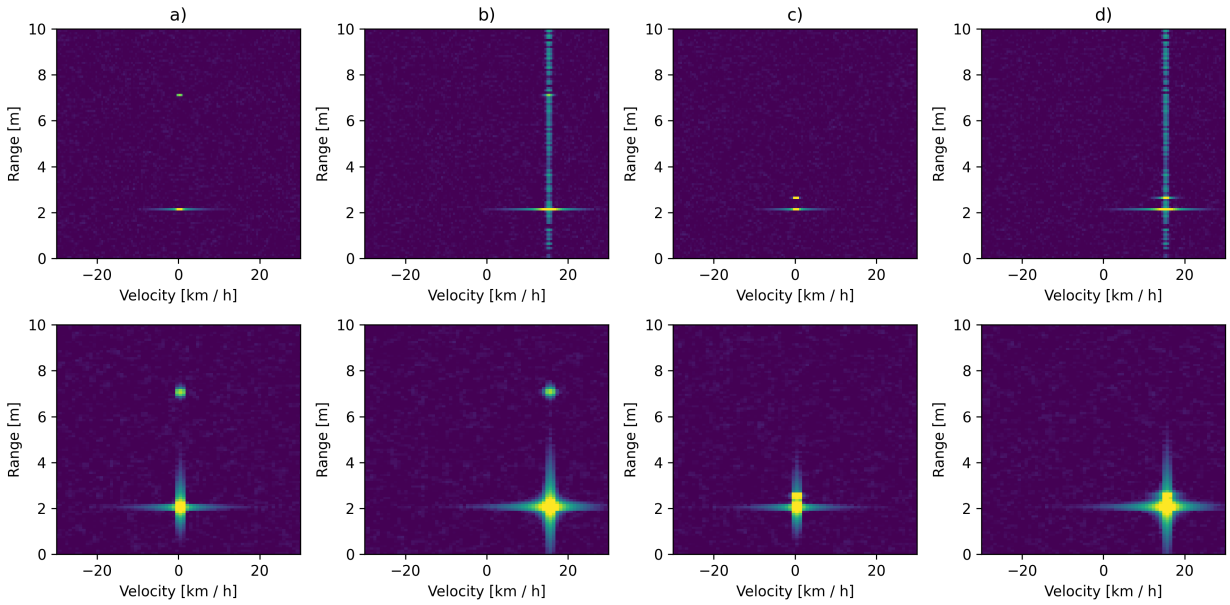

Figure 5.4: range-Doppler maps obtained. Upper row is PMCW, lower row is FMCW.

To further illustrate the effects of the increased sidelobe levels, fig. 5.5 shows eight range slices along the Doppler bin where the targets reside. As previously, the upper column corresponds to the PMCW and the lower by the FMCW, where we have also included a blackman window for reference. The scenarios in fig. 5.5a) and b) represent the cases when the targets are moving at 0 and 15 km/h respectively, each target located at 2 and 7 meter range. As previously, the FMCW system has no problems discerning the targets at either velocity, while the PMCW remains sensitive to the induced Doppler shift, raising the noise floor by almost 40 dB. To show the possible consequences of this mismatch, fig. 5.5c) and d) illustrates the same set of experiments, but the target at 7 m is moving to 14 m. At zero Doppler in c), the targets are well separable, but at 15 km/h the weaker target is no longer detectable as it lies below the sidelobe ridge.

This scenario is important since is idealizes many cases that may be encountered. For instance, one can imagine a bicyclist at boresight and a car crossing in a side lane, both driving at 15 km/h. In such case, both will end up in the same Doppler bin, and if the detector is only based on the range-Doppler map (which appears to be common), the bicyclist will not be detectable at a range of 14 m if the car is 2m from the sensor if one were to operate a PMCW system without any further processing.

Fig. 5.6 shows eight range slices illustrating the high contrast capabilities of either system. In a) and b), the targets are placed at 2 and 2.5 m respectively, with a) being stationary

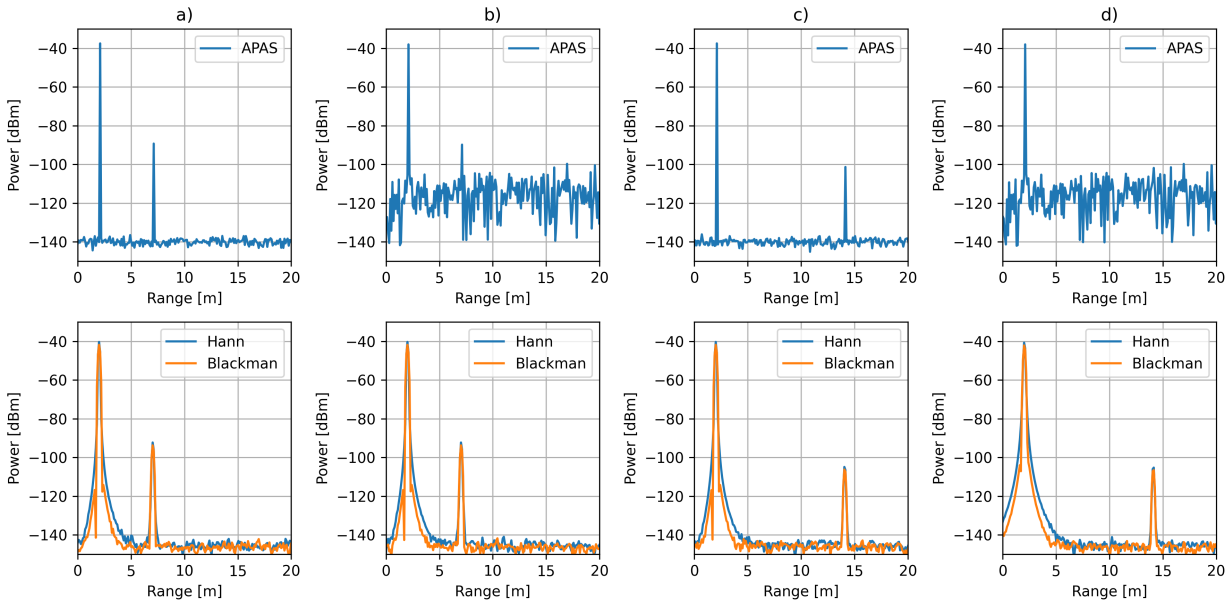

Figure 5.5: Range slices that the target Doppler bins. Upper row is PMCW, lower row is FMCW.

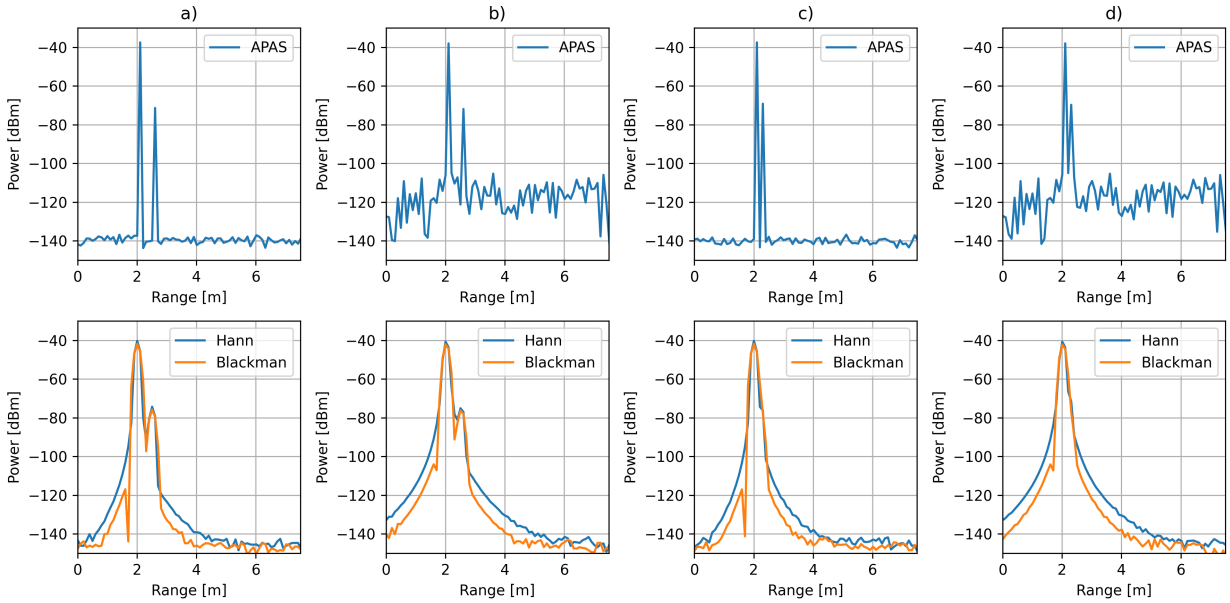

Figure 5.6: Range slices that the target Doppler bins. Upper row is PMCW, lower row is FMCW.

and b) both moving at 15 km/h. It can be seen that the range response of the PMCW system resembles as previously a thumbtack, with both targets clearly separated in the zero Doppler case. At 15 km/h, the sidelobes are as in the previous examples raised i significantly. However, the targets are still separable since the R^{-4} factor gets negligible at such short separation. For the Hann and Blackman windowed FMCW waveforms in the bottom, both targets are discernible for both tapers. However, they do not separate down to the noise floor, which in turn will require some sort of peak finding algorithm or data adaptive detector (for instance a sliding window CFAR variant [3]) in order to recover the sources. It should be noted that implementing a general detector for these kind of scenarios is not straightforward since the closely situated targets will act as persistent interferers and may cause a bias in the training data used in the detector. In practice this means that sometimes only little data is available to estimate the noise, clutter and interference statistics.Thus, discriminating the targets may, or may not be a challenge depending on the processing and kind of targets expected in the field of view. In fig. 5.6 c) and d), the same scenarios are illustrated, but with the targets at 2 and 2.2 m. As previously, both targets are separable in the PMCW systems, whereas in the FMCW, the peaks coalesce into one.

5.3 Extension to large MIMO systems

Sometimes, the separation in the range-Doppler domain is not sufficent for an ideal performance. Certain scenarios can be challenging and adding an extra spatial dimension might improve the performance considerably. Another benefit is that of reducing the cross range variations of the estimated target positions at longer ranges, as well as handling challenging environments where, for instance, resolution in elevation is important.

As discussed in the introduction of this thesis, systems with many tansmitters and receivers are being evaluated in the industry and may eventually make it to the consumer. Thus, in this section we will consider the recently developed SRR system in the angular domain, and investigate how the MIMO system affects the performance. The signal processing will still be based on the conventional matched filters, and in addition to the previously constructed range-Doppler maps, range-angle maps will be generated. These are generated by treating each received range profile as an independent snapshot, used to estimate the direction of arrivals at each range bin. However, some additional processing is needed since target motions will cause phase errors in the virtual array, which may degrade the performance. The process of mitigating this effect is known as motion compensation [138].

5.3.1 Motion compensation

We will now shortly show how to compensate for the motion by dragging back the phases in the Doppler domain. Let $\boldsymbol{y}_{tx,k} \in \mathbb{C}^{M\times 1}$ denote the signals received corresponding to the k:th active transmitter in the TDM. Under the simplified model in eq. (4.1.5), assuming N transmitters with $k = 0 \dots N-1$ and a single target with delay τ and Doppler shift f_d, the signal received under the time division multiplexing is

$$\begin{aligned}
\boldsymbol{y}_{tx,0} &= \alpha\phi(t_f-\tau)e^{-j2\pi f_d(t_s+0\cdot T_p)}\boldsymbol{b}a_0 = \boldsymbol{x}_0 a_0 e^{-j2\pi f_d 0\cdot T_p} \\
\boldsymbol{y}_{tx,1} &= \alpha\phi(t_f-\tau)e^{-j2\pi f_d(t_s+1\cdot T_p)}\boldsymbol{b}a_1 = \boldsymbol{x}_0 a_1 e^{-j2\pi f_d 1\cdot T_p} \\
\boldsymbol{y}_{tx,2} &= \alpha\phi(t_f-\tau)e^{-j2\pi f_d(t_s+2\cdot T_p)}\boldsymbol{b}a_2 = \boldsymbol{x}_0 a_2 e^{-j2\pi f_d 2\cdot T_p} \\
&\vdots
\end{aligned}$$

where $\boldsymbol{b}$ is the receive steering vector and a_k the k:th component of the transmit steering vector. Thus, as can be seen, the motion in the receivers corresponding to the k:th transmitters can be compensated by adding a $f_d T_p \cdot k$ phase shift. However, since the objective is to estimate the target parameters, the Doppler shift is not known. This issue can be circumvented by transforming the range-compressed data to the Doppler domain, apply the modulation specifically for each Doppler bin and then transforming back to the range-pulse domain where the direction of arrivals are estimated. This can be done without knowing the actual waveform parameters as follows. For the FMCW case, the normalized dopler frequencies (which are in the range -0.5 to 0.5) are given by $\nu = f_d N T_p$. Thus, the motion compensation can be expressed in terms of the considered Doppler bin as $f_d T_p k = f_d N T_p \frac{T_p k}{N T_p} = \nu k/N$ for the k:th transmitter. In the PMCW case, if the transmitters are switched between each accumulation, one also needs to know the number of accumulations N_{acc}, since then the normalized frequency is $\nu = f_d N N_{acc} T_p$. The corresponding phase shift is then $\nu k/(N N_{acc})$. It may be noted that the phase error is much smaller in the PMCW case than for the FMCW when a large number of accumulations is used. However, this assumes that the hardware is able to switch the power amplifiers at that rate. It appears more common to run all transmitters simulatensouly and run either inner or outer codes to acheive transmit orthogonality, such as Hadamard CDM, which also has the avantage of increasing the average transmit power given that the regulatory aspects are satisfied. Nevertheless, for the case of this particular comparison, we will disregard this aspect. We finally note that prior to angle estimation, one may perform additional Doppler processing, such as moving target indication to reduce the amount of clutter present.

5.3.2 Range-angle estimation in 3x4 MIMO

We will now illustrate the performance in the range-angle domain using the same systems as previously discussed.

In the first scenario, two targets with a cross section of 40 and 10 dBsm, each located at 2 and 8 m. The direction of arrivals are 30 and 0 degrees, respectively. Figure 5.7 illustrates the range angle maps for the respective PMCW (upper row) and FMCW systems (bottom row) when using a Hann windowed beamformer. As can be seen in a), and disregarding the aspects of range-resolution, both systems perform almost identically in the angular domain when the targets are stationary. Similar results can be seen in b), with also the range sidelobes appearing in the PMCW system.

To further investigate the performance, Figure 5.8 illustrates the angular-profiles obtained along the 7 meter range-bin for two targets moving at 15 km/h, separated by a) 30 degrees and b) 15 degrees. The target at boresight has a cross section of 0 dBsm, while the target at 30 degrees is increased from 0 dBsm to 40 dBsm. As can be seen in a), the targets are separable at 30 degrees, but with a bias of the weaker target which increases the higher the dynamic range is. In b), the targets are barely separable at equal dynamic range, with the resolvability lost at increased dynamic range.

These examples indicate that the performance in the angular domain is similar for both type of systems, and that the resolution is rather poor with very high sidelobes even if windowing is used. This is one of the reasons for the emerging use of large receive arrays, where MIMO plays a central role in keeping the cost and form factor favourable.

5.3.3 Range-angle estimation in 8x8 MIMO

In the following, we will evaluate the DOA estimation performance when using a 8x8 MIMO array. In order to satisfy the maximum unambiguous Doppler requirement, the systems are reconfigured as follows; instead of 12 accumulations, the PMCW will do 4 accumulations; the sweep time is reduced from 16.33 us to 6.1 us in the FMCW system. We will as previously consider two targets, both situated at 7 meters to evaluate the resolution. As previously, all range-angle maps are in dB-scale and represented in a linear color scale from the noise floor to the maximum peak. Furthermore, the upper rows in the figures correspond to the results from the PMCW systems and the lower from the FMCW systems.

Figure 5.9 illustrates the range-angle maps obtained when using the 8x8 MIMO system

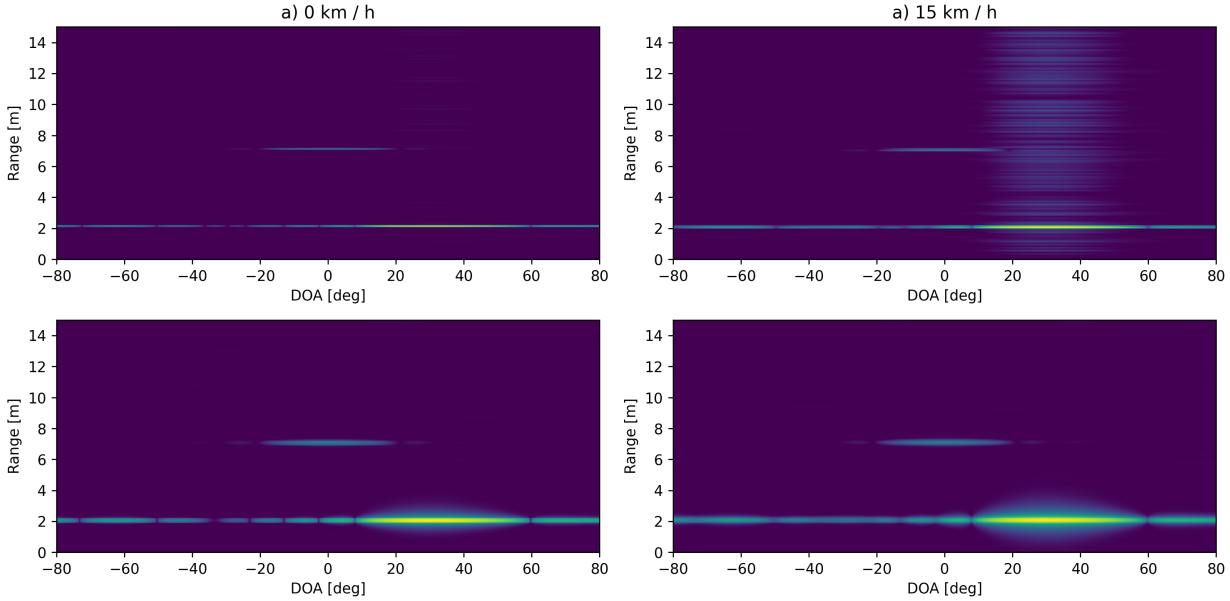

Figure 5.7: The figure illustrates the range-angle image for the respective 3x4 MIMO systems. Two targets are present, each with an RCS of 40 (at 2 m) and 10 (at 7 m) dBsm respetively.

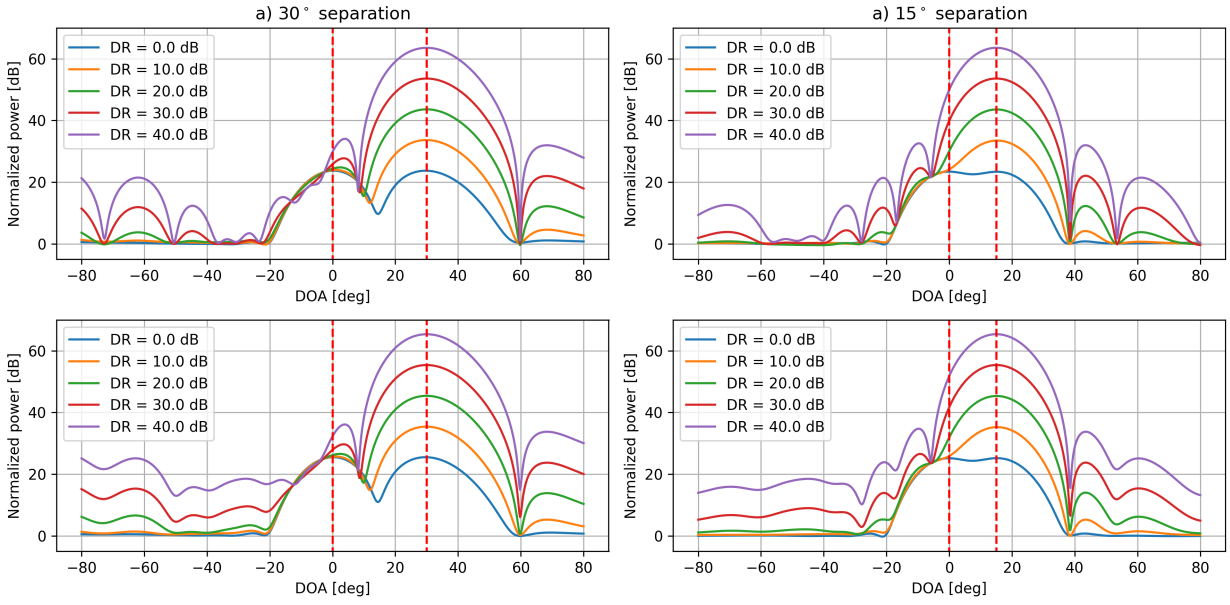

Figure 5.8: The figure illustrates four angular profiles as obtained from the respective 3x4 MIMO systems. The targets are moving at 15 km/h. DR = Dynamic Range.

without any motion compensation. As can be seen in the zero Doppler case in a), there are no issues localizing the targets. When the targets are moving at 15 km/h, however, in addition to the range clutter in the PMCW system, large sidelobes are apparent around the strong target at 15°, as shown in b). In the PMCW case, the target at boresight is still well discriminated, whereas the corresponding target in the FMCW case is masked. As previously discussed, this is because the PMCW system have much shorter pulses than the FMCW which in turn makes the phase errors in the virtual array smaller. Figure 5.10 illustrates the corresponding images after motion compensation. As can be seen, the sidelobes are significantly attenuated and the smaller target at boresight can now be discriminated from the sidelobes.

Figures 5.11 and 5.12 illustrate the angular profiles along the target range bin for both the Doppler uncompensated and compensated case. As can be seen in the uncompensated case, the spurioses caused by the motion induced errors apparent for both systems, but about 20 dB weaker in the PMCW system. The dynamic range in the respective systems is approximately 60 and 40 dB respectively, indicating also a 20 dB favor for the PMCW system. On the other hand, after motion compensation, practically all spurioses are eliminated while there still remain minor peaks in the FMCW system, at a dynamic range of approximately 60 dB, which is enough for practically all scenarios. It is worth nothing that large sidelobes are still present around the strongest target. This is due to the Hann window used during beamforming and indicates one of the major weaknesses of non-adaptive estimators.

The results indicate that PMCW systems have some inherent robustness to motion induced phase errors in the MIMO array when compared with FMCW systems, which is due to the relatively short pulses transmitted.

5.3.4 On MIMO scalability

We will now investigate how adding additional transmitters affects the system design. It was noted in table 5.4 that the minimum PRI needed to satisfy a 70 km/h maximum unambiguous velocity is 49 us. For three transmitters in a TDM or Hadamard CDM mode, this corresponds to a PRI of 16.33 us, and if using 8 or 16 transmitters, the maximum PRIs instead become 6.13 and 3.06 us.

For the considered PMCW system, this poses no bigger challenge than reducing the number of accumulations to 4 and 2, respectively, which in practice is no compromise. On the other hand, for the FMCW system, we first note that 16 transmitters is not supported

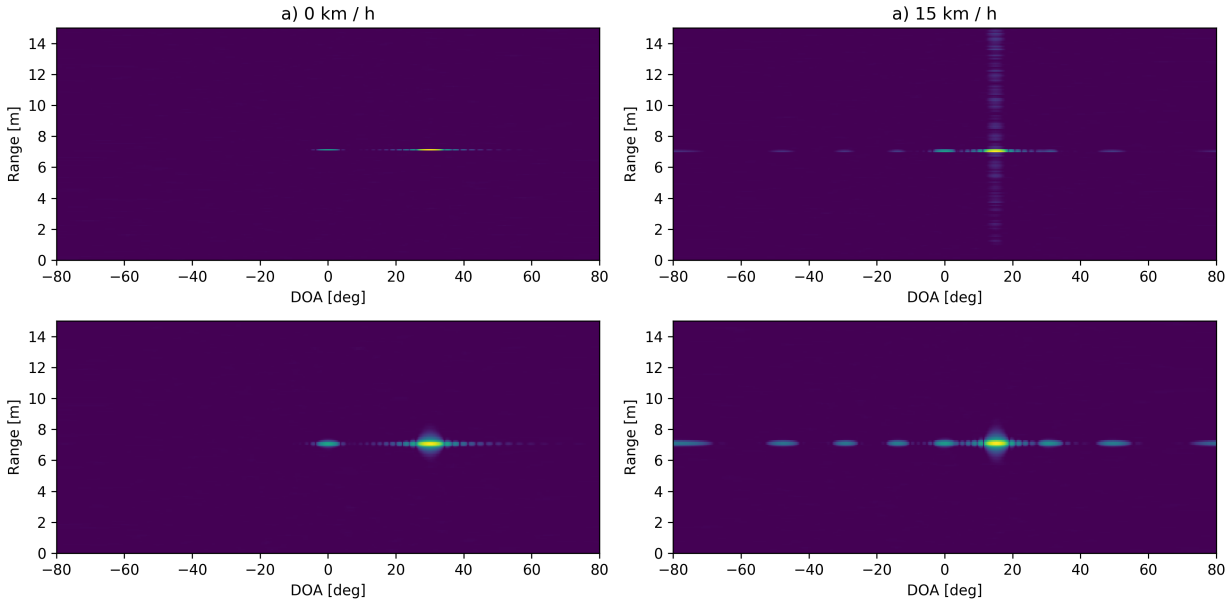

Figure 5.9: The figure illustrates the range-angle image of two targets with cross section 10 and 40 dBsm using the 8x8 MIMO system without motion compensation. The upper row is PMCW, the lower row is FMCW.

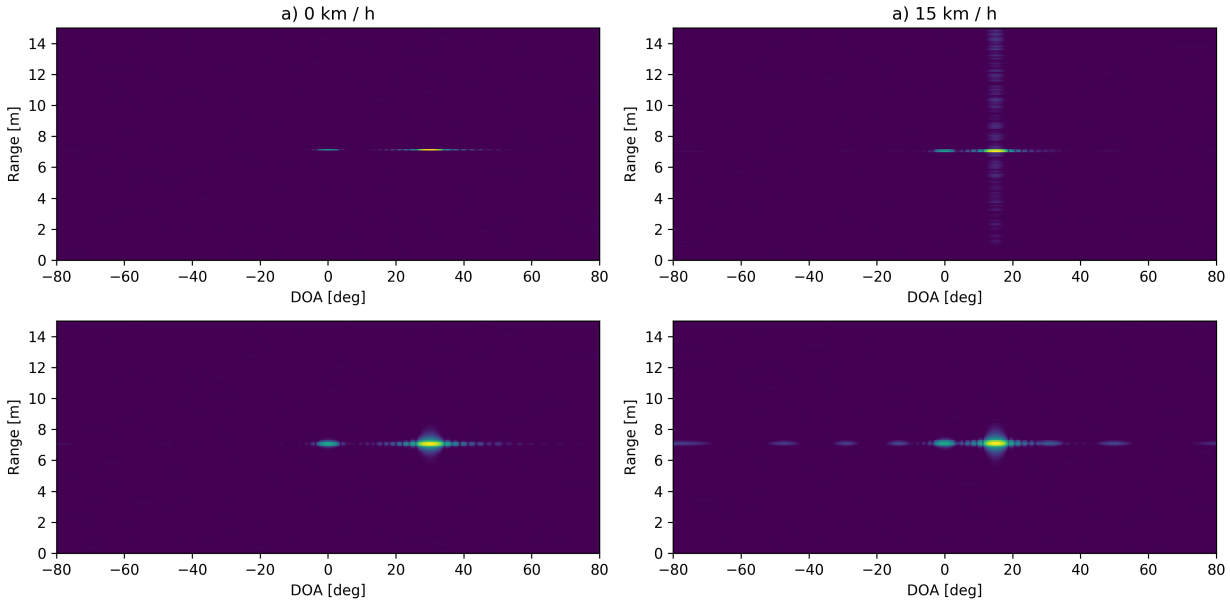

Figure 5.10: The figure illustrates the range-angle image of two targets with cross section 10 and 40 dBsm using the 8x8 MIMO system with motion compensation. The upper row is PMCW, the lower row is FMCW.

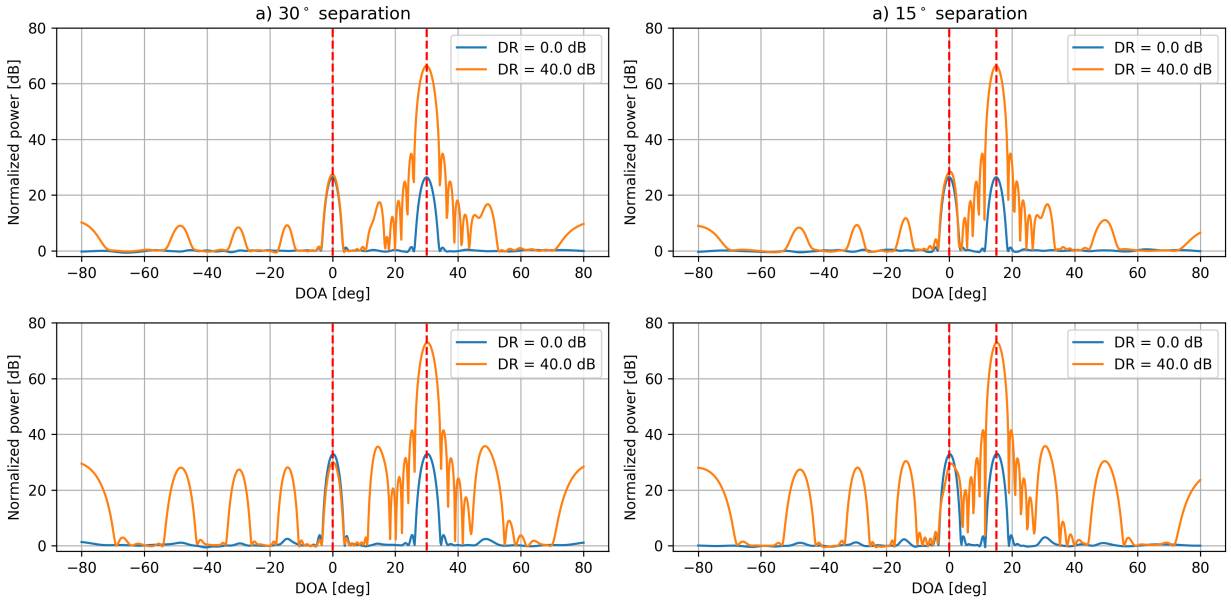

Figure 5.11: The figure illustrates the angular profile at the target range bin from Figure 5.9. The upper row is PMCW, the lower row is FMCW. DR =dynamic range.

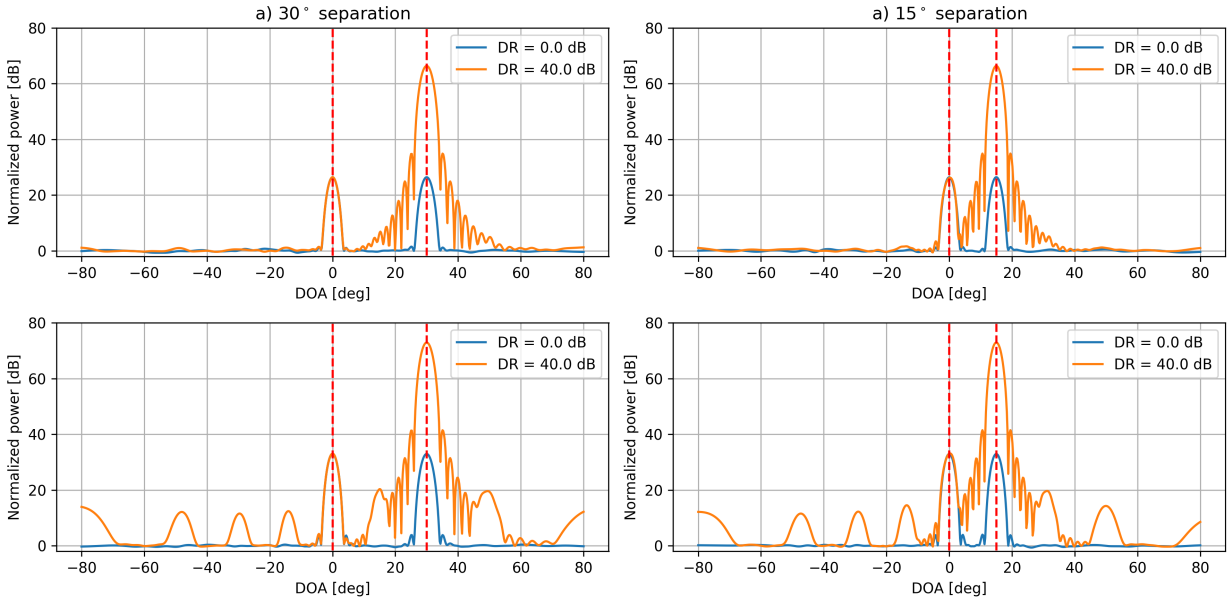

Figure 5.12: The figure illustrates the angular profile at the target range bin from Figure 5.10. The upper row is PMCW, the lower row is FMCW. DR = dynamic range.

by the hardware since this would correspond to a chirp rate of 489 MHz/us, as indicated by table 5.5. Another issue is the required sampling rate needed to cover the 30 m range swath. At 30 m, the beat frequencies for both both cases are 24.5 and 49 MHz. Thus, sampling rates of at least 49 and 98 Msps are needed to prevent aliasing for the respective cases. Neither of these two configurations are supported by hardware, and unless improved, some sort of compromises must be made. For instance, in the example in Section 5.2, a multi-mode approach was used, where a short range, high resolution and ambigous Doppler (low PRF) mode was combined with a long range, low resolution and unambiguous Doppler mode (staggered high PRF). Thus, by switching the modes over two consecutive frames and combining the target lists, the specification may still be fulfilled, at the cost of compromised resolution at longer ranges and twice the dwell time.

The observations indicate that current PMCW systems are more scalable from a MIMO point of view than current FMCW systems, with the issue appearing to originate in the transmit multiplexing and the low sampling rates used. To the best of the writer's knowledge, all current FMCW systems use either TDM or Hadamard CDM to multiplex the transmitters, each reducing the maximum unambiguous Doppler and increasing the required sampling rates by the number of transmitters. This in turn implies that much faster ADCs will be needed in order to keep up with the range-Doppler requirements. Furthermore, at the considered bandwidths, the pulse durations are in the order of few microseconds, and when operating over longer distances, the round-trip delay will be on the same order of magnitude (1 us corresponds to 150 m, for instance), indicating that a significantly large portion of the waveform needs to be discarded if using stretch processing.

The main issue appears to be the need to keep up with the reduced range-Doppler area when the transmitters increase. By multipltying eq. (4.5.2) and eq. (4.5.5) and letting $PRI = T_p/N_{tx}$, one obtains the largest achievable range-Doppler area

$$A_{pmcw} = \frac{\lambda c}{8N_{tx}} \tag{5.3.1}$$

which, as can be seen, does not depend on the choice of waveform, but only on the carrier frequency and number of transmitters. However, since the maximum range in FMCW systems is ADC limited, as indicated by eq. (4.5.3), the corresponding range-Doppler area is instead

$$A_{fmcw} = \frac{\lambda \Delta R F_{s,min}}{4N_{tx}} \tag{5.3.2}$$

which depends on the sampling rate $F_{s,min}$ and range resolution ΔR in addition to the number of transmitters. To make a comparison, consider an extremely capable system with the same SRR system parameters as previously considered, but with a maximum range of 250 meters, approaching that of some LIDAR systems. Then, the needed range-Doppler area is $250 \cdot 70/3.6 = 4861$ m^2/s. The corresponding achievable range-Doppler area in the PMCW case and the required sampling rates in the FMCW case are illustrated in table 5.7 for the case of $N_{tx} = 2, 4, 8, 16$ and 32 transmitters. As can be seen, the required range-Doppler area can be satisfied for all MIMO configurations when employing PMCW (neglecting the small undershoot at 32 transmitters). Turning to the required sampling rates in the FMCW system, it can immediately be seen that the sampling rates quickly approach those needed for direct IF sampling. This indicates that for such high performing systems, stretch processing becomes no longer feasible and the leap to enter the domain of entirely digital processors become smaller. Fundamentally, when pushing radar systems to these performance limits, there are very few corners that can be cut and PMCW systems appear to at least have a native support for managing the required waveforms.

As a final note on this issue, the maximum operational range was set to 250 meters, which indicates that in order to guarantee no range folding, one would need a maximum unambiguous range of, say 1000 meters, indicating the need for a four times larger range-Doppler area. However, this is only a problem when realizing the MIMO with TDM and Hadamard CDM, since then the pulse duration has to be reduced by the number of transmitters. If one instead uses orthogonal ZCZ sequences, such as the ones proposed in [100] (see also Section 3.1), then the range ambiguity is no longer an issue since the pulse duration is not compromised (although one then instead has to deal with Doppler effects). Note that this corresponds to setting $N_{tx} = 1$ in eq. (5.3.1), indicating initially that no compromises are made. However, by the Welch lower bound (see Section 3.3), it is impossible to design N_{tx} sequences with perfect auto- and cross corelation properties. On the other hand, the bound states that it is possible to construct sequences which are orthogonal over certain regions which size is reduced by a factor of N_{tx} from the single sequence case, which is exactly what the sequences in [100] manage. Thus, the *clear* range-Doppler area is still limited by eq. (5.3.1), but there is no risk of range folding. This observation appears to be consistent with the results in [56].

To conclude, as systems are progressing towards large MIMO systems the usable range-Doppler area becomes scarce. It appears therefore advantageous (and maybe necessary) to directly sample the entire IF bandwidth and then peform an entirely digital pulse compression, as in PMCW systems, as compared to the mixed analog-digital processing employed in

Table 5.7: The table illustrates the maximum possible range-Doppler area for a PMCW system, and the minimum sampling rate for a FMCW system to satisfy a range-Doppler area of 4861 m^2/s.

N_{tx}	A_{pmcw} [m^2/s]	$F_{s,min}$ [Msps]
2	71104	102
4	35552	205
8	17776	410
16	8888	820
32	4444	1640

the current FMCW stretch processors.

5.4 Conclusion

The focus on this section has been on automotive radar system design and a special attention has been made to make, to the best of the authors knowledge, a fair comparison between FMCW and PMCW type of systems. First, an overview of the design specifications was reviewed and discussed, also providing an example of an industrial design. Then, two short range radar systems for parking assistance were designed, one for each type of system. It was shown that both systems fulfill the specifications, with margins, and show feasible performance. The FMCW type of system was shown to be robust to Doppler-induced pulse compression mismatch, but showed poor resolution and contrasting capabilities when compared to the PMCW system. The PMCW system on the other hand showed good resolution with a thumbtack-like range response and excellent dynamic range, whenever the targets were stationary. As soon as fair amounts of Doppler was present, significant degradations were observed. In addition to the range-Doppler performance, the angular capabilities were also examined. It was shown that with the use of 12 virtual receivers, the performance was poor for both type of systems. Extending to larger MIMO arrays, PMCW showed better performance in the angular domain due to the fast pulses employed, making it more robust to Doppler-induced angular degradations than FMCW, which have relatively long pulses. It was further shown that from a native stand-point, PMCW systems show much better scaling capabilities than FMCW systems due to the inherent full baseband sampling approach, which allows for a full utilization of the range-doppler area. The FMCW systems on the other hand appear to be bottlenecked by the slow analog-to-digital converters employed, which is a result of the stretch processors used. It is argued that in order to approach real LIDAR capabilities, full baseband sampling might be necessary.

Chapter 6

High performance processing

6.1 Data adaptive DOA estimation

Since imaging radar systems using large MIMO arrays are emerging, we will in this section investigate the possible performance gains in the angular domain. Specifically, we will consider the cases of closely situated point sources and spatially extended targets. The purpose is to show the achievable performance under an idealistic setting to investigate whether certain difficult scenarios can be handled feasibly. Various hardware and environmental limiting factors are therefore neglected. Since data adaptive estimators are known to break to the resolution criteria in eq. (4.5.10), with some also providing more robust estimates than the conventional matched filters, five different estimators will be demonstrated.

6.1.1 Overview of the DOA signal model

We will quickly reiterate the idealized signal model in eq. (4.4.4) for DOA estimation:

$$\boldsymbol{y}(t) = \sum_{k=1}^{K} \alpha_k(t)\boldsymbol{v}_k + \boldsymbol{n} = \boldsymbol{B}\boldsymbol{s}(t) + \boldsymbol{n}(t) \tag{6.1.1}$$

where K is the number of hypothesized targets, $\boldsymbol{y}(t) \in \mathbb{C}^{MN\times 1}$ the data vector, $\boldsymbol{n}(t) \in \mathbb{C}^{MN\times 1}$ the associated noise, $\boldsymbol{s}(t) \in \mathbb{C}^{K\times 1}$ the source signals, $\boldsymbol{v}_k \in \mathbb{C}^{MN\times 1}$ the MIMO steering vector

and $\boldsymbol{B} \in \mathbb{C}^{MN \times K}$ is the MIMO steering matrix, each given as

$$\boldsymbol{s} = [\alpha_1(t), \quad \alpha_2(t), \quad \dots \quad , \alpha_K(t)]^T \tag{6.1.2}$$

$$\boldsymbol{B} = [\boldsymbol{v}_1, \quad \boldsymbol{v}_2, \quad \dots \quad , \boldsymbol{v}_K]^T \tag{6.1.3}$$

The noise $\boldsymbol{n}(t)$ is modelled as a zero mean, temporally white and uncorrelated stochastic process. The source signals $\boldsymbol{s}(t)$ are modelled as being zero mean, mutually uncorrelated and uncorrelated with $\boldsymbol{n}(t)$. The associated covariance matrices are then given by

$$\mathbb{E}\{\boldsymbol{n}(t)\boldsymbol{n}^*(\tilde{t})\} = \operatorname{diag}([\sigma_1 \quad \sigma_2 \quad \dots \quad \sigma_M])\,\delta_{t,\tilde{t}} \tag{6.1.4}$$

$$\mathbb{E}\{\boldsymbol{s}(t)\boldsymbol{s}^*(\tilde{t})\} = \operatorname{diag}([p_1 \quad p_2 \quad \dots \quad p_K])\,\delta_{t,\tilde{t}} \tag{6.1.5}$$

$$\mathbb{E}\{\boldsymbol{n}(t)\boldsymbol{s}^*(\tilde{t})\} = \boldsymbol{0} \tag{6.1.6}$$

where $\delta_{t,\tilde{t}} = 0$ for all $t \neq \tilde{t}$ and $\delta_{t,\tilde{t}} = 1$ for all $t = \tilde{t}$. Under the stated assumptions, the covariance matrix of $\boldsymbol{y}(t)$ can be expressed as

$$\boldsymbol{R} = \mathbb{E}\{\boldsymbol{y}(t)\boldsymbol{y}^*(t)\} = \boldsymbol{A}^*\boldsymbol{P}\boldsymbol{A} \tag{6.1.7}$$

where

$$\boldsymbol{A}^* = [\boldsymbol{v}_1 \quad \dots \quad \boldsymbol{v}_K \quad \boldsymbol{e}_1 \quad \dots \quad \boldsymbol{e}_M] \tag{6.1.8}$$

$$= [\boldsymbol{v}_1 \quad \dots \quad \boldsymbol{v}_K \quad \boldsymbol{v}_{K+1} \quad \dots \quad \boldsymbol{v}_{K+M}] \tag{6.1.9}$$

with $\boldsymbol{e}_k$ denoting a column vector which is one at index k and zero everywhere else, and

$$\boldsymbol{P} = \operatorname{diag}([p_1 \quad \dots \quad p_K \quad \sigma_1 \quad \dots \quad \sigma_M]) \tag{6.1.10}$$

The covariance matrix model (6.1.7) has been considered thoroughly in the literature and serves as the basis for many spectral estimators, see e.g. [112]. In the following, we will let $\hat{\boldsymbol{R}}$ denote an estimate of the covariance matrix, which is typically estimated using a forward-backward and (sometimes) spatially smoothed approach [108] (whenever the array allows),

$$\hat{\boldsymbol{R}} = \frac{1}{ST}\sum_{t=1}^{T}\sum_{i=1}^{S}\boldsymbol{y}_i(t)\boldsymbol{y}_i(t)^* \tag{6.1.11}$$

where $\boldsymbol{y}_i(t)$ is each of the S generated snapshots, both forward-backward and the subarrays, from $\boldsymbol{y}(t)$ and total T the number of temporal snapshots. Note that if the covariance matrix

is spatially smoothed, then the the steering vectors $\boldsymbol{v}_k$ need to be adjusted accordingly.

6.1.2 Overview of some spectral estimators

We will consider five adaptive estimators, MUSIC [139], MVDR [140], RCB [141], IAA [142], and q-SPICE [143–146], which all have previously been demonstrated in the multisnapshot case of DOA estimation that is currently considered. For further details on the first three estimators, see for instance [108, 112, 132].

The method of MUltiple SIgnal Classification (MUSIC) and Minimum Variance Distortionless Response (MVDR) beamformer (also known as Capon) are well known and popular in the radar community and will therefore only be shortly described. MUSIC is based on a subspace fitting approach where the signal and noise subspaces are assumed to be orthogonal in the eigenspace of the data. The pseudo power spectrum is given by

$$\hat{p}_k = \frac{1}{\boldsymbol{v}_k^* \hat{\boldsymbol{U}}_n \hat{\boldsymbol{U}}_n^* \boldsymbol{v}_k}, \quad k = 1 \dots K \tag{6.1.12}$$

where $\hat{\boldsymbol{U}}_n$ is the estimated noise subspace as obtained from the n singular vectors corresponding to the n smallest singular values in the singular value decomposition of $\hat{R}$. Note that the number of targets n needs to be known a priori, which is known as the model order selection problem. MVDR is based on a minimum variance criteria where the power over the array is minimized under the distortionless condition, giving rise to the following data-adaptive estimate of the power spectrum

$$\hat{p}_k = \frac{1}{\boldsymbol{v}_k^* \hat{\boldsymbol{R}}^{-1} \boldsymbol{v}_k}, \quad k = 1 \dots K \tag{6.1.13}$$

Note that an inverse of the $\hat{\boldsymbol{R}}$ needs to be formed, which can be difficult when the number of data is scarce. This is however not an issue in the considered use case where each pulse is an independent snapshot, although for very large arrays this can be problematic. Under such circumstances one may, for instance, form rolling averages from frame to frame or employ some form of dimensionality or rank reduction scheme.

The Robust Capon Beamformer (RCB) is an extension of MVDR to the case when an uncertainty is imposed on the steering vectors. Assuming a spherical uncertainty in $\boldsymbol{v}_k$, the

formulation takes the following form

$$\min_{\tilde{\boldsymbol{v}}_k} \ \tilde{\boldsymbol{v}}_k \boldsymbol{R}^{-1} \tilde{\boldsymbol{v}}_k, \quad \text{s.t} \quad \|\tilde{\boldsymbol{v}}_k - \boldsymbol{v}_k\|_2^2 = \epsilon \tag{6.1.14}$$

where the new weights $\tilde{\boldsymbol{v}}_k$ are used to form the MVDR spectrum. The weights can be solved efficiently using the Lagrange multiplier, see e.g [112], where it is also pointed out that it is not dramatically more expensive than the MVDR. The strength of RCB is the robustness to model misspecifications which may arise in many real world scenarios. For instance, the receive and transmit arrays are more often than not corrupted by calibration errors and mutual couplings, and in the considered problem, phase errors originating from target motions results in certain modeling errors. The steering vector uncertainty imposed on the formulation gives some robustness to these kind of issues.

The iterative adaptive approach (IAA) is an iterative nonparametric estimator which have the following updating formula:

1. Initialize p_k for $k = 1 \dots K$ using the unwindowed beamformer.
2. Repeat until convergence:
   - Set $\boldsymbol{R} = \boldsymbol{B}\boldsymbol{P}\boldsymbol{B}^*$ where $\boldsymbol{P} = \text{diag}\{p_k\}, \quad k = 1 \dots K$
   - Set $\hat{s}_k(t) = \frac{\boldsymbol{v}_k^* \boldsymbol{R}^{-1} \boldsymbol{y}(t)}{\boldsymbol{v}_k^* \boldsymbol{R}^{-1} \boldsymbol{v}_k}, \quad t = 1 \dots T, \quad k = 1 \dots K$
   - $p_k = \frac{1}{T} \sum_{t=1}^{T} |\hat{s}_s(t)|^2, \quad k = 1 \dots K$

The method has been proven useful in applications such as MIMO and STAP radar systems [147–149].

The generalized Sparse Covariance Based Estimator (q-SPICE) is a hyperparameter-free semiparametric estimator recently proposed, which in the considered case minimizes is a linearly constrained whitening problem. The updating formulas are given as

1. Initialize p_k for $k = 1 \dots K$ using PER.
2. Initialize $\sigma_k = p_{K+k}$ for $k = 1 \dots MN$ using the MN smallest values of PER.
3. Set $w_k = \frac{1}{T} \boldsymbol{v}_k^* \hat{\boldsymbol{R}}^{-1} \boldsymbol{v}_k, \quad k = 1 \dots K$
4. Set $\nu_k = \frac{1}{T} \boldsymbol{e}_k^* \hat{\boldsymbol{R}}^{-1} \boldsymbol{e}_k, \quad k = 1 \dots MN$
5. Repeat until convergence:

- Set $\boldsymbol{R} = \boldsymbol{A}^* \boldsymbol{P} \boldsymbol{A}$ using eq. (6.1.7).
- Set $\beta_k = p_k \| \boldsymbol{v}_k^* \boldsymbol{R}^{-1} \hat{\boldsymbol{R}}^{1/2} \|_2, \quad k = 1 \dots K$
- Set $\gamma_l = \sigma_l \| \boldsymbol{e}_l^* \boldsymbol{R}^{-1} \hat{\boldsymbol{R}}^{1/2} \|_2, \quad l = 1 \dots MN$
- Set $\lambda = \sum_{k=1}^{K} w_k^{1/2} \beta_k + \left(\sum_{l=1}^{MN} \nu^{\frac{q}{q+1}} \gamma^{\frac{2q}{q+1}} \right)^{\frac{q+1}{2q}}$
- Set $p_k = \frac{\beta_k}{\lambda w_k^{1/2}}, \quad k = 1 \dots K$
- Set $\sigma_l = \frac{\gamma_l^{\frac{2}{q+1}}}{\lambda \nu_l^{\frac{q}{q+1}}} \left(\sum_{k=1}^{MN} \nu_k^{\frac{q}{q+1}} \gamma_k^{\frac{2q}{q+1}} \right)^{\frac{q-1}{2q}}, \quad l = 1 \dots MN$

where the choice of q should be chosen with respect to the sparsity desired – we will use $q = 1$ and $q = 1.25$. In the case of $q = 1$, the estimator coincides with the SPICE estimator. The estimators have been shown to be useful in several spectral analysis and array processing applications [150–157].

6.1.3 Simulation setup

In the following, we will consider the same FMCW systems as in Section 5.2 using a 3x4 and 8x8 MIMO in a half wavelength ULA configuration, since it was shown to be the most sensitive to Doppler. The simulations were carried out as follows: The received data cubes were first compressed and then motion-compensated as given in Section 5.3.1. A total number of 286 range-profiles were used as individual snapshots. Since not all power spectrums are meaningful - for instance, MUSIC yields a pseudo-spectrum and q-SPICE a heavily biased one, the normalized spectrum of each estimator is considered

For the respective estimators, a set of 1024 steering vectors uniformly covering the angles $(-80°, 80°)$ was used. All targets were generated coherent and placed off-grid. The covariance matrices were estimated using the sample covariance matrix using a four array forward-backward spatial smoothing to mitigate the effect of source coherency. Although unrealistic, MUSIC was given the correct model order. The spherical uncertainty was set as $\epsilon = 0.1$ for RCB. IAA was run for 20 iterations. The q-SPICE estimators were evaluated for $q = 1$ and $q = 1.25$ and run for 250 iterations in order to prevent overly sparse solutions.

6.1.4 Results and Discussion

We will now illustrate the performance of the respective estimators. In total, four scenarios will be considered. The true targets are highlighted by a red cross if point sources and a red dashed line if spatially extended.

Scenario 1

In the following scenario, we will consider car located in front at boresight with a pedestrian 0.5 m to the right in cross range. The radar and car are both assumed to move with a velocity of 30 km/h, indicating the relative velocities are zero and that the pedestrian is instead moving towards the radar at 30 km/h. Although the pedestrian can be separated in Doppler, we will illustrate the performance in angle at the current settings. It is assumed that the car is 8 m in front of the radar, having a width of 1.9 m and thus spanning the azimuth angles -6.17° to 7.12°. In total, 35 point sources are generated over the region and each point is assumed Rayleigh distributed with an expected cross section of 20 dBsm each. This is a reasonable model for the fluctuations in the cross section [3]. The pedestrian is assumed a point target with -8 dBsm cross section at 11.31 degrees, corresponding to approximately 0.5 m from the car in cross range.

Figure 6.1 illustrates the angular profile along the 8 m range obtained using a 3x4 MIMO. As can be seen, none of the estimators manage to resolve the pedestrians. Furthermore, MUSIC, MVDR, 1.00- and 1.25-SPICE split into three peaks while IAA gives a flat spectrum. Figure 6.2 shows the corresponding results when using an 8x8 MIMO, showing a significantly improved performance for all estimators. PER has high sidelobes (as expected), whereas Hann, Blackman, MVDR and RCB resolves the car but not the pedestrian. MUSIC, IAA, 1.00 and 1.25-SPICE resolves the car and the pedestrian, with 1.25 SPICE appearing to have slightly better separation, which is most likely due to the enforced sparsity.

Scenario 2

This scenario is made to represent the case when a car approaches a tunnel opening at 60 km/h, where the objective is to separate the roof from the ground (so that is possible to detect if something is standing at the entrace). The entrace is assumed 80 m away with the opening being 5 m high. The angle from the ground (assumed 0 degrees elevation) to the opening is then 3.58°. Somewhat arbitrary, there is a wall extending above the opening to span 5 degrees up from 3.58°, and the ground is assumed to span 5 degrees down from boresight. A total of 15 Rayleigh distributed point scatterers with an expected cross section of 20 dBsm each was generated for the ground and wall. The number of targets correspond to approximately 3 scatterers per degree, or approximately five scatterers per resolution cell

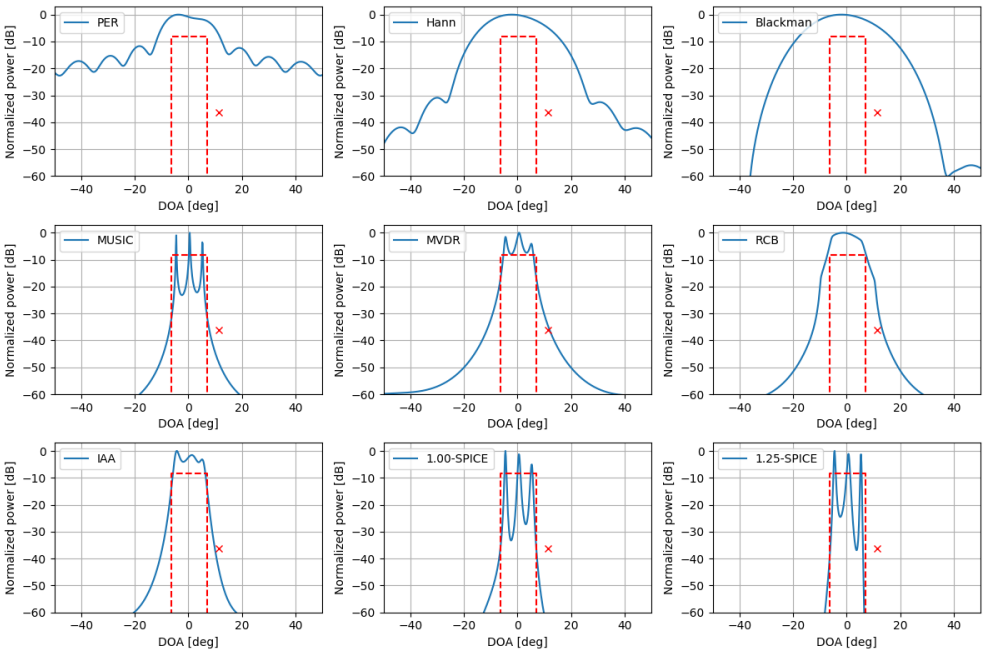

Figure 6.1: The angular profile for scenario 1 using a 3x4 MIMO. All sources are coherent and 286 snapshots (pulses) were used.

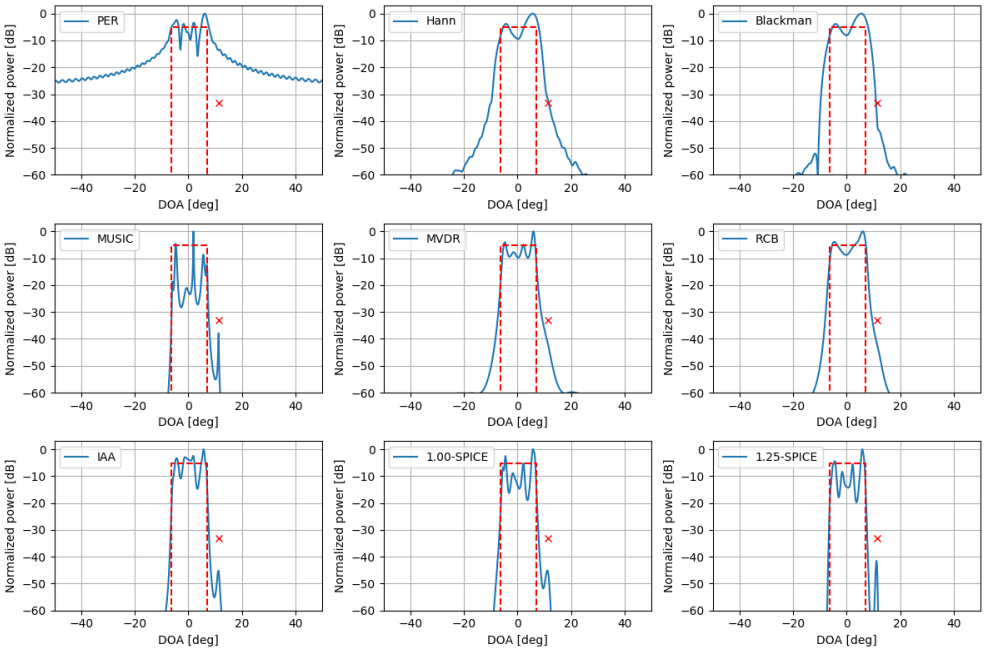

Figure 6.2: The angular profile for scenario 1 using an 8x8 MIMO. All point sources are coherent and 286 snapshots (pulses) were used.

for a 64 channels as given by eq. (4.5.10).

Figure 6.3 illustrates the angular profiles obtained for the 3x4 MIMO. It can be seen that PER, IAA and 1.00- and 1.25-SPICE provides best separation, with 1.50-SPICE appearing to provide the best separation, while the rest of the estimators do not manage to resolve the ridges. The corresponding profiles for the 8x8 MIMO are illustrated in Figure 6.4, with PER and IAA appearing to give the best separation. MUSIC gives separation but a lot of spurioses (it is given correct model order), and 1.00- and 1.25-SPICE, being sparse, have a very high ripple around the flat wideband regions, making the discrimination hard. The other estimators are simply not good enough for this scenario. Notably, the q-SPICE variants yielded much better performance when few elements was used in the 3x4 MIMO case. The reason for this is probably the sparsity assumption enforced and the relatively small dictionary used, since the effective number of targets is much smaller in the 3x4 MIMO than in the 8x8 MIMO, given the sizes of the resolution cells.

Scenario 3

This scenario is a mixed stationary scenario with multiple targets. The scene conssits of an extended target ranging between -20.17° to 7.12°, consisting of 74 scatters each with Rayleigh distributed with 1 dBsm expected value and three point targets at 30.40, 31.40 and 11.31 degrees with a cross section of 30, 30 and -8 dBsm respectively. It should be noted that the total number of sources exceeds the number of virtual receivers for all cases, indicating that the array is saturated and that the problem is somewhat badly posed.

Figure 6.5 illustrates the imaging results when using a 3x4 MIMO array. It can be seen that all periodogram based estimators fail while all adaptive estimators manage to resolve the plateu and one of the two closely spaced scatterers at 30.4° and 31.4°, but not the weak one at 11.37°. The nonparametric estimators, MVDR, IAA and RCB are very similar, while MUSIC, 1.00- and 1.25-SPICE, being sparse, have high ripples in the flat region. The corresponding case with an 8x8 MIMO in Figure 6.6 shows a significantly improved performance for all estimators. All manage to separate the extended target and at least one of the peaks at 30-31 degrees. However, only IAA and the q-SPICE estimators manage to resolve all targets.

A special case of spatial spread

We will consider a scenario with two point sources and one extended target with constant deterministic amplitude. The point sources are placed at 30.4° and 11.31° with a cross section of 40 and -8 dBsm respectively. The spread source consists of 84 uniformly placed point sources from $-32.51°$ to 7.12° (approximately 4 points per resolution cell in the 64

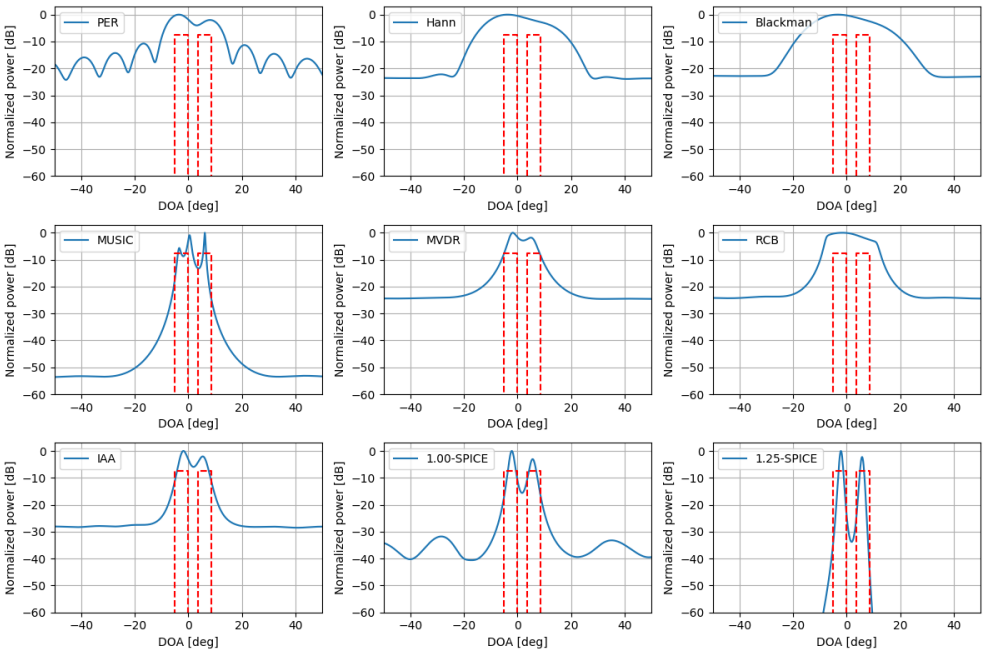

Figure 6.3: Angular profile along target range. 3x4 MIMO Coherent targets, 286 snapshots (pulses). 6 subarray forward-backward spatial smoothing.

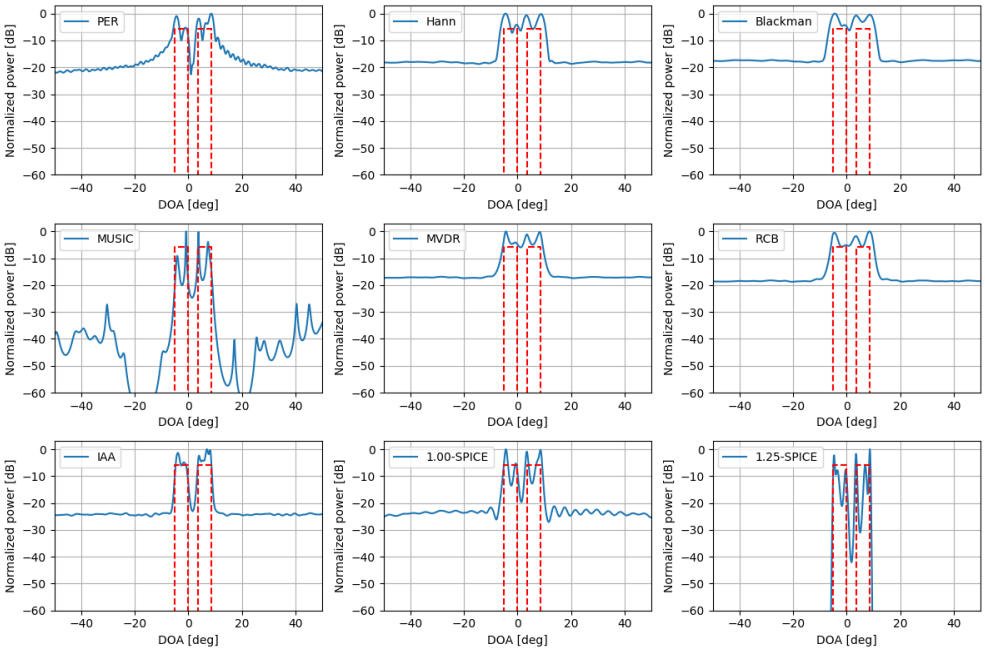

Figure 6.4: Angular profile along target range. 8x8 MIMO Coherent targets, 286 snapshots (pulses). 32 subarray forward-backward spatial smoothing.

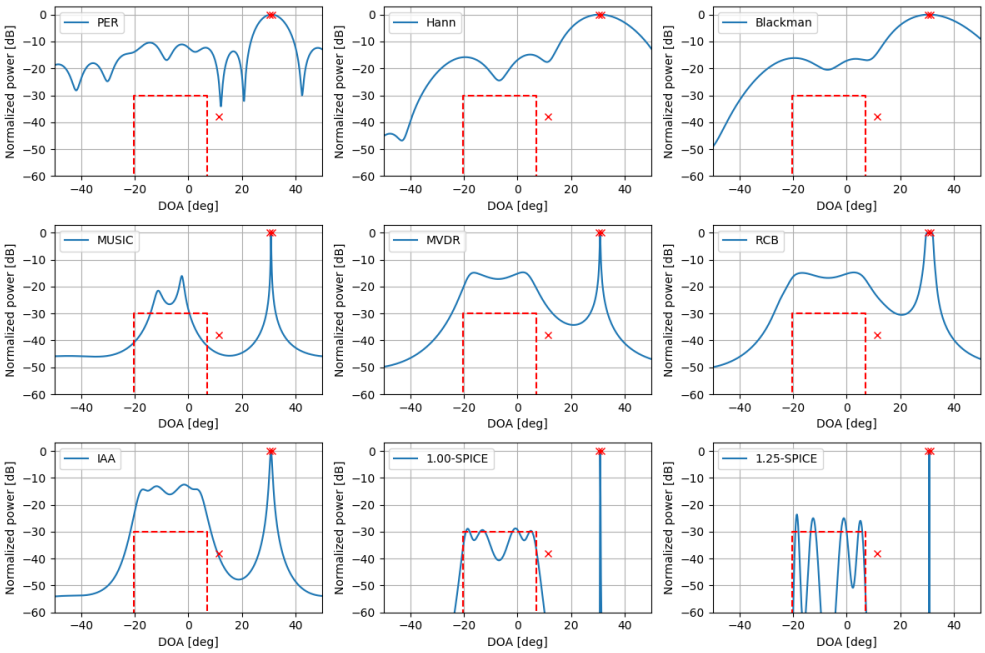

Figure 6.5: Angular profile along target range. 3x4 MIMO Coherent targets, 286 snapshots (pulses). 6 subarray forward-backward spatial smoothing.

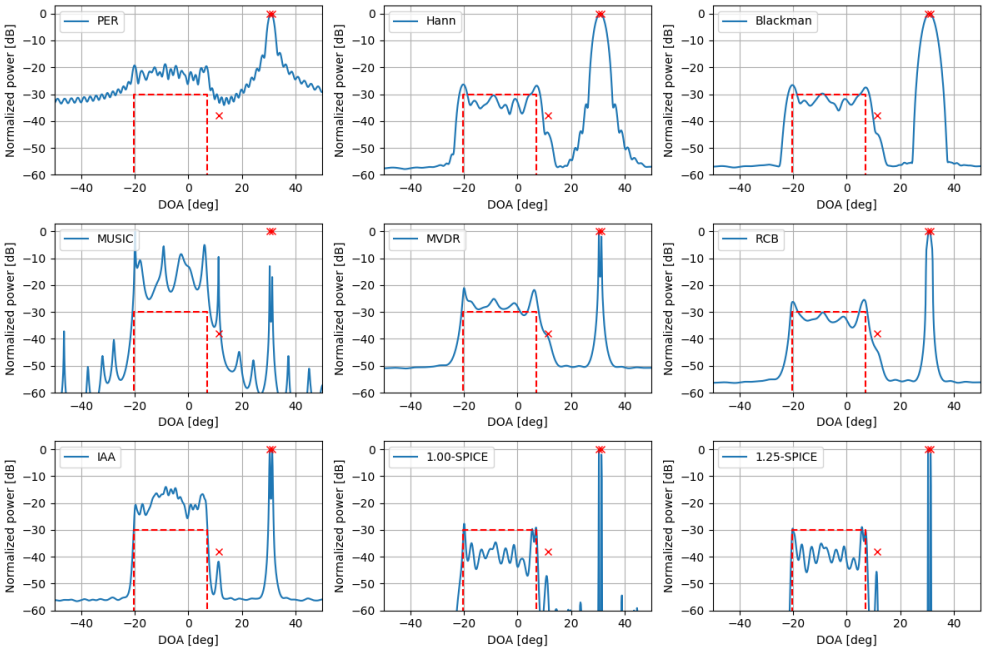

Figure 6.6: Angular profile along target range. 8x8 MIMO Coherent targets, 286 snapshots (pulses). 32 subarray forward-backward spatial smoothing.

element case) each with a cross section of 1.2 dBsm. The targets are stationary and located at 12 m range.

Figure 6.7 illustrates the scenario using an 8x8 MIMO array. As can be seen, increasing the array significantly improves the performace. Somewhat surprising, it can be seen that all of the estimators fails at representing the extended target (with MUSIC having a complete breakdown), except for IAA. Specifically, only the edges of the extended target can be located and the high multitarget scenario appear to negatively affect the resolvability of the closely situated 8 dBsm target at 11.31°. As a reference, we have included the equivalent case of four point targets, where most estimators manage to resolve the targets in Figure 6.8.

This phenomenon of target splitting is believed to be a consequence of the constant deterministic amplitude, explained as follows: Consider a target which is wideband and spread between the frequencies w_1 and w_2 and assume a continuous source distribution. Then, the k:th component of the "spatially extended steering vector" can be represented as

$$\int_{w_1}^{w_2} e^{jwk} dw = \frac{1}{jk}(e^{jw_2k} - e^{jw_1k}) \tag{6.1.15}$$

which consists two weighted point sources each located at the edges of the target. Note that the weighting does not affect the position of the sources, but will only cause a peak widening since its spectrally unimodal, narrowband around the zero frequency and independent of w_1 and w_2. Thus, if a continuous (wideband) target distribution is considered, then the *true* spectrum is *not* wideband, but in fact narrowband! However, if the target can instead be represented by a discrete set of K dominant narrowband sources, possibly unresolvable within each resolution cell, then the target representation is

$$\boldsymbol{y} = \sum_{k=0}^{K-1} \alpha \boldsymbol{v}(\theta + d\theta \cdot k) \tag{6.1.16}$$

where $d\theta$ is the source spacing. Under such circumstances, and assuming identifiability, one should expect the maximum-likelihood solution to be able to recover the amplitudes α at each of the targets, and thus the *true* spread target representation. With the results presented, it therefore appears that in this particular scenario, IAA is closer to the maximum-likelihood solution than the rest of the estimators which instead seem to converge to the continuous solution, indicating that IAA is a very special estimator.

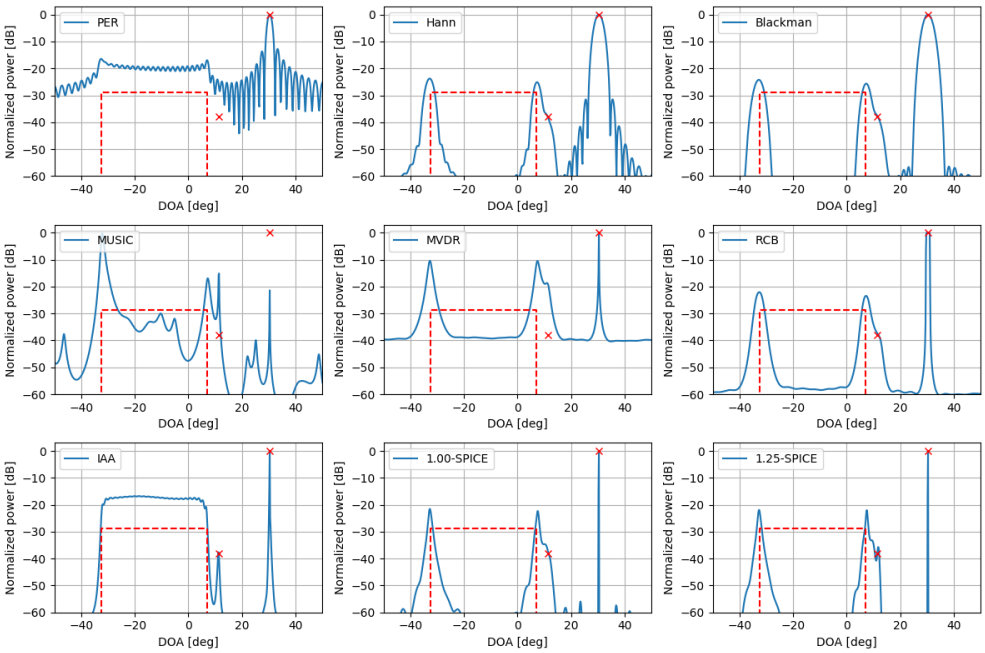

Figure 6.7: Angular profile along target range. Coherent targets, 286 snapshots (pulses). 4 subarray forward-backward spatial smoothing.

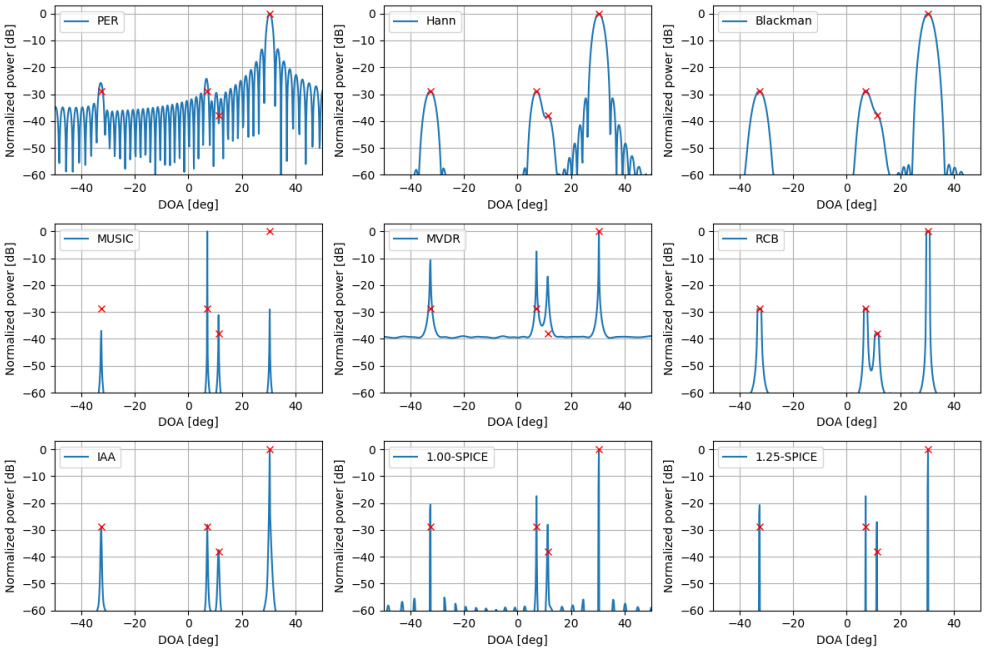

Figure 6.8: Angular profile along target range. Coherent targets, 286 snapshots (pulses). 4 subarray forward-backward spatial smoothing.

6.1.5 Conclusion

In this section, the use of MIMO for improving the angular resolution has been shortly investigated. It was shown that using multiple receivers and transmitters combined with data adaptive estimators significantly improves the performance in the angular domain.

In the considerer scenarios, IAA was shown to have best performance overall. Being non-parametric, it makes few assumptions on the data and does not need any complicated initializations or model order selection schemes. It was shown to handle extended targets well, even in the special case of equal amplitudes, while simultaneously showing a resolution comparable to that of MUSIC and better than MVDR. The amplitude estimates were furthermore good and the estimator was shown to handle large dynamic ranges with close targets without any significant degradations. On the downside, the estimator is *expensive* in the form presented and runs in $\mathcal{O}(M^3N^3)$ when using a direct implementation. It is worth noting that the method does not rely on any data covariance matrix estimates. However, this has been a topic of research and in [158] an exact $\mathcal{O}(M^2N^2)$ implementation was propsed by exploiting the toeplitz structure of the covariance matrix, using a combination of fast fourier transforms, Gohberg-Semencul factorizations and Levinson-Durbin recursions. In [159], the method was extended by using a preconditioned gradient descent approach, yielding an approximate solution running in tractable $\mathcal{O}(MN \log MN)$.

The sparse methods, MUSIC and q-SPICE were shown to be poorly suited (although better than the periodogram and MVDR based estimators) to the mixed nature of spread targets and point sources, yielding a large ripples at extended portions and sometimes spurioses (mostly MUSIC when given correct model order). The periodogram based estimators appeared insufficent for many of the use cases. Based on the results, IAA, being nonparametric, appears to have the best performance against spatially spread targets and appear to provide a good trade-off between resolution, accuracy and robustness.

However, we pin-point the fact that PER is in fact maximum-likelihood when there is only a single point source present and interference is absent, which is a good approximation for the majority of scenarios in automotive radar. Under such circumstances, the data adaptive approaches will not provide any performance benefits over PER. Nevertheless, if imaging capabilities are considered and corner cases are to be properly handled, then they might be of great value.

6.2 Pulse compression filter design

As was discussed in Section 5, good waveform correlation properties can be hard to obtain, specifically when uncompensated Doppler is present. However, since the compression was performed by matching with the same transmitted sequence — the natural question is therefore if one can obtain a better compression by matching with something else.

It is well known from detection theory that the matched filter maximizes the SNR under the white Gaussian noise assumption [3]. However, the matched filter is only optimal in the single target case and is not derived with the consideration of multitarget scenarios. Under such circumstances, out-of-phase matching may lead to high sidelobes with the consequence of masking weak returns. A remedy for this is the mismatched filter, which at the cost of certain performance losses matches the received signal as to mitigate these secondary effects. In FMCW systems, mismatched filters may be realized by using window functions, which reduces the sidelobes at the cost of some SNR and resolution losses. However, window functions are not applicable to PMCW systems, and an approach is to instead consider computational approaches.

In this section, the framework presented in [111] will be used to design mismatched filters for the periodic waveforms used in PMCW radar. It will be shown that sequences with poor correlation properties (for radar) can still be used if the matching filter are tailored at the receving end. Additionally, it is shown that the problem of uncompensated Doppler (as discussed in Section 5) can be mitigated by imposing Doppler constraints into the design problem, making the sequences presented also compatible with the dynamic range requirements for moving targets. However, when compared with the corresponding matched filters, a possible issue appears to be the large number of bits needed in order to achieve sufficient sidelobe attenuations.

6.2.1 Minimum PSLR filter design

We will consider the design of pulse compression filters for one transmit channel at a time. If multiple transmit channels are used, then one can design one filter separately for each channel. Under such conditions, the pulse-compression response for a single receiver in

eq. (4.2.1), evaluated at a certain range bin, can be written as

$$y = \alpha_0 \hat{\boldsymbol{\phi}}^* \boldsymbol{\phi} + \sum_{i=1}^{I} \alpha_i \hat{\boldsymbol{\phi}}^* \boldsymbol{\lambda}_i \tag{6.2.1}$$

where noise, and Doppler and receive phase factors have been neglected. Here, $\hat{\boldsymbol{\phi}} \in \mathbb{C}^{L\times 1}$ is the mismatched filter and $\boldsymbol{\phi} \in \mathbb{C}^{L\times 1}$ the waveform to match against. The terms $\{\boldsymbol{\lambda}_l \in \mathbb{C}^{L\times 1}\}_{i=1}^{I}$ are all the waveforms which the filter needs to suppress, which can for instance be out-of-phase shifts of $\boldsymbol{\phi}$ as well as shifted versions of other waveforms, such as those originating from other transmitters in the MIMO. The term α_0 is the amplitude at the evaluated range bin and α_i the sidelobe contribution from other waveforms. We will consider the case of periodic waveforms, although the representation used does not impose any such restrictions and one may easily consider other type of waveforms. To illustrate the considered scenario, the compression when only one transmitter is present, taking into account of all $L-1$ out-of-phase shifts, is

$$y = \alpha_0 \hat{\boldsymbol{\phi}}^* \boldsymbol{\phi} + \alpha_1 \hat{\boldsymbol{\phi}}^* \boldsymbol{\lambda}_1 + \ldots + \alpha_{L-1} \hat{\boldsymbol{\phi}}^* \boldsymbol{\lambda}_{L-1} \tag{6.2.2}$$

$$= \alpha_0 \hat{\boldsymbol{\phi}}^* \boldsymbol{\phi} + \alpha_1 \hat{\boldsymbol{\phi}}^* \begin{bmatrix} \phi_L \\ \phi_1 \\ \vdots \\ \phi_{L-1} \end{bmatrix} + \ldots + \alpha_{L-1} \hat{\boldsymbol{\phi}}^* \begin{bmatrix} \phi_2 \\ \phi_3 \\ \vdots \\ \phi_1 \end{bmatrix} \tag{6.2.3}$$

where $\boldsymbol{\phi} = [\phi_1 \quad \phi_2 \quad \ldots \quad \phi_L]^T$. If multiple transmitters are used, then the corresponding waveforms should added as well. If Doppler shifts are expected, one may also include a set of Doppler shifted components in the set $\{\boldsymbol{\lambda}_i\}$to make the filter more resistant.

Previously in Section 5.1, the dynamic range was defined by ratio between the largest (in-phase) peak and strongest sidelobe. The definition is intuitive since it sets a limit on how far below strongest scatterer one can detect target returns without the risk of false alarms (thresholding sidelobes). A natural criterion when designing $\hat{\boldsymbol{\phi}}$ is therefore to maximize the dynamic range, or equivalenty minimize the PSLR, as given in eq. (3.1.5). The idea of the method presented in [111] is to solve a relaxed formulation of the PSLR minimization

problem. Specifically, the following problem is solved

$$\min_{t,\hat{\boldsymbol{\phi}}} \; t \tag{6.2.4}$$

$$\text{s.t} \quad \boldsymbol{\phi}^*\hat{\boldsymbol{\phi}} = \boldsymbol{\phi}^*\boldsymbol{\phi} \tag{6.2.5}$$

$$\hat{\boldsymbol{\phi}}^*\hat{\boldsymbol{\phi}} \leq \alpha\boldsymbol{\phi}^*\boldsymbol{\phi} \tag{6.2.6}$$

$$\|\hat{\boldsymbol{\phi}}^*\boldsymbol{\lambda}_i\|_2^2 \leq t, \quad i = 1 \dots I \tag{6.2.7}$$

In the formulation, t is minimized such that the sidelobe constraint $\|\hat{\boldsymbol{\phi}}^*\boldsymbol{\lambda}_i\|_2^2 \leq t$ is minimized uniformly. The energy constraint $\boldsymbol{\phi}^*\hat{\boldsymbol{\phi}} = \boldsymbol{\phi}^*\boldsymbol{\phi}$ prevents the trivial solution $\hat{\boldsymbol{\phi}} = \mathbf{0}$ and the constraint $\hat{\boldsymbol{\phi}}^*\hat{\boldsymbol{\phi}} \leq \alpha\boldsymbol{\phi}^*\boldsymbol{\phi}$ limits the LPG and can be necessary when the SNR losses are too high. The parameter α is set such that $LPG \geq -10\log_{10}\alpha$.

As can be seen in the formulation, there is no constraint put on the set $\{\boldsymbol{\lambda}_i\}$ which gives certain design freedoms. For instance, if only certain portions of the range swath is of interest, then zero correlation zones can be introduced by only considering those out-of-phase components. The advantage of doing this is an improved PSLR performance since fewer constraints are imposed on the optimization criteria. Similarly, one may add more constraints. For instance, to improve the resistance to Doppler degradation, one may in addition add Doppler shifted versions of the waveforms considered. Furthermore, if multiple transmitters (e.g MIMO) are used, one may also add the waveform components from the other transmitters, possibly also Doppler shifted, to improve the channel isolation.

The considered problem is a quadratically constrained quadratic program and is therefore convex [160]. An optimal solution can therefore be guaranteed given convergence to a stationary point and there are many software packages which can be used to solve the program — we will use cvxpy [161]. It should be noted that in the considered use case, all calculations are performed offline and only once. Therefore the computational complexity is of no issue. However, if online adaptivity and cognition is required, then more efficient schemes are most likely needed (at least for long sequences).

6.2.2 Results and Discussion

As previously shown in Section 5, the main issue with the considered waveforms was not poor out-of-phase properties — perfect responses could be designed within the desired range swaths. Similarly, MIMO orthogonality can be achived using any of the discussed methods in Section 3.2, given certain performance losses. The main issue was the degradation in pulse

compression when the returns were subjected to Doppler shifts, which significantly raised the sidelobe levels. We will therefore demonstrate how this particular issue can be mitigated by adding a Doppler constraint to the constraints in eq. (6.2.7).

While unrealistic, we will use a 64 bit floating point arithmetic to demonstrate the compression since this sets a bound on the best achievable performance when using the filters. The effect of quantization in the filter coefficients is shortly investigated afterwards.

A visual example

Figure 6.9 illustrates the matched filter and two minimum PSLR-filters designed on a 63 MLS. The filter denoted as only PSLR was designed as to obtain a ZCZ over the first 30 range bins, while the second, denoted as Doppler-PSLR filter, was designed the same but also including the Doppler modulated out-of-phase components at a Doppler shift of 60 km/h. As can be seen, the filters differ quite significantly in appearence, with the standard PSLR-filter being very similar to the matched filter, while the Doppler-PSLR filter is unrecognized.

To demonstrate the range-responses, Figure 6.10 illustrates the same example, but using a 64 chip APAS instead. As can be seen by the matched filter, a perfect ZCZ is obtained at the zero Doppler case, whereas in the non-zero Doppler case (120 km/h at 1500 MHz bandwidth), the sidelobes appear already at -70 dB. The designed Doppler-PSLR filter on the other hand shows no performance degradations in Doppler. The drawback however: for this particular case the LPG is -6.24 dB, which is significant. In the next example, it will be shown that for longer sequences, the LPG appears to not be as severe.

A design demonstration

In the following, we will illustrate the minimum PSLR filters for the system considered in Section 5.2. Specifically, we will consider four sequences presented in Section 3.1: MLS, Gold codes, APAS and ZCZ sequences each consisting of 2047, 2047, 2040 and 2048 chips respectively. The filters are designed over a ZCZ of 300 range bins, corresponding to the 30 m maximum range requirement, and the Doppler-PSLR filter is designed as previously – by duplicating the constraints at a 60 km/h Doppler shift.

Figure 6.11 illustrates the pulse compression responses (over the ZCZs) for the respective waveforms and filters, with the matched filter used as reference. As can be seen, the minimum PSLR are at least as good as the matched filters for all cases in the zero Doppler case. It should be noted that the PSLR filter for APAS and ZCZ sequences coincide with the matched filter over the considered ZCZ. However, at increased Doppler shifts the performance of the matched and minimum PSLR filters significantly degrade. The Doppler-PSLR on the

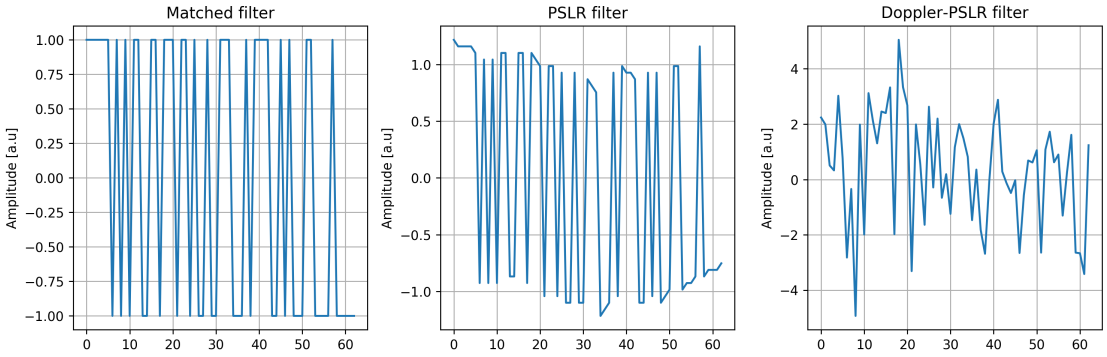

Figure 6.9: An example of a 63 chip MLS 30 bin ZCZ minimum-PSLR filter design. Comparison between matched and minimum-PSLR filters.

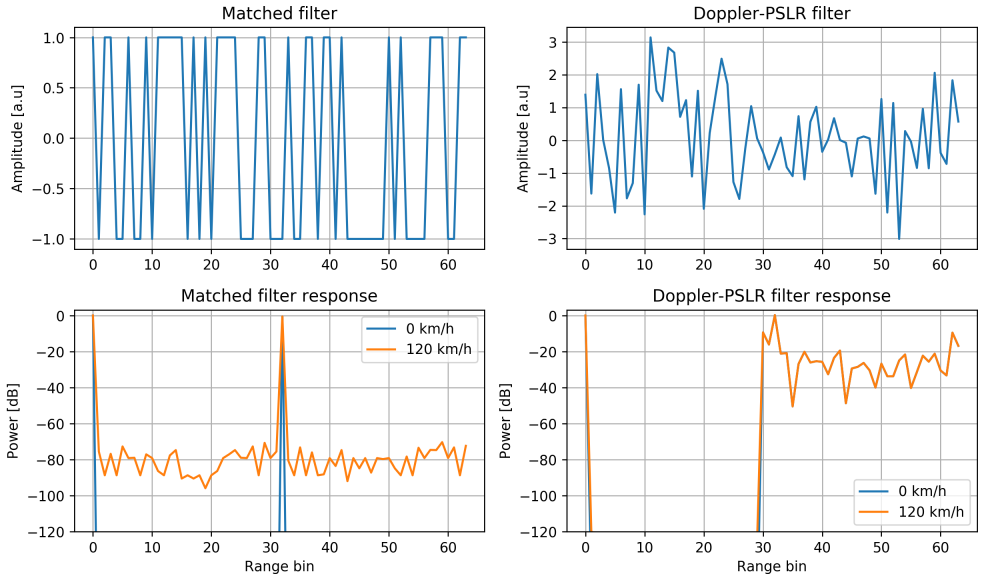

Figure 6.10: An example of a 64 chip APAS filter design. Comparison between matched and Doppler-designed minimum-PSLR filter. A ZCZ of 30 range bins was enforced on the PSLR filter.

other hand remains robust and has a PSLR of below 100 dB for velocities up to 250 km/h, indicating feasibility with respect to the system requirements. The corresponding LPGs are shown in Figure 6.12 and are in the range of a couple dB, comparable to the losses associated with most window functions [3].

To investigate the quantization effects on the minimum PSLR filters, the corresponding pulse compressions were performed (with full precision) after quantizing the filter cofficients. The results are shown in Figure 6.13 with the matched filter (which is only needs 1 bit) is shown for comparison. It can be seen that all of the minimum-PSLR filters are very sensitive to coefficient quantization. Specifically, approximately 24 bits are needed to obtain the same performance as in Figure 6.11, with 16 bits being sufficient if a dynamic range of 100 dB can be tolerated. Quantizing the filters down to 8 and 4 bits results in a performance which is worse than the original matched filter. Regarding the LPGs, those are practically identical to the ones in Figure 6.12 and are therefore omitted. This observation is important since compared to the matched filter, which only needs a 1 bit representation (and thus only additions at compression), the minimum-PSLR filters need at least a 16 bit representation along with multiplications in order to be realized. This may limit their use in real systems since the hardware must be scaled accordingly.

6.2.3 Conclusion

It was noted in Section 5.2 that for some waveforms used in PMCW systems, uncompensated Doppler may significantly degrade the performance to the extent of failing certain requirements. Consequently, the purpose of this section was to approach the problem at the pulse compression level by designing matching filters. The design problem was therefore reviewed and related to the pulse compression used in the PMCW systems. A set of minimum PSLR filters were then designed for the considered waveforms (and the popular Gold codes). The filters showed feasiblity when introducing further Doppler constraints and the LPGs were noted to be in the same level as for the conventional window functions used in FMCW. However, it was noted that a large number of bits is required in order to harness the effectiveness. For instance, 24 bits was required to obtain a similar performance as when using 64 bit floating points, and if 100 dB PSLR can be accepted (over Doppler shifts 0-250 km/h), then 16 bits appeared sufficient.

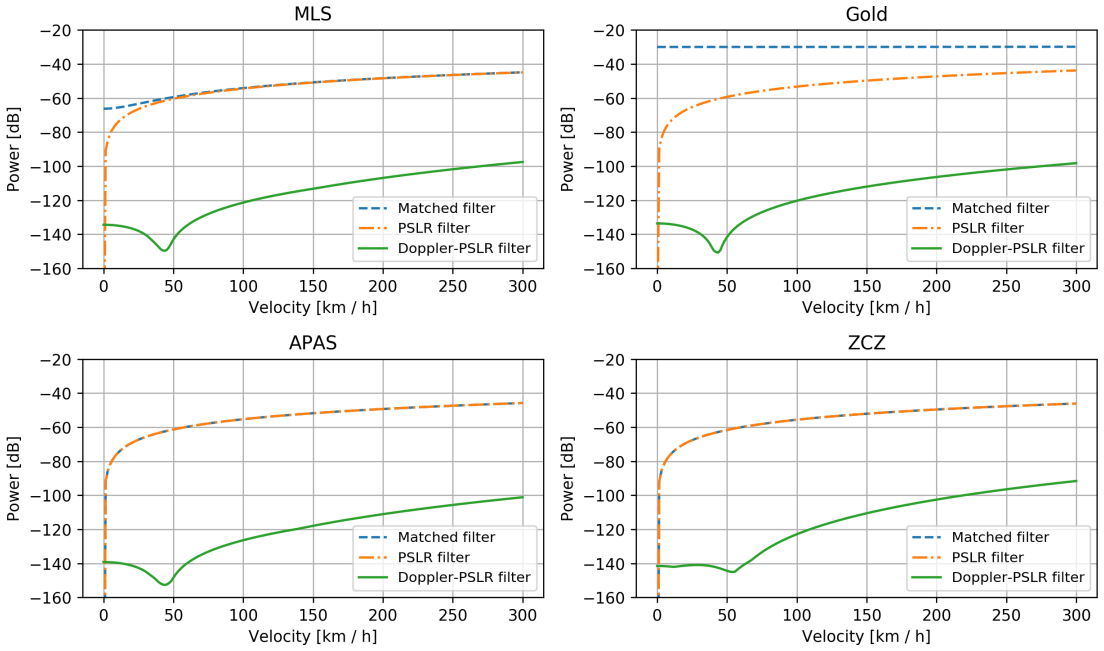

Figure 6.11: The PSLR of range responses of the designed filters.

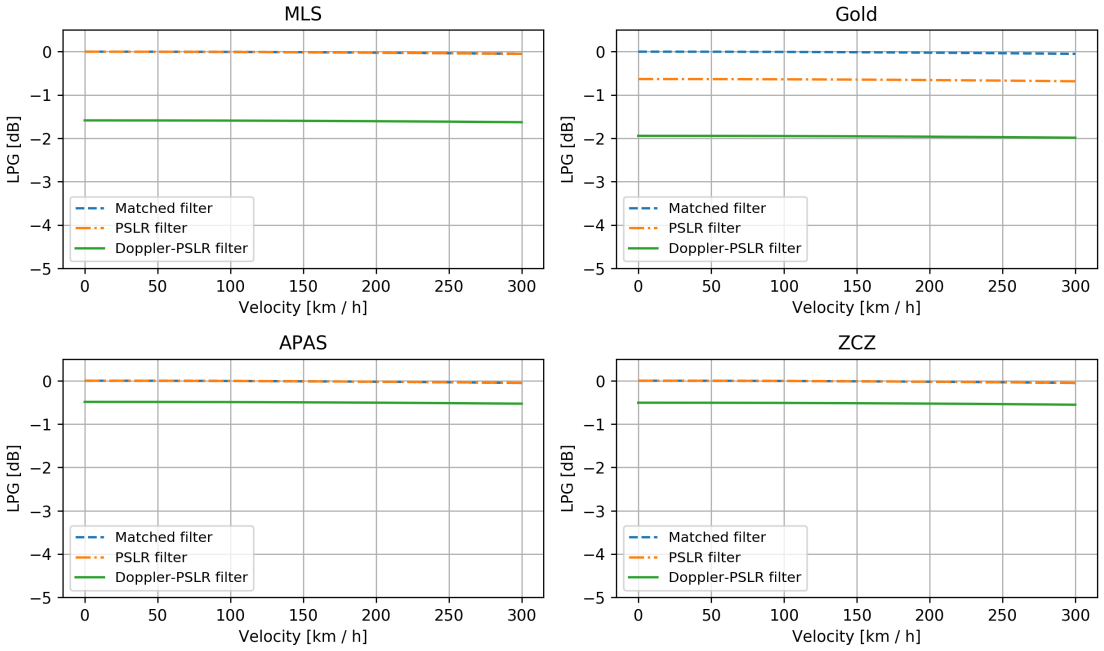

Figure 6.12: The LPGs of the designed pulse compression filters, evaluated at various doppler shifts.

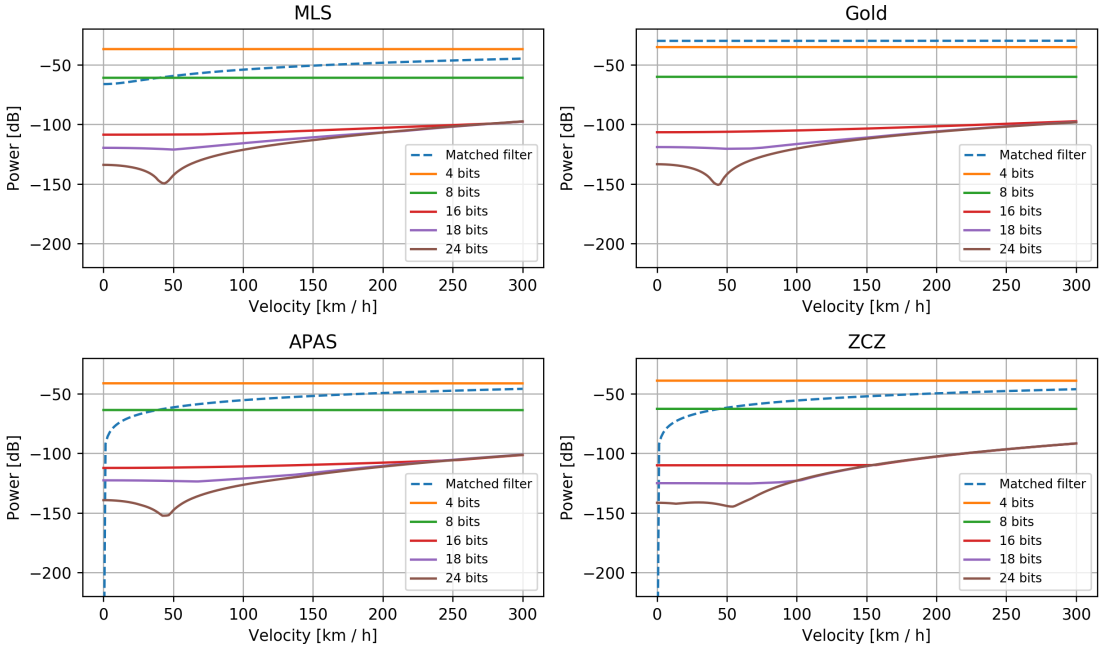

Figure 6.13: The PSLR of the range responses of the Doppler-PSLR filters after quantization, evaluated at various doppler shifts.

Chapter 7

Conclusion and future work

This thesis has attempted at making three contributions. First, some of the current established literature was gathered and summarized, where the focus was on describing the need, development and emergence of phase modulated systems in the automotive setting. Since mutual interference is a central topic in this, some works on mutual interference aspects were also reviewed, concluding that the differences compared with frequency modulated systems might not be as big as one might initially imagine. Second, a system analysis was performed, where a fair comparison between the frequency and phase modulated type of systems was attempted. It was shown that phase modulated systems provide better performance in terms resolution and contrasting capabilities, but suffers from dynamic range degradations in scenarios of uncompensated Doppler. Although it can be argued that the respective effects are insignificant in the general case, one should remember that many of the intended applications are safety critical, and good performance must always be guaranteed, even in the specific case. It is furthermore shown that phase modulated systems provide better performance in the angular domain due to the short pulse repetition interval, which appear to significantly alleviate motion induced errors in the virtual array, when compared with frequency modulated systems. Finally, it is argued that phase modulated systems are advantageous in terms of up-scaling due to the full baseband sampling approach.

In the third contribution, computational approaches were investigated in an attempt at alleviating some of the resolution and Doppler-degrading shortcomings of phase modulated systems. It was first confirmed that data adaptive algorithms may provide significant performance gains in some automotive scenarios where angular resolution is bottlenecking. Specifically, the iteartive adaptive approach was shown to provide the best peformance when all of the considered scenarios were jointly evaluated, with the sparse iterative covariance

based methods coming secondly. Then, a mismatched filtering approach was taken to deal with Doppler degradations at pulse compression. Specifically, a quadratically constrainted quadratic program was used to minimize the maximum peak sidelobes, also taking into account of Doppler-distortions. It was shown that for some common binary sequences, the Doppler-degradation can be heavily attenuated by mismatching at receive, using the designed filters, with only small losses in processing gain. However, it was observed that a major drawback is large number of bits needed in the filter representation.

For future works, it is believed that an entire data processing chain should be considered jointly in order to make definitive conclusions about the performances. Therefore, it is proposed that future work include state of the art detection and tracking systems in the analysis, evaluated using real data or possibly simulated, using a modern simulation framework (see e.g. [162] for an overview). Furthermore, some additional investigations on the mismatched filter design should be made, where one may explore the possibilities of adding a fixed number representation constraint into the optimization problem, as a way of reducing the number of bits required. Finally, the performance needs to be investigated under additional real world conditions, such as, for instance, hardware imperfections, including non-linearities and phase noise, among many other factors.

Bibliography

[1] M. Skolnik, *Introduction to Radar Systems*. McGraw-Hill, 2001.

[2] ——, *Radar Handbook, Third Edition*, ser. Electronics electrical engineering. McGraw-Hill, 2008.

[3] M. A. Richards, Ed., *Principles of Modern Radar: Basic principles*. Institution of Engineering and Technology, 2010.

[4] W. L. Melvin, Ed., *Principles of Modern Radar: Volume 3: Radar Applications*, ser. Radar, Sonar & Navigation. Institution of Engineering and Technology, 2013.

[5] R. Watson-Watt, "Radar in war and in peace," *Nature*, vol. 156, no. 3959, pp. 319–324, 1945.

[6] L. Brown, *A Radar History of World War II: Technical and Military Imperatives*. CRC Press, 1999.

[7] J. Richards, *Remote Sensing with Imaging Radar*, ser. Signals and Communication Technology. Springer Berlin Heidelberg, 2009.

[8] C. Li, V. M. Lubecke, O. Boric-Lubecke, and J. Lin, "A review on recent advances in doppler radar sensors for noncontact healthcare monitoring," *IEEE Transactions on Microwave Theory and Techniques*, vol. 61, no. 5, pp. 2046–2060, May 2013.

[9] H. Kuo, C. Lin, C. Yu, P. Lo, J. Lyu, C. Chou, and H. Chuang, "A fully integrated 60-ghz cmos direct-conversion doppler radar rf sensor with clutter canceller for single-antenna noncontact human vital-signs detection," *IEEE Transactions on Microwave Theory and Techniques*, vol. 64, no. 4, pp. 1018–1028, 2016.

[10] M. Mercuri, I. R. Lorato, Y.-H. Liu, F. Wieringa, C. V. Hoof, and T. Torfs, "Vital-sign monitoring and spatial tracking of multiple people using a contactless radar-based sensor," *Nature Electronics*, vol. 2, no. 6, pp. 252–262, Jun. 2019.

[11] S. Z. Gurbuz and M. G. Amin, "Radar-based human-motion recognition with deep learning: Promising applications for indoor monitoring," *IEEE Signal Processing Magazine*, vol. 36, no. 4, pp. 16–28, 2019.

[12] J. Le Kernec, F. Fioranelli, C. Ding, H. Zhao, L. Sun, H. Hong, J. Lorandel, and O. Romain, "Radar signal processing for sensing in assisted living: The challenges associated with real-time implementation of emerging algorithms," *IEEE Signal Processing Magazine*, vol. 36, no. 4, pp. 29–41, 2019.

[13] J. Hasch, E. Topak, R. Schnabel, T. Zwick, R. Weigel, and C. Waldschmidt, "Millimeter-Wave Technology for Automotive Radar Sensors in the 77 GHz Frequency Band," *IEEE Transactions on Microwave Theory and Techniques*, vol. 60, no. 3, pp. 845–860, 2012.

[14] Acconeer AB. (2020). [Online]. Available: https://www.acconeer.com/innovation-lab

[15] Imagimob. (2020). [Online]. Available: https://www.imagimob.com/news/acconeer-and-imagimob-combine-radar-technology-and-edge-ai-in-gesture-controlled-headphones-showcased-at-ces-2020

[16] Google. (2020). [Online]. Available: https://www.blog.google/products/pixel/new-features-pixel4/

[17] Google Soli. (2020). [Online]. Available: https://atap.google.com/soli/

[18] Google. (2020). [Online]. Available: https://ai.googleblog.com/2020/03/soli-radar-based-perception-and.html/

[19] ——. (2020). [Online]. Available: https://en.wikipedia.org/wiki/Pixel_4

[20] IEEE Signal Processing Magazine, *Advances in Radar Systems for Modern Civilian and Commercial Applications: Part 1.* IEEE, July 2019, vol. 36, no. 4.

[21] ——, *Advances in Radar Systems for Modern Civilian and Commercial Applications: Part 2.* IEEE, September 2019, vol. 36, no. 5.

[22] R. Klemm, U. Nickel, C. Gierull, and P. Lombardo, *Novel Radar Techniques and Applications: Real Aperture Array Radar, Imaging Radar, and Passive and Multistatic*

Radar, Volume 1, ser. Electromagnetics and Radar. Institution of Engineering and Technology, 2017.

[23] R. Klemm, H. Griffiths, and W. Koch, *Novel Radar Techniques and Applications: Waveform Diversity and Cognitive Radar and Target Tracking and Data Fusion, Volume 2*, ser. Electromagnetics and Radar. Institution of Engineering and Technology, 2017.

[24] "Global status report on road safety 2018." [Online]. Available: https://www.who.int/publications-detail/global-status-report-on-road-safety-2018

[25] J. Wenger, "Automotive radar - status and perspectives," in *IEEE Compound Semiconductor Integrated Circuit Symposium, 2005. CSIC '05.*, 2005, pp. 4 pp.–.

[26] K. Bengler, K. Dietmayer, B. Farber, M. Maurer, C. Stiller, and H. Winner, "Three decades of driver assistance systems: Review and future perspectives," *IEEE Intelligent Transportation Systems Magazine*, vol. 6, no. 4, pp. 6–22, 2014.

[27] W. D. Jones, "Building safer cars," *IEEE Spectrum*, vol. 39, no. 1, pp. 82–85, 2002.

[28] D. Gerónimo, A. M. López, A. D. Sappa, and T. Graf, "Survey of pedestrian detection for advanced driver assistance systems," *IEEE Transactions on Pattern Analysis and Machine Intelligence*, vol. 32, no. 7, pp. 1239–1258, 2010.

[29] K. Brookhuis, D. de Waard, and W. Janssen, "Behavioural impacts of advanced driver assistance systems–an overview," *European Journal of Transport and Infrastructure Research*, vol. 1, no. 3, 2001. [Online]. Available: https://journals.open.tudelft.nl/ejtir/article/view/3667

[30] M. G. Walden, "Automotive radar – from early developments to self-driving cars," 2015.

[31] H. H. Meinel, "Evolving automotive radar — from the very beginnings into the future," in *The 8th European Conference on Antennas and Propagation (EuCAP 2014)*, 2014, pp. 3107–3114.

[32] H. Rohling, M. Kronauge, "Continuous waveforms for automotive radar systems," 2012.

[33] H. Rohling, "Milestones in radar and the success story of automotive radar systems," in *11th International Radar Symposium*, 2010, pp. 1–6.

[34] Bosch Mobility Solutions. (2020). [Online]. Available: https://www.bosch-mobility-solutions.com/en/products-and-services/passenger-cars-and-light-commercial-vehicles/driver-assistance-systems/automatic-emergency-braking/mid-range-radar-sensor-(mrr)/

[35] InnoSenT. (2020). [Online]. Available: https://www.innosent.de/en/radar-systems/product-finder/

[36] Texas Instruments. (2020). [Online]. Available: http://www.ti.com/sensors/mmwave/awr/overview.html

[37] NXP. (2020). [Online]. Available: https://www.nxp.com/products/rf/radar-transceivers

[38] N. Levanon and E. Mozeson, *Radar Signals*, ser. Wiley - IEEE. Wiley, 2004.

[39] J. A. Scheer and W. L. Melvin, *Principles of Modern Radar, Volume 2 - Advanced Techniques*. Institution of Engineering and Technology - IET, 2013.

[40] M. Jankiraman, *FMCW Radar Design*, ser. Artech House radar library. Artech House, 2018.

[41] M. Murad, I. Bilik, M. Friesen, J. Nickolaou, J. Salinger, K. Geary, and J. S. Colburn, "Requirements for next generation automotive radars," in *2013 IEEE Radar Conference (RadarCon13)*, 2013, pp. 1–6.

[42] I. Bilik, O. Longman, S. Villeval, and J. Tabrikian, "The rise of radar for autonomous vehicles: Signal processing solutions and future research directions," *IEEE Signal Processing Magazine*, vol. 36, no. 5, pp. 20–31, 2019.

[43] F. Engels, P. Heidenreich, A. M. Zoubir, F. K. Jondral, and M. Wintermantel, "Advances in automotive radar: A framework on computationally efficient high-resolution frequency estimation," *IEEE Signal Processing Magazine*, vol. 34, no. 2, pp. 36–46, 2017.

[44] S. M. Patole, M. Torlak, D. Wang, and M. Ali, "Automotive radars: A review of signal processing techniques," *IEEE Signal Processing Magazine*, vol. 34, no. 2, pp. 22–35, 2017.

[45] J. Li and P. Stoica, "Mimo radar with colocated antennas," *IEEE Signal Processing Magazine*, vol. 24, no. 5, pp. 106–114, 2007.

[46] Texas Instruments. (2020) AWR2243 Single-Chip 76- to 81-GHz FMCW Transceiver. [Online]. Available: https://www.ti.com/product/AWR2243

[47] NXP. (2020) TEF810X Fully-Integrated 77 GHz Radar Transceiver. [Online]. Available: https://www.nxp.com/products/rf/radar-transceivers/tef810x-fully-integrated-77-ghz-radar-transceiver:TEF810X

[48] ST. (2020) Automotive dual-band 77 GHz radar transceiver (3 TX / 4 RX) with integrated FMCW chirp modulator and chirps sequencer. [Online]. Available: https://www.st.com/content/st_com/en/products/automotive-adas-devices/automotive-radar-transceivers/strada770m.html

[49] Texas Intruments. (2020) Imaging Radar Using Cascaded mmWave Sensor Reference Design. [Online]. Available: https://www.ti.com/tool/TIDEP-01012

[50] Vayyar. (2020). [Online]. Available: https://vayyar.com/technology

[51] V. Giannini, M. Goldenberg, A. Eshraghi, J. Maligeorgos, L. Lim, R. Lobo, D. Welland, C. Chow, A. Dornbusch, T. Dupuis, S. Vaz, F. Rush, P. Bassett, H. Kim, M. Maher, O. Schmid, C. Davis, and M. Hegde, "9.2 a 192-virtual-receiver 77/79ghz gmsk code-domain mimo radar system-on-chip," in *2019 IEEE International Solid- State Circuits Conference - (ISSCC)*, 2019, pp. 164–166.

[52] Arbe. (2020). [Online]. Available: https://arberobotics.com/

[53] F. Daum and J. Huang, "Mimo radar: Snake oil or good idea?" in *2009 International Waveform Diversity and Design Conference*, Feb 2009, pp. 113–117.

[54] E. Brookner, "Mimo radar demystified and where it makes sense to use," in *2014 IEEE International Conference on Acoustics, Speech and Signal Processing (ICASSP)*, May 2014, pp. 5292–5296.

[55] T. Kilpatrick and I. D. Longstaff, "Mimo radar - some practical considerations," in *2015 IEEE Radar Conference (RadarCon)*, May 2015, pp. 0566–0571.

[56] Y. I. Abramovich and G. J. Frazer, "Bounds on the volume and height distributions for the mimo radar ambiguity function," *IEEE Signal Processing Letters*, vol. 15, pp. 505–508, 2008.

[57] J. Bechter, M. Rameez, and C. Waldschmidt, "Analytical and experimental investigations on mitigation of interference in a dbf mimo radar," *IEEE Transactions on Microwave Theory and Techniques*, vol. 65, no. 5, pp. 1727–1734, 2017.

[58] C. Aydogdu, G. K. Carvajal, O. Eriksson, H. Hellsten, H. Herbertsson, M. F. Keskin, E. Nilsson, M. Rydström, K. Vanäs, and H. Wymeersch, "Radar interference mitigation for automated driving," 2019.

[59] S. Alland, W. Stark, M. Ali, and M. Hegde, "Interference in automotive radar systems: Characteristics, mitigation techniques, and current and future research," *IEEE Signal Processing Magazine*, vol. 36, no. 5, pp. 45–59, Sep. 2019.

[60] D. Guermandi, Q. Shi, A. Dewilde, V. Derudder, U. Ahmad, A. Spagnolo, A. Bourdoux, P. Wambacq, and W. van Thillo, "A 79ghz 2x2 mimo pmcw radar soc in 28nm cmos," in *2016 IEEE Asian Solid-State Circuits Conference (A-SSCC)*, 2016, pp. 105–108.

[61] D. Guermandi, Q. Shi, A. Dewilde, V. Derudder, U. Ahmad, A. Spagnolo, I. Ocket, A. Bourdoux, P. Wambacq, J. Craninckx, and W. Van Thillo, "A 79-ghz 2 $\times$ 2 mimo pmcw radar soc in 28-nm cmos," *IEEE Journal of Solid-State Circuits*, vol. 52, no. 10, pp. 2613–2626, Oct 2017.

[62] K. V. Mishra, M. R. Bhavani Shankar, V. Koivunen, B. Ottersten, and S. A. Vorobyov, "Toward millimeter-wave joint radar communications: A signal processing perspective," *IEEE Signal Processing Magazine*, vol. 36, no. 5, pp. 100–114, 2019.

[63] A. Bourdoux, U. Ahmad, D. Guermandi, S. Brebels, A. Dewilde, and W. Van Thillo, "Pmcw waveform and mimo technique for a 79 ghz cmos automotive radar," in *2016 IEEE Radar Conference (RadarConf)*, 2016, pp. 1–5.

[64] V. Giannini, D. Guermandi, Q. Shi, A. Medra, W. Van Thillo, A. Bourdoux, and P. Wambacq, "A 79 ghz phase-modulated 4 ghz-bw cw radar transmitter in 28 nm cmos," *IEEE Journal of Solid-State Circuits*, vol. 49, no. 12, pp. 2925–2937, Dec 2014.

[65] W. Van Thillo, V. Giannini, D. Guermandi, S. Brebels, and A. Bourdoux, "Impact of adc clipping and quantization on phase-modulated 79 ghz cmos radar," in *2014 11th European Radar Conference*, 2014, pp. 285–288.

[66] B. Verbruggen, J. Craninckx, M. Kuijk, P. Wambacq, and G. Van der Plas, "A 2.6 mw 6 bit 2.2 gs/s fully dynamic pipeline adc in 40 nm digital cmos," *IEEE Journal of*

Solid-State Circuits, vol. 45, no. 10, pp. 2080–2090, 2010.

[67] Y. Gai, A. Dewilde, U. Ahmad, A. Bourdoux, and S. Pollin, "Parallelized correlator bank for a 1 ghz bandwidth phase modulated cw radar in the 79ghz band," in *2015 IEEE Symposium on Communications and Vehicular Technology in the Benelux (SCVT)*, 2015, pp. 1–6.

[68] H. Haderer, R. Feger, and A. Stelzer, "A comparison of phase-coded cw radar modulation schemes for integrated radar sensors," in *2014 11th European Radar Conference*, 2014, pp. 593–596.

[69] W. Van Thillo, P. Gioffré, V. Giannini, D. Guermandi, S. Brebels, and A. Bourdoux, "Almost perfect auto-correlation sequences for binary phase-modulated continuous wave radar," in *2013 European Radar Conference*, 2013, pp. 491–494.

[70] H. Haderer, R. Feger, C. Pfeffer, and A. Stelzer, "Millimeter-wave phase-coded cw mimo radar using zero- and low-correlation-zone sequence sets," *IEEE Transactions on Microwave Theory and Techniques*, vol. 64, no. 12, pp. 4312–4323, 2016.

[71] G. M. Brooker, "Mutual interference of millimeter-wave radar systems," *IEEE Transactions on Electromagnetic Compatibility*, vol. 49, no. 1, pp. 170–181, 2007.

[72] M. Goppelt, H. . Blöcher, and W. Menzel, "Analytical investigation of mutual interference between automotive fmcw radar sensors," in *2011 German Microwave Conference*, 2011, pp. 1–4.

[73] M. Barjenbruch, D. Kellner, K. Dietmayer, J. Klappstein, and J. Dickmann, "A method for interference cancellation in automotive radar," in *2015 IEEE MTT-S International Conference on Microwaves for Intelligent Mobility (ICMIM)*, 2015, pp. 1–4.

[74] J. Bechter, K. Eid, F. Roos, and C. Waldschmidt, "Digital beamforming to mitigate automotive radar interference," in *2016 IEEE MTT-S International Conference on Microwaves for Intelligent Mobility (ICMIM)*, 2016, pp. 1–4.

[75] J. Bechter, K. D. Biswas, and C. Waldschmidt, "Estimation and cancellation of interferences in automotive radar signals," in *2017 18th International Radar Symposium (IRS)*, 2017, pp. 1–10.

[76] F. Uysal and S. Sanka, "Mitigation of automotive radar interference," in *2018 IEEE Radar Conference (RadarConf18)*, 2018, pp. 0405–0410.

[77] J. Bechter and C. Waldschmidt, "Automotive radar interference mitigation by reconstruction and cancellation of interference component," in *2015 IEEE MTT-S International Conference on Microwaves for Intelligent Mobility (ICMIM)*, 2015, pp. 1–4.

[78] A. Al-Hourani, R. J. Evans, S. Kandeepan, B. Moran, and H. Eltom, "Stochastic geometry methods for modeling automotive radar interference," *IEEE Transactions on Intelligent Transportation Systems*, vol. 19, no. 2, pp. 333–344, 2018.

[79] A. Bourdoux, K. Parashar, and M. Bauduin, "Phenomenology of mutual interference of fmcw and pmcw automotive radars," in *2017 IEEE Radar Conference (RadarConf)*, 2017, pp. 1709–1714.

[80] H. Beise, T. Stifter, and U. Schröder, "Virtual interference study for fmcw and pmcw radar," in *2018 11th German Microwave Conference (GeMiC)*, 2018, pp. 351–354.

[81] J. Overdevest, F. Jansen, F. Laghezza, F. Uysal, and A. Yarovoy, "Uncorrelated interference in 79 ghz fmcw and pmcw automotive radar," in *2019 20th International Radar Symposium (IRS)*, 2019, pp. 1–8.

[82] M. M. W. Stark, M. Ali, "Digital Code Modulation (DCM) Radar for Automotive Application," Uhnder, Tech. Rep., 01 2020.

[83] H. C. Yildirim, M. Bauduin, A. Bourdoux, and F. Horlin, "Impact of phase noise on mutual interference of fmcw and pmcw automotive radars," in *2019 16th European Radar Conference (EuRAD)*, 2019, pp. 181–184.

[84] S. Stephany, B. Schweizer, C. Knill, and C. Waldschmidt, "Impact of an automotive chirp-sequence interferer on a wideband pseudo-noise radar," in *2019 International Conference on Electromagnetics in Advanced Applications (ICEAA)*, 2019, pp. 0859–0862.

[85] J. P. Bordes, C. E. Davis, W. A. Stark, O. K. Schmidt, and R. P. Rao, "PMCW-PMCW interference mitigation." Uhnder Inc, September 2017, Patent US9772397B1. [Online]. Available: https://patents.google.com/patent/US9772397B1/en

[86] "Digital automotive radar," https://www.uhnder.com/.

[87] S. Taranovich, "A digital mmw radar ic for automotive use," https://www.edn.com/5G/4461894/Uhnder-Digital-mmW-RADAR-IC, May 2019.

[88] P. Swerling, "Probability of detection for fluctuating targets," *IRE Transactions on Information Theory*, vol. 6, no. 2, pp. 269–308, 1960.

[89] N. Yamada, Y. Tanaka, and K. Nishikawa, "Radar cross section for pedestrian in 76ghz band," in *2005 European Microwave Conference*, vol. 2, 2005, pp. 4 pp.–1018.

[90] F. Gini, A. De Maio, and L. Patton, *Waveform Design and Diversity for Advanced Radar Systems*, ser. IET radar, sonar and navigation series. Institution of Engineering and Technology, 2012.

[91] H. He, J. Li, and P. Stoica, *Waveform Design for Active Sensing Systems: A Computational Approach*. Cambridge University Press, 2012.

[92] E. García, J. A. Paredes, F. J. Álvarez, M. C. Pérez, and J. J. García, "Spreading sequences in active sensing: A review," *Signal Processing*, vol. 106, pp. 88 – 105, 2015.

[93] A. Bourdoux, U. Ahmad, D. Guermandi, S. Brebels, A. Dewilde, and W. Van Thillo, "Pmcw waveform and mimo technique for a 79 ghz cmos automotive radar," in *2016 IEEE Radar Conference (RadarConf)*, 2016, pp. 1–5.

[94] D. V. Sarwate and M. B. Pursley, "Crosscorrelation properties of pseudorandom and related sequences," *Proceedings of the IEEE*, vol. 68, no. 5, pp. 593–619, 1980.

[95] J. Wolfmann, "Almost perfect autocorrelation sequences," *IEEE Transactions on Information Theory*, vol. 38, no. 4, pp. 1412–1418, 1992.

[96] D. Jungnickel and A. Pott, "Perfect and almost perfect sequences," *Discrete Applied Mathematics*, vol. 95, no. 1, pp. 331 – 359, 1999.

[97] P. Langevin, "Some sequences with good autocorrelation properties," in *Finite Fields*, ser. Contemporary Mathematics, vol. 168, Las Vegas, United States, 1994, pp. 175–185. [Online]. Available: https://hal.archives-ouvertes.fr/hal-01279317

[98] ——, "Almost perfect sequences," 2017. [Online]. Available: http://langevin.univ-tln.fr/project/apc/aps.html

[99] H. Haderer, R. Feger, C. Pfeffer, and A. Stelzer, "Millimeter-wave phase-coded cw mimo radar using zero-correlation-zone sequence sets," in *2015 IEEE MTT-S International Microwave Symposium*, 2015, pp. 1–4.

[100] F. Benattou, H. Mimoun, R. Messaoudi, and M. Addad, "A new class of ternary zero correlation zone sequence sets based on mutually orthogonal complementary sets,"

IOSR Journal of Electronics and Communication Engineering 2278-8735, vol. 10, pp. 8–13, 06 2015.

[101] J. J. M. de Wit, W. L. van Rossum, and A. J. de Jong, "Orthogonal waveforms for fmcw mimo radar," in *2011 IEEE RadarCon (RADAR)*, 2011, pp. 686–691.

[102] H. Sun, F. Brigui, and M. Lesturgie, "Analysis and comparison of mimo radar waveforms," in *2014 International Radar Conference*, 2014, pp. 1–6.

[103] A. Zwanetski and H. Rohling, "Continuous wave mimo radar based on time division multiplexing," in *2012 13th International Radar Symposium*, 2012, pp. 119–121.

[104] J. Overdevest, F. Jansen, F. Uysal, and A. Yarovoy, "Doppler influence on waveform orthogonality in 79 ghz mimo phase-coded automotive radar," *IEEE Transactions on Vehicular Technology*, vol. 69, no. 1, pp. 16–25, 2020.

[105] Wikipedia contributors, "Welch bounds — Wikipedia, the free encyclopedia," 2020. [Online]. Available: https://en.wikipedia.org/wiki/Welch_bounds

[106] S. Kay, *Fundamentals of Statistical Signal Processing: Detection theory*, ser. Prentice Hall Signal Processing Series. Prentice-Hall PTR, 1998.

[107] M. Zatman, "How narrow is narrowband?" *IEE Proceedings - Radar, Sonar and Navigation*, vol. 145, no. 2, pp. 85–91, 1998.

[108] H. Van Trees, *Optimum Array Processing: Part IV of Detection, Estimation, and Modulation Theory*, ser. Detection, Estimation, and Modulation Theory. Wiley, 2004.

[109] M. Sullivan, *Practical Array Processing*. McGraw-Hill Education, 2008.

[110] P. Stoica, Jian Li, and Ming Xue, "Transmit codes and receive filters for pulse compression radar systems," in *2008 IEEE International Conference on Acoustics, Speech and Signal Processing*, 2008, pp. 3649–3652.

[111] O. Rabaste and L. Savy, "Mismatched filter optimization for radar applications using quadratically constrained quadratic programs," *IEEE Transactions on Aerospace and Electronic Systems*, vol. 51, no. 4, pp. 3107–3122, 2015.

[112] P. Stoica and R. Moses, *Spectral Analysis of Signals*. Pearson Prentice Hall, 2005.

[113] V. C. Chen, F. Li, S. . Ho, and H. Wechsler, "Micro-doppler effect in radar: phenomenon, model, and simulation study," *IEEE Transactions on Aerospace and Electronic Systems*, vol. 42, no. 1, pp. 2–21, 2006.

[114] T. Wagner, R. Feger, and A. Stelzer, "Radar signal processing for jointly estimating tracks and micro-doppler signatures," *IEEE Access*, vol. 5, pp. 1220–1238, 2017.

[115] C. Will, P. Vaishnav, A. Chakraborty, and A. Santra, "Human target detection, tracking, and classification using 24-ghz fmcw radar," *IEEE Sensors Journal*, vol. 19, no. 17, pp. 7283–7299, 2019.

[116] Y. Kim and H. Ling, "Human activity classification based on micro-doppler signatures using a support vector machine," *IEEE Transactions on Geoscience and Remote Sensing*, vol. 47, no. 5, pp. 1328–1337, 2009.

[117] Y. Kim and T. Moon, "Human detection and activity classification based on micro-doppler signatures using deep convolutional neural networks," *IEEE Geoscience and Remote Sensing Letters*, vol. 13, no. 1, pp. 8–12, 2016.

[118] S. Xu and A. Yarovoy, "Doppler shifts mitigation for pmcw signals," in *2019 International Radar Conference (RADAR)*, 2019, pp. 1–5.

[119] G. Hakobyan and B. Yang, "High-performance automotive radar: A review of signal processing algorithms and modulation schemes," *IEEE Signal Processing Magazine*, vol. 36, no. 5, pp. 32–44, 2019.

[120] K. B. Petersen, M. S. Pedersen, J. Larsen, K. Strimmer, L. Christiansen, K. Hansen, L. He, L. Thibaut, M. Barão, S. Hattinger, V. Sima, and W. The, "The matrix cookbook," Tech. Rep., 2006.

[121] M. Richards, *Fundamentals of Radar Signal Processing, Second Edition.* McGraw-Hill, 2014.

[122] S. M. Kay, *Fundamentals of Statistical Signal Processing, Volume 1: Estimation Theory.* Pearson Education, 1993.

[123] A. Dogandzic and A. Nehorai, "Cramer-rao bounds for estimating range, velocity, and direction with an active array," *IEEE Transactions on Signal Processing*, vol. 49, no. 6, pp. 1122–1137, 2001.

[124] J.-P. Delmas, "Performance bounds and statistical analysis of DOA estimation," in *Array and statistical signal processing,*, ser. Academic Press library in signal processing. Elsevier, 2015, vol. 3, pp. 719 – 764. [Online]. Available: https://hal.archives-ouvertes.fr/hal-01285947

[125] M. Chen and C. Chen, "Rcs patterns of pedestrians at 76-77 ghz," *IEEE Antennas and Propagation Magazine*, vol. 56, no. 4, pp. 252–263, 2014.

[126] M. Haruta, H. Ishizaka, O. Hashimoto, J. Ueyama, and K. Wada, "Measurement of radar cross section for a truck and bus under an open field in 60 ghz band," *Microwave and Optical Technology Letters*, vol. 25, no. 4, pp. 243–246, 2000.

[127] J. Hasch, "Driving towards 2020: Automotive radar technology trends," in *2015 IEEE MTT-S International Conference on Microwaves for Intelligent Mobility (ICMIM)*, 2015, pp. 1–4.

[128] B. T. Arnold and M. A. Jensen, "The effect of antenna mutual coupling on mimo radar system performance," *IEEE Transactions on Antennas and Propagation*, vol. 67, no. 3, pp. 1410–1416, 2019.

[129] C. M. Schmid, C. Pfeffer, R. Feger, and A. Stelzer, "An fmcw mimo radar calibration and mutual coupling compensation approach," in *2013 European Radar Conference*, 2013, pp. 13–16.

[130] M. Stephan, K. Wang, T. Reissland, R. Weigel, K. Wu, and F. Lurz, "Evaluation of antenna calibration and doa estimation algorithms for fmcw radars," in *2019 16th European Radar Conference (EuRAD)*, 2019, pp. 309–312.

[131] Texas Instruments, "People Tracking and Counting Reference Design Using mmWave Radar Sensor," Mar 2018.

[132] H. Krim and M. Viberg, "Two decades of array signal processing research: the parametric approach," *IEEE Signal Processing Magazine*, vol. 13, no. 4, pp. 67–94, 1996.

[133] M. Kronauge, C. Schroeder, and H. Rohling, "Radar target detection and doppler ambiguity resolution," in *11-th INTERNATIONAL RADAR SYMPOSIUM*, 2010, pp. 1–4.

[134] F. Roos, J. Bechter, N. Appenrodt, J. Dickmann, and C. Waldschmidt, "Enhancement of doppler unambiguity for chirp-sequence modulated tdm-mimo radars," in *2018 IEEE*

MTT-S International Conference on Microwaves for Intelligent Mobility (ICMIM), 2018, pp. 1–4.

[135] H. A. Gonzalez, C. Liu, B. Vogginger, and C. G. Mayr, "Doppler ambiguity resolution for binary-phase-modulated mimo fmcw radars," in *2019 International Radar Conference (RADAR)*, 2019, pp. 1–6.

[136] Texas Instruments. (2018). [Online]. Available: https://www.ti.com/tool/TIDEP-0092

[137] J. Dickmann, J. Klappstein, H. Bloecher, M. Muntzinger, and H. Meinel, "Automotive radar — "quo vadis?"," in *2012 9th European Radar Conference*, 2012, pp. 18–21.

[138] C. M. Schmid, R. Feger, C. Pfeffer, and A. Stelzer, "Motion compensation and efficient array design for tdma fmcw mimo radar systems," in *2012 6th European Conference on Antennas and Propagation (EUCAP)*, 2012, pp. 1746–1750.

[139] R. Schmidt, "Multiple emitter location and signal parameter estimation," *IEEE Transactions on Antennas and Propagation*, vol. 34, no. 3, pp. 276–280, 1986.

[140] J. Capon, "High-resolution frequency-wavenumber spectrum analysis," *Proceedings of the IEEE*, vol. 57, no. 8, pp. 1408–1418, 1969.

[141] Jian Li, P. Stoica, and Zhisong Wang, "On robust capon beamforming and diagonal loading," *IEEE Transactions on Signal Processing*, vol. 51, no. 7, pp. 1702–1715, 2003.

[142] T. Yardibi, J. Li, P. Stoica, M. Xue, and A. B. Baggeroer, "Source localization and sensing: A nonparametric iterative adaptive approach based on weighted least squares," *IEEE Transactions on Aerospace and Electronic Systems*, vol. 46, no. 1, pp. 425–443, Jan 2010.

[143] A. Sakhnini and A. Jakobsson, "Direction of arrival estimation using the generalized spice criterion," in *The 17th European Radar Conference (EuRAD 2020)*, 2020.

[144] J. Swärd, S. I. Adalbjörnsson, and A. Jakobsson, "Generalized sparse covariance-based estimation," *Signal Processing*, vol. 143, pp. 311 – 319, 2018.

[145] P. Stoica, P. Babu, and J. Li, "Spice: A sparse covariance-based estimation method for array processing," *IEEE Transactions on Signal Processing*, vol. 59, no. 2, pp. 629–638, Feb 2011.

[146] ——, "New method of sparse parameter estimation in separable models and its use for spectral analysis of irregularly sampled data," *IEEE Transactions on Signal Processing*, vol. 59, no. 1, pp. 35–47, Jan 2011.

[147] J. Li, X. Zhu, P. Stoica, and M. Rangaswamy, "Iterative space-time adaptive processing," in *2009 IEEE 13th Digital Signal Processing Workshop and 5th IEEE Signal Processing Education Workshop*, 2009, pp. 440–445.

[148] W. Roberts, P. Stoica, J. Li, T. Yardibi, and F. A. Sadjadi, "Iterative adaptive approaches to mimo radar imaging," *IEEE Journal of Selected Topics in Signal Processing*, vol. 4, no. 1, pp. 5–20, 2010.

[149] Z. Yang, X. Li, H. Wang, and W. Jiang, "Adaptive clutter suppression based on iterative adaptive approach for airborne radar," *Signal Processing*, vol. 93, no. 12, pp. 3567 – 3577, 2013, special Issue on Advances in Sensor Array Processing in Memory of Alex B. Gershman.

[150] A. Das, D. Zachariah, and P. Stoica, "Comparison of two hyperparameter-free sparse signal processing methods for direction-of-arrival tracking in the hf97 ocean acoustic experiment," *IEEE Journal of Oceanic Engineering*, vol. 43, no. 3, pp. 725–734, July 2018.

[151] S. Fortunati, R. Grasso, F. Gini, M. S. Greco, and K. LePage, "Three cs-based beamformers for single snapshot doa estimation," in *2014 22nd European Signal Processing Conference (EUSIPCO)*, Sep. 2014, pp. 1044–1048.

[152] F. Tao, T. Wang, J. Wu, and Y. Su, "A knowledge aided spice space time adaptive processing method for airborne radar with conformal array," *Signal Processing*, vol. 152, pp. 54 – 62, 2018.

[153] J. Ren, T. Zhang, J. Li, L. H. Nguyen, and P. Stoica, "Rfi mitigation for uwb radar via hyperparameter-free sparse spice methods," *IEEE Transactions on Geoscience and Remote Sensing*, vol. 57, no. 6, pp. 3105–3118, June 2019.

[154] Y. Zhang, A. Jakobsson, Y. Zhang, Y. Huang, and J. Yang, "Wideband sparse reconstruction for scanning radar," *IEEE Transactions on Geoscience and Remote Sensing*, vol. 56, no. 10, pp. 6055–6068, Oct 2018.

[155] Y. Zhang, D. Mao, Y. Bu, J. Wu, Y. Huang, and A. Jakobsson, "Online high resolution stochastic radiation radar imaging using sparse covariance fitting," in *IGARSS 2019 -*

2019 IEEE International Geoscience and Remote Sensing Symposium, July 2019, pp. 8562–8565.

[156] Y. Zhang, A. Jakobsson, D. Mao, Y. Zhang, Y. Huang, and J. Yang, "Generalized time-updating sparse covariance-based spectral estimation," *IEEE Access*, vol. 7, pp. 143 876–143 887, 2019.

[157] A. Sakhnini, D. Montgomery, and A. Jakobsson, "Time-updating the generalized sparse covariance-based estimator," in *2018 International Symposium on Intelligent Signal Processing and Communication Systems (ISPACS)*, Nov 2018, pp. 357–362.

[158] G. Glentis and A. Jakobsson, "Efficient implementation of iterative adaptive approach spectral estimation techniques," *IEEE Transactions on Signal Processing*, vol. 59, no. 9, pp. 4154–4167, 2011.

[159] G. O. Glentis and A. Jakobsson, "Superfast approximative implementation of the iaa spectral estimate," *IEEE Transactions on Signal Processing*, vol. 60, no. 1, pp. 472–478, 2012.

[160] S. Boyd and L. Vandenberghe, *Convex Optimization*. Cambridge University Press, 2004.

[161] S. Diamond and S. Boyd, "CVXPY: A Python-embedded modeling language for convex optimization," *Journal of Machine Learning Research*, vol. 17, no. 83, pp. 1–5, 2016.

[162] Y. Kang, H. Yin, and C. Berger, "Test your self-driving algorithm: An overview of publicly available driving datasets and virtual testing environments," *IEEE Transactions on Intelligent Vehicles*, vol. 4, no. 2, pp. 171–185, 2019.